Department of Physics and Astronomy

Heidelberg University

Master thesis

in Physics

submitted by

Junhee Lee

born in Goyang

2023

Shaping waveform of X-ray Mössbauer scattering into short pulses

---

This Master thesis has been carried out by

Junhee Lee

at the

Max Planck Institute for Nuclear Physics

under the supervision of

apl. Prof. Dr. Jörg Evers

Shaping waveform of X-ray Mössbauer scattering into short pulses

The Mössbauer nuclei have proven as a good platform for X-ray quantum optics with their coherent resonant scattering and ultranarrow linewidth from recoiless scattering, and long lifetime. Despite the successes in the study of the Mössbauer nuclei and relevant quantum optics, the research has been restricted from the difficulties of generating multiple coherent pulses with short duration and high intensity. This thesis proposes a method for shaping the waveform of Mössbauer scattering into pulses in nanoseconds duration. Regarding their long lifetime, the study is expected to promote the study of the nuclear targets' dynamics, specifically, nuclear pump-probe measurement, etc. The motions of two nuclei by piezotransducers control the phases of coherent scattering fields and shape them into pulse-shape. The second study investigates the deviation in the measured motion. Narrowing down to the a part of the motion system, electronic response of the piezo transducer, its electronic property and limitations are studied and tested as response functions in the frequency domain with varying external voltage inputs and types of piezo transducers. With this measurements and future study in mechanical response, it is expected to allow improved controllability to the motion system on the nanosecond time scale and wavelength-order spatial scale.

Contents

Chapter 1

Introduction

The advent of new light sources in the year 1960 [1] has brought a broad range of applications to scientists and engineers over the last century. Nowadays, it is even difficult to find the fields where the laser is not used. The wide applications of laser can be found in communication [2], laser metrology [3], spectroscopy [4, 5], and even nuclear fusion [6]. The development of ultrashort lasers with the Q-switching [7], the mode-locking techniques [8, 9], and, chirped pulse amplification[10, 11] deepens and broadens our understanding of nature. Specifically, its short duration opens a way to investigate the fast dynamics of the charge carriers, atoms, and molecules from nanosecond to femtosecond time scales [12, 13].

The development of the Quantum Optic field is also accompanied by the advancement of laser technology. The coherent property and tunability of the laser light source have enabled us to exploit the quantum nature of the matter as well as the photon. Relevant successes can be found in the field of quantum metrology [14, 15], precise measurement [16] to control of light-matter interactions [17, 18]. Furthermore, coherent short pulses have shown applications as coherent control of the system, [19, 20, 21]. However, the usual laser sources operate at wavelengths from microwaves, infrared, and the visible light, to ultraviolet.

The X-ray's short wavelength has provided a useful research tool to scientists. The research fields, from nanoscale physics [22, 23], interactions with core electrons in the atomic shell [24, 25], to the nucleus [26, 27], became the researchable area with X-ray and have reported interesting sciences and development in technologies.

On the other hand, the X-ray quantum optics field has remained a relatively new field [28], though the X-ray is not fundamentally different from visible light where great progress has been achieved in the Quantum optics field. The synchrotron light sources such as PETRA III (DESY in Hamburg), ESRF (in Grenovel), etc operating in X-ray range can be a game changer in this rising field [29, 30, 31]. The produced beam's property: beam brilliance, beam collimation, photon numbers, and picoseconds pulse duration broadens the area of the Quantum optics research field. The reported successful Quantum optical concepts in the X-ray regime are including Hanbury Brown-Twiss effect [32], ghost imaging[33, 34], parametric down-conversion [35], and two-photon X-ray spectroscopy [36]. Furthermore, operation of the XFELs [37, 38] are expected to promise more fruitful research [39, 40] with its higher brilliance and shorter pulse duration, etc.

Moving to the Nuclear quantum optics, the Mössbauer nuclei are of particular interest. Due to their long lifetime, recoilless, and coherent scattering process, they

offer ultranarrow resonance widths in frequency and coherent forward scattering (Nuclear Forward Scattering, NFS) in time [41, 42]. The most popular isotope ^{57}Fe shows a transition energy of 14.4 keV with a linewidth of 4.7neV which corresponds to a lifetime of 141ns. The ^{57}Fe provides successful storage of single photon [43, 44], and supperadiance [45, 46], collective Lamb-shift [45]. And the lists go on for coherent control of NFS. With the magnetic field, control of Bragg scattering [47] and enhancement of re-emission [48] are reported in the early 90s. More recently, the motion by the piezo transducer, ultrasonic, or the magnon also allows other ways to give a coherent control to NFS property, including nuclear dynamics [49, 50, 51] and shaping [52, 53].

The two projects of this thesis can be found in the context of the NFS with moving Mössbauer nuclei. The first project will provide one method that shapes the scattering waveform into pulse-shape with the two thin ^{57}Fe targets. The successfully shaped pulse waveform will give a tool to understand the dynamics of nuclear targets, nuclear pump-probe measurement. Applying motions to the targets, it makes possible to control the time intensity by the interference effect and beating. Most of the time, the motion of the targets will construct a destructive interference to achieve low-intensity. Such destructive interference condition is purposely broken to produce a pulse at a desired time. Based on the formulated general equation for the two targets' NFS, the property of the pulse will be analyzed and discussed as a function of the targets' thickness. For example, the maximum intensity of the produced pulse, time duration, pulse-to-pulse delay, and general motion conditions. Furthermore, one application using polarization dependent scattering will be provided that lowers the time intensity at both sides of the generated pulse. Hence, the enhanced intensity contrast is achieved for the generated pulse.

The measured real displacement of the Mössbauer nuclei is not exactly following the desired profile [54, 55]. The second project aims to diagnose the reason for the imperfect motions in the synchrotron experiments. To fully characeterize the motion system and achieve precise motion control, we need to understand both electronic response of the piezo transducer as well as the mechanical response of the Mössbauer target. The study will focus on the part of the motion system, the electronic response of the piezo transducers, instead of measuring the motions of the Mössbauer target. The measurement of electronic response of the piezo transducers is available with the electronics without using the X-ray photon sources. The electronics have been already set to test the piezo transducers for the past beamtimes [54]. The piezo transducer and relevant electronics are investigated as response functions in the frequency domain, where a physical process is easily formulated. A couple of processes are required to calculate the response function from raw data, properly. The average will take place at first to get rid of thermal noises. The 768ns length data will be chosen out of the raw data for the proper Fourier transformation. And threshold settings are introduced for the calculation of the response function. Lastly, the time-jitter is going to be eliminated with the time-jitter noise density function that is measured from the raw data. After having processes, the refined response functions will be used for the analysis. We observed the thickness dependency of

the piezo-transducer response, good linear response range for the piezo transducers, and the limitation of the electronics at high frequency ranges within the 400MHz and 1.5V inputs.

Structure

The Chapter 2 aims to provide a mathematical model for the Nuclear Forward Scattering (NFS) of a single Mössbauer target and the effect of motion on the observables. This chapter will start with the ^{57}Fe's energy structure, Mössbauer scattering, and then it will introduce delocalized scattering for the NFS. A semi-classical model will be brought to explain the observables of the NFS of motionless target. The NFS matrix will be introduced to account for the polarization dependent scattering of the hyperfine irons and future usage. As a last part of the background part, we will formulate the NFS of moving target and understand how the motion affects the time intensity and spectrum.

The Chapter 3 proposes a scheme to shape the Mössbauer scattering field into pulses in hard X-rays. Our scheme employs two Mössbauer targets that can interfere or beat depending on their motions. With the equation of the NFS time intensity, we will formulate the arriving field over the entire measurement time as well as the generated pulse. The intensity equations will enable us to discuss the properties and limitations of the generated pulses regarding their maximum pulse intensity, pulse-to-pulse delay, pulse duration, and conditions for motions. Lastly, one application of improving the pulse's relative intensity will make up the last part of the waveform shaping project. Introducing hyperfine interacting iron targets in certain configurations, the undesired intensity at wings of pulse can be suppressed at the time periods before and after the generated pulse. In the same fashion, the analysis of the scattering field will be followed to discuss its properties, improvements, and limitations.

The Chapter 4 is motivated to understand the existing errors of the motion system. Specifically, the project focuses on part of motion systems: the electronic response of the piezo transducer and the relevant electronics, which don't require photons, unlike displacement measurement. The measurements are carried with the already-set electronics in the laboratory to prepare and test the piezo transducers for the past beamtimes [54]. To understand the raw data, the first section will be dedicated to explaining the configurations of the pre-set electronics. The specification of each unit as well as the experiment variables (piezo transducers, and tested input functions) will be introduced during the discussion. The electronic response of the system and piezo transducer will be studied with the response function in the frequency domain. The process to calculate the response function from the raw data will be presented in the following order: Averaging, data length selection, response function calculation with threshold, and time-jitter noise elimination. With the data, the thickness dependent linear response of the piezo transducer is confirmed within 400MHz and 1.5V input voltages.

Chapter 2

Background: Nuclear forward scattering of ^{57}Fe

The ^{57}Fe is one of the Mössbauer activate elements which shows a nuclear resonant scattering, i.e. Mössbauer scattering [56, 57]. Its long lifetime corresponds to a narrow transition in the frequency, neV level for the ^{57}Fe's example and has a large potential to be used in various scientific fields [58, 59, 60]. Despite its attractive feature, direct observation of nuclear transition had prevented early research in the laboratory because of the huge momentum recoil that the nucleus exchanges with photons during absorption and re-emission. The key feature of Mössbauer isotopes is that their scattering process is free from the huge recoil problem. The reason for the recoilless scattering can be found in the nucleus embedded in the crystal [56, 61]. When the Mössbauer isotopes are prepared as a solid state, the exchanged momentum is no longer delivered to the single nucleus. Instead, the entire crystal is rebound back and consequently, the recoil momentum gives only a negligible effect due to the macroscopic mass of the crystal.

The object of the background chapter is to understand the scattering of the Mössbauer nuclei, specifically ^{57}Fe. The scattering process of interest is the coherent resonant scattering where the dipole radiation explains the scattering process [62, 63]. Because of the coherent resonant scattering of Mössbauer nuclei, its property and environment make the scattering take place via several paths, quantum mechanically. The semi-classical model can describe such propagation effect [54]. Therefore, the energy structure of the ^{57}Fe is put at the beginning to see the 2-level system approximation for the semi-classical description, Section 2.1.1. The classical field will be introduced to describe the propagation through a medium with the quantum nuclear dipole moment, Section 2.2.2. The introduced model is a universal model which can be adaptable to many similar systems [64]. Then, the Nuclear forward scattering matrix is introduced in Section 2.2.3 to include the polarization dependent scattering of iron with hyperfine structure [65]. The last section, Section 2.4, will discuss the effect of the motion on the scattering field which benefited from the timely separated scattering field in the synchrotron Mössbauer experiment[53, 57].

2.1 Nuclear excitation of ^{57}Fe

To understand the existing scattering process in the ^{57}Fe, it is necessary to understand the energy structure of the nucleus.

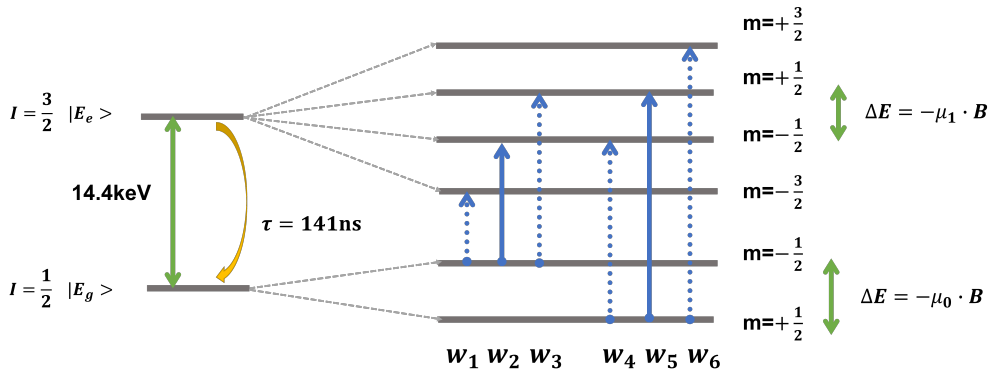

Figure 2.1: The figure shows a schemactic energy structure of the ^{57}Fe, reconstructed figure in [67]. Under the hyperfine interaction, the ground state and excited state split into 2 and 4 different states, respectively.

2.1.1 Energy structure of ^{57}Fe

The nuclear energy state is determined by its internal nuclear interactions. One excited state of ^{57}Fe can be characterized by three quantum numbers: the energy E, the nuclear spin I, and its spin orientation along the quantization axis, I_z. The ground state of ^{57}Fe is comprised of all paired nuclear spins except one unpaired nucleon due to its odd mass number [57, 66]. Ground state, I=1/2, can undergo a transition to one of the excited states if the transition satisfies the spin and energy conservation law. The interaction with resonant photon breaks one of the paired nucleon spins of the nuclear ground state and it produces the excited state which has three unpaired nuclear spin configurations, I=3/2 [57, 66]. The probability of an absorption event, in the absence of Hyperfine interaction, can be quantified with the cross-section of resonant nuclear scattering, $\sigma_0 = 2.464 \times 10^{-18}$ cm^{-2} for the ^{57}Fe [57, 66]. Comparing to the total electronic absorption cross-section of ^{57}Fe, 5.75×10^{-21} cm^{-2}, nuclear resonant excitation is the most dominant phenomena at the 14.4keV X-ray energy level.

The nuclear energy state of the iron can be assumed as an almost perfect two-level system. The first excited state is separated by $E_0 = 14.4$keV or equivalently $\lambda_0 = 0.861$Å from the ground state. A striking feature of the excited state of the ^{57}Fe is its long lifetime, $\tau = 141$ns or the ultranarrow linewidth $\gamma = 4.66$neV in the spectrum [57]. Furthermore, the degenerated energy states of ^{57}Fe are split into hyperfine energy states, respectively.

The isomer shift, quadrupole electric moment, and the nuclear Zeeman interactions are the most common interactions [41, 57]. The ^{57}Fe in our interest is the ferromagnetic ^{57}Fe, showing 33T of internal magnetic field. The randomly oriented magnetic dipole moment of such ^{57}Fe can be aligned with the external magnetic field [68], and can imprint hyperfine interaction in the observables. For such ^{57}Fe, the ground state splits into two states with quantum number $m = -1/2$ and $m = 1/2$

Label	Transitions: $\|I, I_z\rangle$	Polariziation	ΔE	C_γ
ω_1	$\|\frac{1}{2}, -\frac{1}{2}\rangle \rightarrow \|\frac{3}{2}, -\frac{3}{2}\rangle$	$\Delta m_z = -1$	ω_0 - 53.6γ	1
ω_2	$\|\frac{1}{2}, -\frac{1}{2}\rangle \rightarrow \|\frac{3}{2}, -\frac{1}{2}\rangle$	$\Delta m_z = 0$	ω_0 - 31.1γ	$\sqrt{2/3}$
ω_3	$\|\frac{1}{2}, -\frac{1}{2}\rangle \rightarrow \|\frac{3}{2}, +\frac{1}{2}\rangle$	$\Delta m_z = 1$	ω_0 - 8.6γ	$\sqrt{1/3}$
ω_4	$\|\frac{1}{2}, +\frac{1}{2}\rangle \rightarrow \|\frac{3}{2}, -\frac{1}{2}\rangle$	$\Delta m_z = -1$	ω_0 + 8.6γ	$\sqrt{1/3}$
ω_5	$\|\frac{1}{2}, +\frac{1}{2}\rangle \rightarrow \|\frac{3}{2}, +\frac{1}{2}\rangle$	$\Delta m_z = 0$	ω_0 + 31.1γ	$\sqrt{2/3}$
ω_6	$\|\frac{1}{2}, +\frac{1}{2}\rangle \rightarrow \|\frac{3}{2}, +\frac{3}{2}\rangle$	$\Delta m_z = 1$	ω_0 + 53.6γ	1

Table 2.1: Parameters of M1 transitions of ^{57}Fe with 33T internal magnetic field are presented in increasing energy order. The $|I, I_z\rangle$ basis is chosen to represent the ground and excited state. The new parameter C_γ is the Clebsch Gordan coefficient which represents the relative strength for each transition. [67]

separated by $-\mu_0 \cdot B = 39.7\gamma$ for $(B = 33T)$. And the excited state splits into four equally separated states $m = 3/2$ to $m = -3/2$ but by $\mu_1 \cdot B = 22.4\gamma$ for $(B = 33T)$ [67]. The M1 transition of the ^{57}Fe allows only sextet transitions $\Delta m = -1, 0, 1$ to obey spin conservation.

2.1.2 Delocalized nuclear excitation and Nuclear Forward Scattering(NFS)

The study of the nuclear state of the ^{57}Fe is often carried out with the synchrotron radiation that produces less than one resonant photon at each pulse, on average, due to its low number of photon per mode and ultranarrow linewidth of ^{57}Fe [30].

When a resonant photon is incident to a crystal where ^{57}Fe nuclei are embedded, one of the nuclei will absorb the photon without recoil and re-emit it at a later time. The relevant scattering is the dipole radiation of the nucleus which features a coherent evolution of the state and the radiation [69]. This type of scattering process can take place for the ^{57}Fe in $14,4$keV [54], or generally the nuclear excitation. Since the scattering is coherent and elastic, the final state of the nucleus is returned to exactly the same state as the other nucleus after completing the scattering [57]. Then, such scattering conditions set a delocalized scattering since spatial information of the scattering center is not known before and after the scattering. The nuclear-photon interaction needs to be expressed as a superposition of all nuclei in the target, quantum mechanically, and the scattered field is also required to be expressed as the superposition of respective scattering paths [57, 62, 63]. The feature of the delocalized scattering field is the scattering direction from the interferences of each path. The forward and backward scattering direction is the universal scattering direction observed for all Mössbauer targets, where the scattering propagating to forward direction is called Nuclear Forward Scattering (NFS) [42, 70]. While there are non-zero scattering amplitudes along the Bragg's direction for periodic crystals. The delocalized nuclear scattering concept is independently developed by Hannon and Kagan, named as nuclear exciton [63] and nuclear polariton [62], respectively.

2.2 Semi-classical model for Nuclear forward scattering

The NFS of ^{57}Fe can be described by the semi-classical model, where a quantum state for the nucleus and a classical field are assumed.

2.2.1 Master equation

From the energy structure of the ^{57}Fe, it encourages modeling the ^{57}Fe as a two-level system for the nuclear-field interaction.

Master equation

Generally, the wavefunction of a two-level system can be expressed as,

$$|\psi\rangle = \sum_{i=e,g} c_i |i\rangle, \tag{2.1}$$

where e, g refer the excited state and ground state, respectively

The density operator of the given system is defined as,

$$\hat{\rho} = |\psi\rangle \langle\psi| \tag{2.2}$$

The interaction of one two-level system and a light field is described by the master equation [64]. The interaction is described as the evolution of the given system,

$$\partial_t \hat{\rho}(t) = \frac{1}{i\hbar} \left[\hat{H}, \hat{\rho}\right] + \hat{\rho}_s, \tag{2.3}$$

where $\hat{\rho}$ is a density matrix defined as Eq. (2.2). And $\hat{H}$ is interaction hamiltonian of the system with toghether describes the coherent evolution of the state. While $\hat{\rho}_s$ operator (decoherence matrix) describes the decoherence effect such as the spontaneous emission.

Explicitly, the nuclear states will have the following form in the interaction picture.

$$\hat{\rho} = \begin{pmatrix} \rho_{gg} & \rho_{ge} \\ \rho_{eg} & \rho_{ee} \end{pmatrix} = \begin{pmatrix} |c_g|^2 & c_e {c_g}^* \\ c_g {c_e}^* & |c_e|^2 \end{pmatrix} \tag{2.4}$$

$$\hat{\rho}_s = \frac{\Gamma}{2} \begin{pmatrix} 2\rho_{ee} & -\rho_{ge} \\ -\rho_{eg} & -2\rho_{ee} \end{pmatrix} \tag{2.5}$$

$$\hat{H}_{int} = -\frac{\hbar}{2} \begin{pmatrix} 0 & \Omega_p^* \\ \Omega_p & 2\Delta_p, \end{pmatrix} \tag{2.6}$$

where the Δ_p is the detuning between the natural frequency of the nucleus and the incident field. The Rabi frequency is defined as $\Omega_p = \frac{1}{\hbar} \langle e| \hat{H}_{int} |g\rangle = \frac{1}{\hbar} \langle e| \hat{d} \cdot E |g\rangle$

indicating the coupling amplitude of the field-nucleus interaction. The operator $\hat{d}$ is the dipole moment operator of the nucleus defined as $\hat{d} = e \cdot \hat{r}$ with position operator $\hat{r}$.

Each component of the Eq. (2.3) is given by,

$$\partial_t \rho_{gg} = \Gamma \rho_{ee} + \frac{i}{2}(\Omega_p^* \rho_{eg} - \Omega_p \rho_{eg}^*) \tag{2.7}$$

$$\partial_t \rho_{eg} = -(\frac{\Gamma}{2} - i\Delta_p)\rho_{eg} - \frac{i}{2}\Omega_p(\rho_{ee} - \rho_{gg}) \tag{2.8}$$

$$\partial_t \rho_{ee} = -\Gamma \rho_{ee} + \frac{i}{2}(-\Omega_p^* \rho_{eg} + \Omega_p \rho_{eg}^*) \tag{2.9}$$

$$\rho_{ge} = \rho_{eg}^* \tag{2.10}$$

We can read the the conservation law, $\partial_t \rho_{gg} + \partial_t \rho_{ee} = 0$, universally. Furthermore, exponential decay of excited state, $\rho_{ee} = |c_e|^2 \sim e^{-\Gamma t}$, and decay of coherences of the nuclear system (two-level system), $\rho_{ge} \sim e^{-\Gamma/2t}$, are observed when pumping field doesn't exist.

2.2.2 Maxwell-Bloch equation

Our interest is in how the field is changed after propagating through the nuclear system. To answer this question we need to combine the Master equation with Maxwell's wave equation.

First order wave equation The behavior of the electromagnetic field is completely determined by the set of Maxwell's equations. When the electric field and magnetic field exist in the medium, each field is represented as the sum of the external field and an induced internal field [69].

The propagation equation of the electromagnetic field through dielectric material is given as [69],

$$\overrightarrow{\nabla} \times (\overrightarrow{\nabla} \times \overrightarrow{E}) + \mu_0 \epsilon_0 \partial_{tt} \overrightarrow{E} = -\mu_0 \partial_{tt} \overrightarrow{P}, \tag{2.11}$$

where the $\overrightarrow{E}$ is the electric field. The Polarization, $\overrightarrow{P}$, represents the induced electric field of the given system. It is the averaged dipole moments over a sizable area of the medium. The detailed derivation is presented in Appendix A.1.

The following equation solves the wave equation along the z-direction

$$E(z,t) = \frac{1}{2}\mathcal{E}(z,t)e^{i(kz - \nu t + \phi(z,t))} + c.c, \tag{2.12}$$

where the envelope of the electric field, $\mathcal{E}(z,t)$, and the phase $\phi(z,t)$ are assumed to slowly vary [71, 72]. The induced electric field in the medium can be also written in a similar fashion.

$$P(z,t) = \frac{1}{2}\mathcal{P}(z,t)e^{i(kz - \nu t + \phi(z,t))} + c.c, \tag{2.13}$$

Recalling the macroscopic object, the Polarization, is defined as the averaged dipole moment over a sizable area in classical electromagnetic dynamics, it is attempting to introduce a quantum mechanical counterpart for the Polarization to figure out the propagation effect of the nuclear 2-level system. The multiplication of the total number of dipoles and the expectation value of a single quantum dipole moment can fulfill the quantum mechanical expression [64, 73],

$$\mathcal{P} = N \left\langle \hat{d} \right\rangle = N \times tr(\hat{\rho}\hat{d}) = 2Nd_{eg}\rho_{eg}(t) \tag{2.14}$$

The second-order Maxwell's wave equation reduces to the first-order differential equation, details in Appendix A.1. And applying slowly varying approximations,

$$(\partial_z + \frac{1}{c}\partial_t)(\mathcal{E}e^{i\phi(z,t)}) \simeq i\frac{k}{2\epsilon_0}\mathcal{P} \tag{2.15}$$

$$= i\frac{2\pi}{\epsilon_0\lambda}Nd_{eg}\rho_{eg}(t), \tag{2.16}$$

where the last equation replaces one classical object with the quantum mechanical observable.

Coherent propagation effect

The discussion keeps assuming that both electric field and polarization will be parallel. Multiplying $\frac{d_{eg}}{\hbar}$ at both sides of the equation, the following equation comes out,

$$(\partial_z + \frac{1}{c}\partial_t)\Omega_p = i\frac{2\pi}{\lambda\hbar\epsilon_0}N\rho_{eg}|d_{eg}|^2 \equiv i\eta\rho_{eg}, \tag{2.17}$$

where $\Omega_p = \frac{1}{\hbar}(d_{eg} \cdot E)$ is the Rabi frequency. The η is defined as $\frac{\xi\Gamma}{2L}$ with $\xi = N\sigma L$. The resonant cross section of nuclear scattering is $\sigma = \frac{4\pi|d_{eg}|^2}{\hbar\epsilon_0\lambda\Gamma}$ [71, 72].

Together with the Master equation, the first-order Maxwell's equation can describe the scattering of a nuclear ensemble with proper boundary conditions. We assume that the nuclear state is prepared in a ground state, $\rho_{ij}(t=0) = \delta_{gi}\delta_{jg}$. Another condition is that the Rabi frequency is also zero inside the material at time zero, $\Omega_p(t=0,z) = 0$. And the Rabi frequency satisfies $\Omega_p(t, z=0) = \delta(t-\tau)$ at the boundary of the nuclear ensemble.

Assuming weak nuclear-field interaction, $\Omega_p \ll \Gamma$, for the nucleus system, it is possible to treat the interaction strength Ω_p and consequent nuclear state $\rho_{ij}(t)$ as a perturbation in the equations from Eq. (2.7) to Eq. (2.9), and Eq. (2.17) [72].

First, let's introduce κ to understand the order of perturbations.

$$\rho_{eg}(t) = \kappa\rho_{eg}(t)$$
$$\Omega_p(t) = \kappa\Omega_p(t)$$

Then, the following set of equations is obtained.

$$\kappa\partial_t\rho_{gg}(t) = \Gamma\kappa\rho_{ee}(t) + \frac{i}{2}\kappa^2(\Omega_p^*(t)\rho_{eg}(t) - \Omega_p(t)\rho_{eg}^*(t))$$
$$\kappa\partial_t\rho_{ee}(t) = -\Gamma\kappa\rho_{ee}(t) + \frac{i}{2}\kappa^2(\Omega_p(t)\rho_{eg}^*(t) - \Omega_p^*(t)\rho_{eg}(t))$$
$$\kappa\partial_t\rho_{eg}(t) = -\kappa(\frac{\Gamma}{2} - i\Delta_p)\rho_{eg}(t) + \frac{i}{2}\kappa\Omega_p(t) - \frac{i}{2}\kappa^2\Omega(\rho_{ee}(t) - \rho_{gg}(t))$$
$$\kappa\frac{1}{c}\partial_t\Omega_p(t) + \kappa\partial_z\Omega_p(t) = i\kappa\eta\rho_{eg}(t)$$

Neglecting the terms higher than $O(\kappa)$, a linear set of differential equations is obtained.

$$\partial_t\rho_{gg}(t) = \Gamma\rho_{ee}(t) \tag{2.18}$$
$$\partial_t\rho_{ee}(t) = -\Gamma\rho_{ee}(t) \tag{2.19}$$
$$\partial_t\rho_{eg}(t) = -(\frac{\Gamma}{2} - i\Delta_p)\rho_{eg}(t) + \frac{i}{2}\Omega_p(t) \tag{2.20}$$
$$\frac{1}{c}\partial_t\Omega_p(t) + \partial_z\Omega_p(t) = i\eta\rho_{eg}(t) \tag{2.21}$$

The last two linear differential equations compose a set of propagation equation from which the coherence of the nuclear system and electric field can be solved. The set of differential equations is represented in the frequency space to easy solution.

$$-i\omega\rho_{eg}(\omega, z) = -(\frac{\Gamma}{2} - i\Delta_p)\rho_{eg}(\omega, z) + \frac{i}{2}\Omega_p(\omega, z) \tag{2.22}$$
$$-i\frac{\omega}{c}\Omega_p(\omega, z) + \partial_z\Omega_p(\omega, z) = i\eta\rho_{eg}(\omega, z) \tag{2.23}$$

The following $\rho_{eg}(\omega, z)$ solves the above equation.

$$\rho_{eg}(\omega, z) = \frac{-1/2}{\omega + \Delta_p + i\Gamma/2}\Omega_p(\omega, z) \tag{2.24}$$

Substituting $\rho_{eg}(\omega, z)$, the calculation of remained the Rabi frequency is also easily followed as,

$$\Omega_p(\omega, z) = e^{\frac{-i\eta z/2}{\omega+\Delta_p+i\Gamma/2}} \times \Omega_p(\omega, 0)e^{i\frac{\omega}{c}z} = R(\omega)E_0(\omega, z) \tag{2.25}$$

To find the scattered field equation, it needs to transform the Rabi oscillation into time space.

$$\Omega_p(t, z) = \frac{1}{2\pi}\int dw \times \Omega_p(\omega, z)e^{-iw(t-z/c)} \tag{2.26}$$

With the definition of the Rabi frequency, $\Omega_p(t, z) = \frac{1}{\hbar}(E \cdot d_{eg})$, the scattering field is as followed.

$$
\begin{aligned}
E(t,z) &= \frac{1}{2\pi}\int E(\omega,0)e^{\frac{-i\eta z/2}{\omega+\Delta_p+i\Gamma/2}}e^{-i\omega(t-z/c)}d\omega \\
&= \frac{1}{2\pi}\int \big(\mathcal{E}(w,z)e^{-i\nu(t-z/c)}\big)(\omega,0)e^{\frac{-i\eta z/2}{\omega+\Delta_p+i\Gamma/2}}e^{-i\omega(t-z/c)}d\omega \\
&= \frac{1}{2\pi}\int \mathcal{E}(\omega,0)e^{\frac{-i\eta z/2}{\omega-\omega_0+i\Gamma/2}}e^{-i\omega(t-z/c)}d\omega, \qquad (2.27)
\end{aligned}
$$

where the definition of detuning $\Delta_p = \nu - \omega_0$ is used and defined envelope for electric field (Eq. (2.12)) is substituted in the second equation. And the integral variable is re-defined as $\omega + \nu \equiv \omega$ at the last equation.

Taylor expanding the exponential inside integral,

$$
\begin{aligned}
E(t,z) &= \frac{1}{2\pi}\int \mathcal{E}(\omega,0)\sum_{n=0}^{\infty}(1+\frac{1}{1!}(\frac{-ib}{\omega-\omega_0+i\gamma})^1+\cdots)e^{-i\omega(t-z/c)}d\omega \\
&= \frac{1}{2\pi}\int e^{-i\omega(t-z/c)}d\omega + \sum_{n=1}^{\infty}\frac{1}{2\pi}\frac{1}{n!}\int(\frac{-ib}{\omega-\omega_0+i\gamma})^n\times e^{-i\omega(t-z/c)}d\omega, \qquad (2.28)
\end{aligned}
$$

where the new variables, $\gamma = \Gamma/2$ and $b = \eta z/2$, are introduced and $\delta(t)$-like incident pulse is assumed at the last equation [71].

The Cauchy's residual theorem evaluates the second integral of the last equation [71].

$$
\begin{aligned}
&\oint(\frac{-ib}{\omega-\omega_0+i\gamma})^n\times e^{-i\omega(t-z/c)}d\omega \\
&= -i\times(-ib)^n\mathrm{Res}[\frac{e^{-i\omega(t-z/c)}}{(\omega-\omega_0+i\gamma)^n}] \\
&= -i\times(-ib)^n\frac{(-i\omega(t-z/c))^{n-1}}{(n-1)!}e^{-\gamma(t-z/c)}e^{-i\omega_0(t-z/c)}
\end{aligned}
$$

Substituting the result of the contour integral, the electric field is given by,

$$
\begin{aligned}
E(t,z) &= \delta(t-z/c)+\sum_{n=1}^{\infty}\frac{(-i)^{2n}}{n!(n-1)!}(t-z/c)^{n-1}b^n e^{-\gamma(t-z/c)}e^{-i\omega_0(t-z/c)}\theta(t-z/c) \\
&= \delta(t-z/c)+b\frac{J_1(2\sqrt{b(t-z/c)})}{\sqrt{b(t-z/c)}}e^{-\gamma(t-z/c)}e^{i\omega(b(t-z/c))}\theta(t-z/c), \qquad (2.29)
\end{aligned}
$$

where the last equation uses the first kind Bessel-function definition [74, 75].

Discussion about the semi-classical model

The result of the semi-classical approach explains the direction of the scattering field and its result is consistent with the measured time intensity in the NFS experiment

[62, 70, 74]. The successful description of the NFS is possible because, first, narrowing down the field near the resonant frequency, the given synchrotron pulse can be treated as a weak classical field since it only produces less than one resonant photon on average [30]. It is available to describe the propagation of a light field through the resonant medium with the Maxwell's equation and nuclear dipole moment [54]. Second, considering the delocalized nuclear excitation in Section 2.1.2, the collective effect is reflected when we consider the refractive index, in Eq. (2.14) [72]. The Maxwell-Bloch equation assumed that all nuclei are homogeneous and thus, the refractive index is represented as the sum of the dipole moments of homogeneous nuclear dipole moments.

2.2.3 Nuclear forward scattering matrix

Although phenomenologically the time intensity is well explained by the Eq. (2.29), more properties can be found in Mössbauer nucleus' NFS than the simple model predicts. For example, the NFS can take place via different scattering channels and can even involve an electronic contribution. To encounter the NFS thoroughly, it is required to extend the idea into a more general method.

2.2.3.1 General description for scattering

The new method will also describe the propagation effect in terms of the refractive index. To define the refractive index for the nucleus, it needs to keep assuming a homogeneous nuclear ensemble for the scattering [57]. Then, the scattering can be described with the refractive index matrix, generally [75, 76].

$$\boldsymbol{\eta} = 1 + \frac{2\pi}{{k_0}^2} \sum \rho_i \mathbf{M_i} \tag{2.30}$$

The refractive index matrix, $\boldsymbol{\eta}$, contains all possible scattering channels. Each individual channel, represented as a scattering matrix $\mathbf{M_i}$, which is weighted by the number density of the scatterer, written in ρ_i, that can undergo the $\mathbf{M_i}$ scattering process [57]. The sum of weighted scattering enables us to consider all existing scattering for the nuclear system. A newly defined refractive index matrix will be used to describe the propagation effect on the electric field.

$$\begin{aligned} & E(z+\Delta z) - E(z) = i\boldsymbol{\eta} E(z)\Delta z \\ \rightarrow \;& E(z) = e^{i\boldsymbol{\eta} z} E(0) \end{aligned} \tag{2.31}$$

2.2.3.2 Nuclear forward scattering matrix

The NFS is described by the NFS matrix, $\mathbf{F}(\omega)$, corresponding to $\boldsymbol{\eta}$ in Eq. (2.30) [57, 65]. The NFS matrix contains information on the number density of nuclear ensemble and possible scattering paths. The forward scattering matrix is usually a 2x2 matrix to include two polarization dependent scattering processes. It can be divided into an electronic scattering matrix and a nuclear scattering matrix.

$$\mathbf{F}(\omega) = \mathbf{E}(\omega) + \mathbf{N}(\omega), \tag{2.32}$$

where $\mathbf{N}(\omega)$ and $\mathbf{E}(\omega)$ indicates scattering off of nucleus and electrons, repsectively.

The electronic scattering matrix is defined as [57, 65],

$$\mathbf{E}_{\mu\nu}(\omega) = (\epsilon_\mu \cdot \epsilon_\nu)[-Zr_0 + \frac{ik_0}{4\pi}\sigma_e(\omega)], \tag{2.33}$$

where ϵ_μ and ϵ_ν refer the polarization direction of the fields. Z is the Atomic number and r_0 is the classical electron radius, and σ_e is the total absorption cross section of electrons.

The nuclear part of the scattering matrix is written as, for 2^L-pole transitions [57, 65],

$$\mathbf{N}_{\mu\nu}(\omega) = \frac{4\pi f_{LM}}{k_0}(\epsilon_\mu \cdot Y_{LM}(k_0))(Y^*_{LM}(k_0) \cdot \epsilon_\mu)F_{LM}(\omega) \tag{2.34}$$

The f_{LM} is the recoilless fraction, called the Lamb-Mössbauer factor. The anisotropic scattering process, different refractive indices for different scattering channels, is described by the spherical harmonics $Y_{LM}(k_0)$ and its inner product with polarization vector. Here $Y_{LM}(k_0)$ is the vector spherical harmonic function which is used to represent the nuclear state to best use its spherical symmetry. The F_{LM} is the part describing the energy dependence of nuclear transition.

$$F_{LM}(\omega) = \sum_{\alpha,n} \frac{p_\alpha p_\alpha(\eta)\Gamma(\alpha M\eta; L)}{E(\eta) - E(\alpha) - \hbar\omega - i\Gamma(n)/2} \tag{2.35}$$

The quantity F_{LM} includes all information on possible transitions of the nuclear system under the study [57, 65]. The α denotes all initial states while η indicates potential excited states. p_α represents a probability for the α state to be occupied. And $p_\alpha(n)$ is the conditional probability for the state η is empty while the state α is occupied. Lastly, $\Gamma(\alpha M\eta; L)$ describes one single scattering process from the α state to the η state after experiencing M magnetic quantum number changes via 2^L-multipole. And $\Gamma(\eta)$ stands for the full resonance width.

2.2.3.3 Nuclear forward scattering matrix of ^{57}Fe

The M1 transition is in particular interest for the Mössbauer isotope ^{57}Fe [57, 65]. The M1 transition set variables to L=1 for $F_{LM}(\omega)$, and requires to replace ϵ by $\epsilon \times k_0$ at the Eq. (2.34), where k_0 is the unit vector of the photon propagation axis.

$$\begin{aligned}\mathbf{N}_{\mu\nu}(\omega) = \frac{3}{16\pi}&\big((\epsilon_\mu \times k_0) \cdot (\epsilon_\nu \times k_0)\big)(F_1 + F_{-1}) \\ &- i\big(((\epsilon_\mu \times k_0) \times (\epsilon_\nu \times k_0)) \cdot \mathbf{m}\big)(F_1 - F_{-1}) \\ &+ \big((\epsilon_\mu \times k_0) \cdot \mathbf{m}\big)\big((\epsilon_\nu \times k_0) \cdot \mathbf{m}\big)(2F_0 - F_1 - F_{-1}),\end{aligned} \tag{2.36}$$

where one can read the magnetization sensitive matrix components, in our case nuclear magnetic dipole moment. The first component is independent of nuclear magnetic dipole moment. The second term causes a dichroic propagation effect for the circularly polarized light. And the last term indicates a linear dichroic scattering channel for a similar reason.

Newly introduced F_1, F_0, F_{-1} are transition amplitudes of excitations with $\Delta\mathbf{m} = -1, 0, 1$, in order.

$$F_1 = f_{LM}(\frac{1}{1+\alpha})(\frac{1}{2j_0+1})(|C_{-1}|^2\frac{\Gamma}{\hbar(\omega_1-\omega)-i\Gamma/2} + |C_1|^2\frac{\Gamma}{\hbar(\omega_4-\omega)-i\Gamma/2}) \tag{2.37}$$

$$F_0 = f_{LM}(\frac{1}{1+\alpha})(\frac{1}{2j_0+1})(|C_0|^2\frac{\Gamma}{\hbar(\omega_2-\omega)-i\Gamma/2} + |C_0|^2\frac{\Gamma}{\hbar(\omega_5-\omega)-i\Gamma/2}) \tag{2.38}$$

$$F_{-1} = f_{LM}(\frac{1}{1+\alpha})(\frac{1}{2j_0+1})(|C_1|^2\frac{\Gamma}{\hbar(\omega_3-\omega)-i\Gamma/2} + |C_{-1}|^2\frac{\Gamma}{\hbar(\omega_6-\omega)-i\Gamma/2}) \tag{2.39}$$

The parameters C_γ are Clebsch Gordan coefficients reflecting different coupling amplitudes for nuclear excitations (ω_i, values in Table 2.1). The $\alpha = 8.21$ is the internal conversion coefficient, $f_{LM} = 0.86$ is the recoilless fraction, and $j_0 = 1/2$ indicates the spin quantum number of the nuclear ground state [57, 65].

With a choice of basis, it is possible to explicitly represent the nuclear scattering matrix of ^{57}Fe. The most popular basis is defined on the orthogonal plane of the propagation axis. A set of virtual two orthogonal linear axes on the plane, $\{\hat{\sigma}, \hat{\pi}\}$, are frequently chosen for the experiment.

$$\mathbf{N}(\omega) = \begin{pmatrix} \mathbf{N}_{\sigma\sigma} & \mathbf{N}_{\sigma\pi} \\ \mathbf{N}_{\pi\sigma} & \mathbf{N}_{\pi\pi,} \end{pmatrix} \tag{2.40}$$

where

$$\mathbf{N}_{\sigma\sigma} = \frac{3}{8}\frac{\lambda}{2\pi}p\{F_1 + F_{-1} + (\pi\cdot\mathbf{m})^2(2F_0 - F_1 - F_{-1})\} \tag{2.41}$$

$$\mathbf{N}_{\sigma\pi} = \frac{3}{8}\frac{\lambda}{2\pi}p\{-i(k_0\cdot\mathbf{m})(F_1 - F_{-1}) + (\hat{\pi}\cdot\mathbf{m})(\hat{\sigma}\cdot\mathbf{m})(2F_0 - F_1 - F_{-1})\} \tag{2.42}$$

$$\mathbf{N}_{\hat{\pi}\sigma} = \frac{3}{8}\frac{\lambda}{2\pi}p\{+i(\hat{k_0}\cdot\mathbf{m})(F_1 - F_{-1}) + (\hat{\pi}\cdot\mathbf{m})(\hat{\sigma}\cdot\mathbf{m})(2F_0 - F_1 - F_{-1})\} \tag{2.43}$$

$$\mathbf{N}_{\pi\pi} = \frac{3}{8}\frac{\lambda}{2\pi}p\{F_1 + F_{-1} + (\hat{\sigma}\cdot\mathbf{m})^2(2F_0 - F_1 - F_{-1})\} \tag{2.44}$$

The scattering matrix shows clear polarization mixing effects depending on the magnetic dipole moment alignment [57, 65]. For example, two scattering paths, $\mathbf{N}_{\sigma\sigma}$ and $\mathbf{N}_{\sigma\pi}$, explain scatterings scatter off in $\hat{\sigma}$ polarization from the same $\hat{\sigma}$ and $\hat{\pi}$ polarization component of the incident field. Further, p is used to consider different

polarity between the excited state and the ground state, where the M1 transition has $p = 1$.

$$p = (-1)^L \text{ for } 2^L \text{ electric transition}$$
$$p = (-1)^{L+1} \text{ for } 2^L \text{ magnetic transition}$$

2.3 Measurables of static ^{57}Fe target

We investigated the quantum mechanical models for the NFS of the ^{57}Fe. Often, the NFS predicts a complicated spectrum due to its polarization dependent scattering. Assuming vanishing Hyperfine interactions for a simple discussion, off-diagonal components of the NFS matrix become zero. The stainless steel, $Fe_{55}Cr_{25}Ni_{20}$, shows vanishing hyperfine interactions [57, 77]. Then, it enables us to describe the scattering independently as follows:

$$E_\sigma(\omega, d) = e^{iN_{\sigma\sigma}d} E_\sigma(\omega, 0) \tag{2.45}$$

$$E_\pi(\omega, d) = e^{iN_{\pi\pi}d} E_\pi(\omega, 0), \tag{2.46}$$

where $E_{\hat{i}}(\omega, d)$ indicates the scattered field in $\hat{i}$ polarization state.

The target is prepared in a way that its virtual $\hat{\sigma}$ axis is parallel to the polarization direction of synchrotron pulse [30]. Such preparation will simplify the discussion since the incident field has no components on $\hat{\pi}$ direction, $E_\pi(\omega, 0) = 0$. Then it degenerates existing six transitions into one for the ^{57}Fe, all $\omega_i = \omega_0 = 14.4$keV, and consequently $F_1 = F_0 = F_{-1}$ [65].

Explicitly,

$$\begin{aligned} E(\omega, d) &= e^{i\Gamma_c[\frac{1}{\hbar(\omega_0-\omega)-i\Gamma/2}]d} E(\omega, 0) = e^{\frac{-ib}{\hbar(\omega-\omega_0)+i\gamma}} E(\omega, 0) \\ &= R(w)E(w, 0) \\ &= \underbrace{1}_{\text{non interacting part}} + \underbrace{(R(w) - 1)}_{\text{scattered part}} = 1 + T(w), \end{aligned} \tag{2.47}$$

where $\gamma = \Gamma/2$ and $b = \Gamma_c d$. The Γ_c is the enhanced decay width defined as $\frac{\lambda}{2\pi} f_{LM} \frac{1}{1+\alpha} \frac{1}{2j_0+1} \Gamma$. The $R(w)$ is defined as $e^{\frac{-ib}{\hbar(\omega-\omega_0)+i\gamma}}$, which has transition information and is named as NFS response function. The last equation assumed the synchrotron pulse for an incident pulse, $E(\omega, 0) = 1$, and decomposes the response function into non-interacting part($= 1$) and scattered part($= T(w)$).

Applying Fourier transformation to get the scattering field as a function of time,

$$E_{\text{rest}}(t) = \underbrace{\delta(t)e^{i\omega t}}_{\text{non-interacting part}} \underbrace{- b\frac{J_1(\sqrt{2bt})}{\sqrt{bt}} e^{-\gamma t} e^{-i\omega_0 t} \theta(t)}_{\text{scattered part}=T(t)}. \tag{2.48}$$

We can confirm that the same result is outcome for the vanishing hyperfine assumption with Eq. (2.29). The e^{ikz} is dropped in the above equation and is going to be omitted after assuming the scattered field is measured at the detector fixed in one position.

The scattering field is composed of two parts. The first part is the prompt pulse which just passed the nuclei ensemble, as written in $\delta(t)e^{i\omega t}$. The ultranarrow linewidth, $\Gamma = 4.66$neV, for the ^{57}Fe nucleus and meV frequency band of synchrotron pulse makes it possible to assume the non-interacting part remains same as the incident part. The $T(t)$ is the dipole radiation arriving after the $t > 0$. In addition to the exponential decay $e^{-\gamma t}$, the amplitude has been modulated by $b\frac{J_1(2\sqrt{bt})}{\sqrt{bt}}$, called as **Dynamical beating** [62, 63, 74]. The Dynamical beating is caused by the interference of the scattering fields radiated from the nuclei at different depths of the target.

Time intensity The time intensity as a function of time can be directly studied from Eq. (2.48).

$$I_{\text{rest}}(t) = |E_{\text{rest}}|^2 = \delta(t) + |b\frac{J_1(\sqrt{2bt})}{\sqrt{bt}}|^2 e^{-2\gamma t}\theta(t), \tag{2.49}$$

where any function multiplied with $\delta(t)$ function is re-expressed as $\delta(t)$ due to its property [78].

Agreeing with Eq. (2.49), the high intensity of synchrotron pulse locates at $t = 0$ and the pure scattering field is radiated over hundreds of nanoseconds in Fig. 2.2. The pure scattering field exhibits a clear dynamical beating feature which can be seen as a slow oscillation in which zeros at $t \approx 125$ can be observed [62, 65].

Frequency spectrum The frequency spectrum of the NFS is calculated with Eq. (2.47),

$$I_{\text{rest}}(\omega) = |R(\omega)|^2 = |e^{\frac{-ib}{\hbar(\omega-\omega_0)+i\gamma}}|^2 \tag{2.50}$$

The overall $y \approx 1$ in Fig. 2.2 features the frequency band of the synchrotron pulse. The spectrum explains a feature near $\omega = \omega_0$. The scattered field is radiated in out-of-phase with the incident field and imprints a dip feature in the spectrum. A thickness effect causes a broadened absorption spectrum, it is approximated by a Lorenztian curve if a thin target is used, $b = \Gamma_c d \ll 1$ [62, 65].

2.4 Measurables of moving ^{57}Fe target

The nuclear radiates the field over a long period of time. The relative phase of the scattering field can be modified if the position of the Mössbauer target can be controlled on the wavelength level. Considering the nanosecond time scale for the

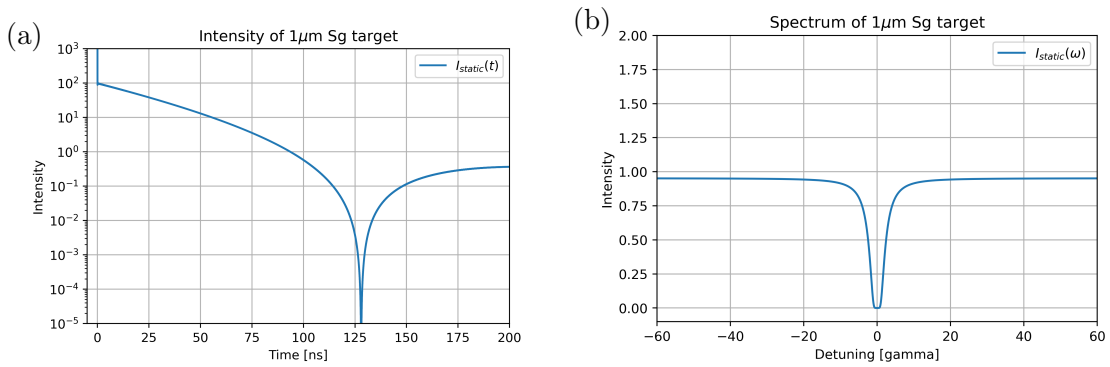

Figure 2.2: (a) The time intensity of a single target without the Hyperfine interaction is plotted. A 1μm thick target is chosen for the simulation. (b) The absorption spectrum of the same target is plotted.

Mössbauer effect and the 10^{-10}m magnitude of the X-ray wavelength, not many of them are feasible for the experiment. For this reason piezo-transducer [49, 52, 53], ultrasonic [51], and time-dependent magnetic field [70] are the most frequently chosen techniques to realize phase control. For our research, the mechanically induced phase with a piezo-transducer is chosen to study the effect of the motion on the observables. The mechanical displacement manifests the phase control by enlarging or shortening the propagation distance, e^{ikz} to $e^{ik(z+\Delta z)}$ [52, 53].

2.4.1 Phase modification of nuclear forward scattering

If the target is at rest, the position of the scattering is fixed over the scattering. When the pumping field arrives at the target, the field propagates $z_{\text{target}}(t_a) - z_{\text{source}}$ to arrive at the target. When the field is re-emitted, the scattered field propagates the distance of $z_{\text{detector}} - z_{\text{target}}(t_r)$ to arrive at the detector.

$$\underbrace{\{z_{\text{target}}(t_a) - z_{\text{source}}\}}_{\text{incident field to target}} + \underbrace{\{z_{\text{detector}} - z_{\text{target}}(t_r)\}}_{\text{scattered field tar. to det.}}$$

The total distance for the scattered field to propagate is constant if the target is not moving. Therefore the scattering field and synchrotron pulse propagates the same distance and is impinged with same phase at the detector.

However the propagation distance changes for the moving targets. The total propagation distance is modified since the position of absorption and emission is no longer the same, $z_{\text{target}}(t_a) \neq z_{\text{target}}(t_f)$. This difference in the phase can cause interference on the measurables. One method to account for the correct phase is to **describe the scattering in the target rest frame** where the position of absorption and radiation are fixed [54]. Then the scattering field will be transformed back to the lab frame to explain the intensity that the detector measures in the experiment.

Transformation matrix

Our goal in this section is to find a proper coordinate transformation between the lab frame and the target rest frame to express an electric field in a different frame.

Let's assume one observer in the lab frame measures the $E_{\mathrm{lab}}(z,t)$ and imagine one observer A in the target rest frame sees the same field as $E_{\mathrm{tar}}(z',t)$. The passive transformation of the electric field can relate two observations [69],

$$E_{\mathrm{tar}}(z',t) = (\mathbf{T^{-1}}\{E_{\mathrm{lab}}\})(\mathbf{T}\{z\},t)$$

The bold $\mathbf{T}$ represents a linear coordinate transformation between the coordinates, where often the Lorentizan transformation is used. The $\mathbf{T^{-1}}$ is the inverse transformation of the $\mathbf{T}$. The same electric field is observed as $\mathbf{T^{-1}}\{E_{\mathrm{lab}}\}$ at the new coordinate $\mathbf{T}\{z\}$. The $\mathbf{T^{-1}}\{E_{\mathrm{lab}}\}$ can be approximated to E_{lab} if the speed of the target is not comparable to the speed of the light [71].

$$E_{\mathrm{tar}}(z',t) = E_{\mathrm{lab}}(\mathbf{T}\{z\},t) = E_{\mathrm{lab}}(z-\Delta z,t) \tag{2.51}$$

Variable z' is the coordinate of the target rest frame where $\mathbf{T}\{z\} = z - \Delta z$ is held for the non-relativistic approximation ($v \ll c$).

The inverse operation is achieved in a similar fashion.

$$E_{\mathrm{lab}}(z,t) = E_{\mathrm{tar}}(\mathbf{T^{-1}}\{z'\},t) = E_{\mathrm{tar}}(z'+\Delta z,t) \tag{2.52}$$

Nuclear forward scattering with synchrotron pulse

Assuming the incident synchrotron pulse is observed by observer A in the target rest frame,

$$E^{i}_{\mathrm{tar}}(z',t) = \delta(t)e^{ik(z-\Delta z(t))}e^{-i\omega t}, \tag{2.53}$$

where superscript 'i' indicates the incident field and subscript 'tar' stands for the target rest frame.

The scattered field is described in the target rest frame as,

$$\begin{aligned} E^{\mathrm{scatt}}_{\mathrm{tar}}(z',t) &= \int R(t-\tau)\delta(\tau)e^{ik(z-\Delta z(\tau))}e^{-i\omega\tau}d\tau \\ &= R(t)e^{ikz}e^{-ik\Delta z(0)} = (\delta(t)e^{-i\omega t} + T(t))e^{ikz}e^{-ik\Delta z(0)}, \end{aligned}$$

where superscript 'scatt' notes the scattering field. The scattering response function, $R(t)$, is decomposed into non-interacting part $\delta(t)e^{\omega t}$ and interacting part $T(t)$ in the last equation.

It is required to transform into the lab frame to account for the measured intensity by the detector with Eq. (2.52).

$$\begin{aligned} E^{\mathrm{scatt}}_{\mathrm{lab}}(z,t) &= \delta(t)e^{-i\omega t}e^{ikz} + T(t)e^{ikz}e^{ik\Delta z(t)}e^{-ik\Delta z(0)} \\ &= \underbrace{\delta(t)e^{-i\omega t}e^{ikz}}_{\text{non-interacting part}} \underbrace{- b\frac{J_1(\sqrt{2bt})}{\sqrt{bt}}e^{-\gamma t}e^{-i\omega_0 t}e^{ikz}e^{ik(\Delta z(t)-\Delta z(0))}\theta(t)}_{\text{phase modified scattered part}} \end{aligned} \tag{2.54}$$

The property of $\delta(t)e^{ik\Delta z(t)} = \delta(t)e^{ik\Delta z(0)}$ is used. The motion determines a **relative phase** ($e^{ik(\Delta z(t)-\Delta z(0))}$) between interacting part and non-interacting part [49, 52, 53, 71].

2.4.2 Single target in step-motion

Let's consider the following motion,

$$\Delta z(t) = \Delta z_0 \theta(t - t_0), \tag{2.55}$$

where Δz_0 is a constant value and indicates the distance of jump of the nuclear target and the $\theta(t - t_0)$ is the Heaviside function which takes the value of 1 for $t > t_0$ and 0 for other times.

Time intensity Substituting the step motion into Eq. (2.54) the new scattering field is written as,

$$(t < t_0) \rightarrow E_{\text{step}}(t) = \delta(t)e^{-i\omega t} - b\frac{J_1(\sqrt{2bt})}{\sqrt{bt}}e^{-\gamma t}e^{-i\omega_0 t}\theta(t). \tag{2.56}$$

$$(t > t_0) \rightarrow E_{\text{step}}(t) = \delta(t)e^{-i\omega t} - b\frac{J_1(\sqrt{2bt})}{\sqrt{bt}}e^{-\gamma t}e^{ik\Delta z_0}e^{-i\omega_0 t}\theta(t), \tag{2.57}$$

where the z variable is omitted after assuming the fixed position of the detector. The relative phase between the non-interacting field and the scattered field can suddenly change after t_0 as a result of motion.

The time intensity can be easily calculated to be,

$$I_{\text{step}}(t) = \delta(t) + |b\frac{J_1(\sqrt{2bt})}{\sqrt{bt}}|^2 e^{-2\gamma t}\theta(t) \tag{2.58}$$

[71]. Although the step motion affects the phase of the electric field, its time intensity is invariant since the product of the electric field cancels modified phases. The computed intensity proves that the time intensity of the applied step motion is equal to that of a motionless target in Fig. 2.3(b).

Spectrum The effect on the spectrum is transformed from Eq. (2.56) and Eq. (2.57). For simplicity, we assume the onset of step motion is right after the arrival of the synchrotron, $t_0 = 0$.

$$E_{\text{step}}(\omega) = \frac{1}{2\pi}\int_{-\infty}^{\infty} E_{\text{step}}(t)e^{i\omega t}d\omega = \underbrace{1}_{\text{non interacting}} + \underbrace{e^{ik\Delta z_0}(R(\omega) - 1)}_{\text{scattered part}} \tag{2.59}$$

The part of the scattering field that just passes the target doesn't experience any phase modification. And it is the scattered part which reveals phase modification. The spectrum is,

$$I_{\text{step}}(\omega) = \underbrace{1}_{\text{non interacting}} + \underbrace{e^{ikz_0}(R(\omega) - 1) + e^{-ikz_0}(R^*(\omega) - 1)}_{\text{interference}} + \underbrace{|(R(\omega) - 1|^2}_{\text{scattered part}} \tag{2.60}$$

An interesting effect of the phase modification is that the phase-modified spectrum can show various features in Fig. 2.3(b), which is called Fano-resonance [53, 79]. The $\Delta z_0 = \frac{\lambda}{2}$ is in particular interest because the extra phase is $e^{ik\Delta z_0} = -1$ and can enhance spectrum [53]. Besides, dynamical beating imprints double hump features around the tip of the peak.

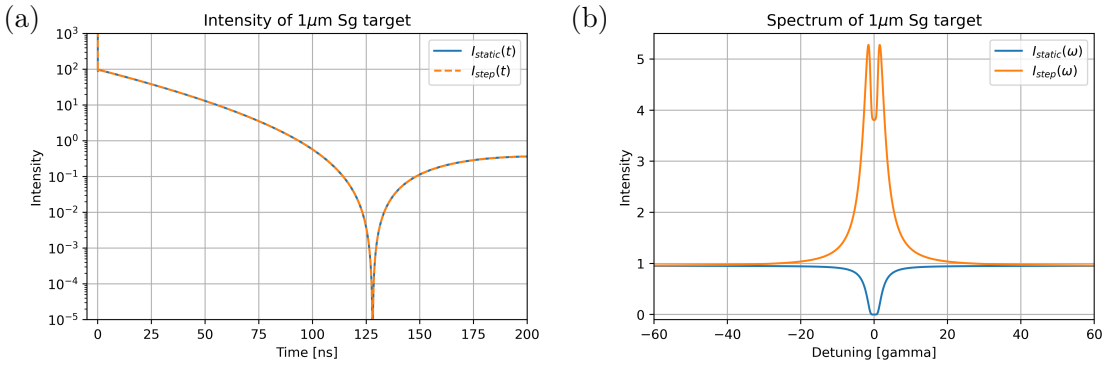

Figure 2.3: (a) The same intensity is found for the step-motioning target as the stationary target. (b) The enlarged distance makes the field propagate a longer distance, therefore a Fano line can be found in the spectrum. In this subfigure, a peak is visible while the static case exhibits an absorption dip.

Chapter 3

Shaping Mössbauer scattering waveform into short pulses

Implementation of a coherent nuclear pump probe measurement scheme has still been challenged, especially for the Mössbauer nuclear transitions which it requires two X-ray pulses with long delays (10 to several 10^2ns) [54]. Its difficulties can be found in a lack of sources with enough high-intensity and coherent radiation in this energy regime. One idea of shaping coherent Mössbauer scattering into pulse-shpaes in X-ray wavelength will be suggested as an effort to detour the experimental challenges in this X-ray field. Especially, the long lifetime of ^{57}Fe makes the generated pulses to be coherent for a long time.

With two targets' scattering equations, we will see how two Mössbauer targets scattering is different from the single target experiment and how the motionally induced phase can modify the scattering field. Based on the control of the scattering fields with the motion, one example motion will be introduced that can produce pulses with few nanoseconds duration at a desired time. We will discuss the properties and limitations of the generated pulse as a function of the targets' thickness. The next part of this chapter is about one application with iron with hyperfine interactions. A set of magnetic dipole moment alignments is introduced to suppress intensities at both sides of the generated pulses. And the achieve higher pulse contrast and property will be discussed based on the pulse's equation.

3.1 Nuclear forward scattering of two targets

By far we have treated the case that a single Mössbauer target scatters with a synchrotron pulse. When the $\delta(t)$-shape pump field is incident to the single target, it was simple to encounter the effect of motion. The total propagation distance, $(z_{\text{target}}(t_r) - z_{\text{target}}(t_a))$, is only function of current motion $z_{\text{target}}(t_r)$ because the synchrotron pulse interacts with target only once at t_a which is again constant.

However, a **continuous pumping field** requires a sophisticated consideration. The difference for the continuous pumping field is that it can interact with a target over a long period of time. The scattering field needs to include modified phases by its motions over the entire past to include the absorptions correctly and needs to consider the current motion for the radiation at present.

3.1.1 Scattering channels of two targets

When the two targets are installed for the NFS experiment, the total scattering can be seen as a sequence of two scatterings: the early scattering at target A and the second scattering at target B at a later time. The scattering of target A is the same as the single target NFS in that only the synchrotron pulse can pump the target. On the other hand, the scattering of target B has another pumping field in addition to the synchrotron pulse. The scattered field radiated by target A pumps the second target located downstream of the beamline.

Let us assume that both targets are at rest and homogeneous for a simple discussion. The synchrotron pulse interacts with the A target at an earlier time. The scattering field from the A target is,

$$\begin{aligned} E_A^{\mathrm{scatt}}(t) &= R_A(t) \otimes \delta^{\mathrm{i}}(t) e^{-i\omega_0 t} \\ &= (\delta(t) + T_A(t)) \otimes \delta^{\mathrm{i}}(t) e^{-i\omega_0 t}, \end{aligned} \tag{3.1}$$

where the $\delta^{\mathrm{i}}(t)e^{-i\omega t}$ indicates the incident synchrotron pulse. The superscript 'i' is introduced to distinguish with the $\delta(t)$ in the response function. The subscript 'A' labels the scattering targets.

Both of $E_A^{\mathrm{scatt}}(t)$ scatter off at the second target located in the backstream.

$$\begin{aligned} E_B^{\mathrm{scatt}}(t) &= R_B(t) \otimes E_A^{\mathrm{scatt}}(t) \\ &= R_B(t) \otimes \{(\delta(t) + T_A(t)) \otimes \delta^{i}(t) e^{-i\omega_0 t}\} \\ &= \delta^{\mathrm{i}}(t) e^{-i\omega_0 t} + T_A(t) + T_B(t) + T_{BA}(t), \end{aligned} \tag{3.2}$$

with the following notations.

- $T_A(t) = T_B(t) = -b\frac{J_1(\sqrt{2bt})}{\sqrt{bt}} e^{-\gamma t} e^{-i\omega_0 t}\theta(t)$ (if two targets are homogeneous)
- $T_{BA}(t) = T_B(t) \otimes (T_A(t) \otimes \delta^{i}(t) e^{-i\omega t})$

The Eq. (3.2) is composed of four terms explaining specific scattering channels. The corresponding schematic figure is presented in Fig. 3.1. The first channel is the scattering which doesn't engage in any scattering processes at both targets. The $T_A(t)$, and $T_B(t)$ are the scattered fields that have interacted only once with either of the targets. These scattered fields will be called **singly scattered field** over this thesis. The $T_{BA}(t)$ is the scattering field radiated from the B target as well. But this scattering shows different properties with $T_B(t)$ because it is the $T_A(t)$ that pumps the second target. The $T_{BA}(t)$ will be called **radiative coupling (scattering) field**.

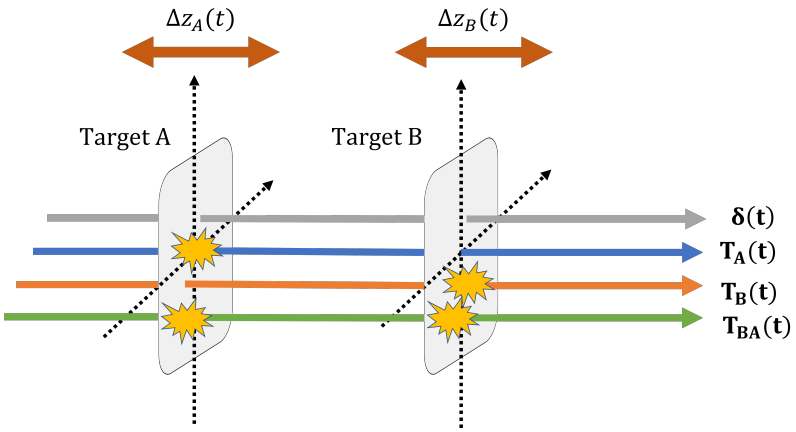

Figure 3.1: The figure schematically depicts possible scattering channels of the two Mössbauer targets scattering. The first channel is the non-interacting part which has interacted with none of the two targets, $\delta(t)$. The $T_A(t)$ and $T_B(t)$ indicate the singly scattered field from each of the two targets. The $T_A(t)$ doesn't interact with the second target and arrives at the detector. The $T_B(t)$ is defined similarly. The last $T_{BA}(t)$ is the scattering path that experiences two interactions at both targets during its propagation. The targets are able to move independently.

3.1.2 Scattering of targets at rest

The Eq. (3.2) is explicitly written as,

$$\begin{aligned} E_{\text{rest}}(t>0) = \quad & \delta(t)e^{ikz}e^{-i\omega_0 t} - 2b\frac{J_1(\sqrt{2bt})}{\sqrt{bt}}e^{-\gamma t}e^{ikz}e^{-i\omega_0 t} \\ & + \Big(\int_0^t b^2 \frac{J_1(\sqrt{2b(t-\tau)})}{\sqrt{b(t-\tau)}}\frac{J_1(\sqrt{2b\tau})}{\sqrt{b\tau}}d\tau\Big)e^{-\gamma t}e^{ikz}e^{-i\omega_0 t}, \end{aligned} \tag{3.3}$$

where the non-interacting channel, doubled singly scattered field due to homogeneous targets assumption, and the radiative coupling scattering field can be found in order. The integral range is given as 0 to t after evaluating $\theta(\tau)$ and $\theta(t-\tau)$ in the $T_A(\tau)$ and $T_B(t-\tau)$. The superscript 'scatt' in $E_{\text{rest}}(t)$ and 'i' in $\delta(t)e^{ikz}e^{-i\omega t}$ are dropped without losing the meaning. The field considers the arriving electric field at the detector during $t>0$, thereby the $\theta(t)$ is omitted from the equation.

The time intensity is calculated as,

$$
\begin{aligned}
I_{\text{rest}}(t>0) = \quad & \delta(t) + \underbrace{|2b\frac{J_1(\sqrt{2bt})}{\sqrt{bt}}e^{-\gamma t}|^2}_{=|T_A(t)+T_B(t)|^2} \\
& + \underbrace{|\Big(\int_0^t b^2 \frac{J_1(\sqrt{2b(t-\tau)})}{\sqrt{b(t-\tau)}}\frac{J_1(\sqrt{2b\tau})}{\sqrt{b\tau}}d\tau\Big)e^{-\gamma t}|^2}_{=|T_{BA}(t)|^2} \\
& - 4b^3\frac{J_1(\sqrt{2bt})}{\sqrt{bt}}e^{-2\gamma t}\Big(\int_0^t \frac{J_1(\sqrt{2b(t-\tau)})}{\sqrt{b(t-\tau)}}\frac{J_1(\sqrt{2b\tau})}{\sqrt{b\tau}}d\tau\Big)
\end{aligned}
\tag{3.4}
$$

The time intensities of identical two targets are plotted in the Fig. 3.2(a)-(d) in an orange solid line with various thicknesses. The thicknesses with $d = 0.1\mu m$, $d = 0.33\mu m$, $d = 0.66\mu m$, $d = 1\mu m$ are chosen for the figures. All four subplots have a common feature that the high intensity of synchrotron pulse locates at $t = 0$ and the intensity of the pure scattering field follows after $t > 0$. Expectedly, the stronger Dynamical beating and radiative coupling field can be found in the time intensity of the thicker targets Eq. (2.48) [80].

The timely varying amplitude of the singly scattered field, $T_A(t)+T_B(t) = 2T_A(t)$ (for two homogeneous targets), and radiative coupling scattering field, $T_{BA}(t)$ gives a complicated behavior for the time intensity $I_{\text{rest}}(t)$. Not all four scattering channels equally make up the time intensity at given times. Rather it is the singly scattered field that comprises most of the time intensity at early measurement time. However, the amplitude of $T_{BA}(t)$ increases and becomes comparable and even higher than the singly scattered fields over the early measurement time. Because its importance at future discussion, $|T_{BA}(t)|^2$(green) and $|2T_A(t)|^2$(blue) are numerically calculated to see its magnitude, independent to $I_{\text{rest}}(t > 0)$. Notice that $I_{\text{rest}}(t) = |T_A(t) + T_B(t) + T_{BA}(t)|^2 = |2T_A(t) + T_{BA}(t)|^2$, since the oscillating terms $|T_{BA}(t)|^2$ can be greated than $I_{\text{rest}}(t)$. Manually produced each scattering intensities are computed by the PYNUSS [81]. The details of the calculation are outlined in Appendix A.3.

3.1.3 Moving two homogeneous targets

When moving targets are in consideration, it is necessary to describe each scattering event Eq. (3.1) and Eq. (3.2) in each target's rest frame. The scattering of the target A is already obtained in Section 2.4.1. The required work is to transform the Eq. (2.54) into the B target rest frame and to describe the scattering in its rest frame. Later, the total scattering field will be transformed back to the lab frame.

The obtained equation is capable to describe the scattering fields of two moving targets if the motions are non-relativistic. The details of the calculation can be

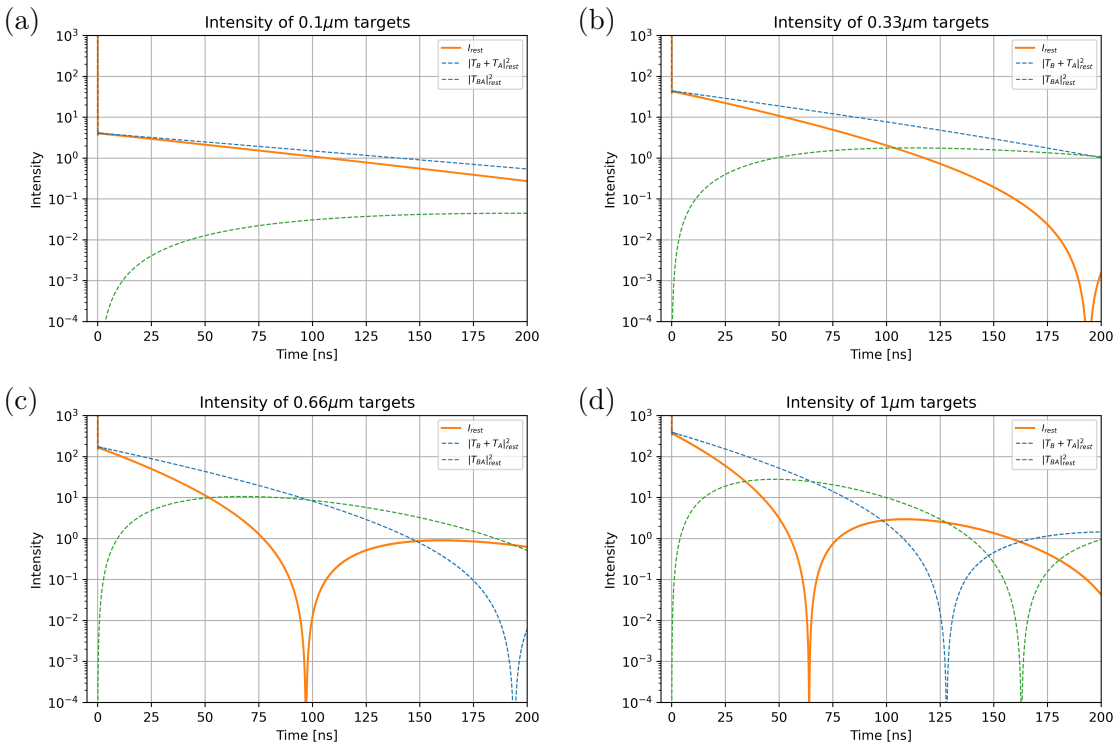

Figure 3.2: (*)The motions of resting two homogenous targets are excluded in this figure panel. (a)-(d) The time intensities of two resting targets are plotted with various thickness parameters. The manually produced intensity of singly scattered fields and the intensity of the radiative coupling field are presented together for future purposes. Notice that $I_{\text{rest}}(t>0)$(orange)$\neq \delta(t)+|T_A(t)+T_B(t)|^2$(blue)$+|T_{BA}(t)|^2$(green)

found in Appendix A.2.

$$\begin{aligned} E_{\text{motion}}(t>0) = \quad & \delta(t)e^{ikz}e^{-i\omega_0 t} \\ & + T_A(t)e^{ik(z+\Delta z_A(t))}e^{-ik\Delta z_A(0)} \\ & + T_B(t)e^{ik(z+\Delta z_B(t))}e^{-ik\Delta z_B(0)} \\ & + (T_B(t)\otimes T_A(t)e^{-ik(\Delta z_{BA}(t)-\Delta z_{BA}(0))})e^{ik(z+\Delta z_B(t))}e^{-ik\Delta z_B(0)}, \end{aligned} \tag{3.5}$$

where the $\delta(t)e^{ikz}e^{-i\omega_0 t}$ refers to the non-interacting synchrotron pulse, $T_A(t)$ and $T_B(t)$ are the singly scattered fields, the radiative coupling field can be found in order. The $\Delta z_A(t)$, $\Delta z_B(t)$ are the motions of each target that modifies the phases of each term. Expectedly, the radiative coupling field includes a relative distance $\Delta z_{BA}(t) = \Delta z_B(t) - \Delta z_A(t)$. The convolution $T_B(t)\otimes(T_A(t)e^{-ik(\Delta z_{BA}(t)-\Delta z_{BA}(0))})$ explains the radiation at the current time requires to consider scatterings that have taken over its entire past.

Step motion

The first example of motion is step motion. It supposes that the motion will only

take place at the B target installed at the backstream for this example.

The motions are formulated as,

$$\begin{cases} \Delta z_A(t) = 0 \\ \Delta z_B(t) = \Delta z_0 \theta(t - t_0) \end{cases} \tag{3.6}$$

The Fig. 3.3(a),(b) show examples of motions of A and B targets with variables $\Delta z_0 = \lambda/2 = 4.3 \times 10^{-11}$m, $t_0 = 10$ or 20ns, respectively.

Substituting, the motion parameters into the Eq. (3.5), the scattering field in the lab frame is given as.

$$\begin{aligned} E_{\text{step}}(t > 0) = \quad & \delta(t) e^{-i\omega_0 t} - b \frac{J_1(\sqrt{2bt})}{\sqrt{bt}} e^{-\gamma t} e^{-i\omega_0 t} \underbrace{(1 + e^{ik\Delta z_0 \theta(t-t_0)})}_{\text{interference b/w } T_A \text{ \& } T_B} \\ & + \Big(\int_0^t b^2 \frac{J_1(\sqrt{2b(t-\tau)})}{\sqrt{b(t-\tau}} \frac{J_1(\sqrt{2b\tau})}{\sqrt{b\tau}} e^{-ik\Delta z_0 \theta(\tau - t_0)} d\tau \Big) \\ & \times e^{-\gamma t} e^{ik\Delta z_0 \theta(t-t_0)} e^{-i\omega_0 t}, \end{aligned} \tag{3.7}$$

where a constant overall phase, e^{ikz}, is omitted by assuming the scattering field is measured at a fixed position. A noticeable feature for the scattering of two homogeneous targets is the **interference between two singly scattered fields**. The $\Delta z_0 = \lambda/2$ is of particular interest since the two singly scattered fields destructively interfere together. Before and after the t_0, the relative phase of singly scattered fields is reversed and no singly scattered field is observed.

- when $t < t_0$: $b\frac{J_1(\sqrt{2bt})}{\sqrt{bt}}(1 + 1) = 2b\frac{J_1(\sqrt{2bt})}{\sqrt{bt}}$
- when $t > t_0$: $b\frac{J_1(\sqrt{2bt})}{\sqrt{bt}}(1 + e^{i\pi}) = 0$

The time intensity for the step-motioning targets is,

$$\begin{aligned} I_{\text{step}}(t > 0) = \delta(t) + & \underbrace{|b\frac{J_1(\sqrt{2bt})}{\sqrt{bt}} e^{-\gamma t}|^2 |1 + e^{ik\Delta z_0 \theta(t-t_0)}|^2}_{=|T_A(t)+T_B(t)|^2_{\text{step}}} \\ & + \underbrace{|\int_0^t b^2 \frac{J_1(\sqrt{2b(t-\tau)})}{\sqrt{b(t-\tau)}} \frac{J_1(\sqrt{2b\tau})}{\sqrt{b\tau}} e^{-ik\Delta z_0 \theta(\tau - t_0)} d\tau \times e^{-\gamma t}|^2}_{=|T_{BA}(t)|^2_{\text{step}}} \\ & - 2b^3 \frac{J_1(\sqrt{2bt})}{\sqrt{bt}} \Big(\int_0^t \frac{J_1(\sqrt{2b(t-\tau)})}{\sqrt{b(t-\tau)}} \frac{J_1(\sqrt{2b\tau})}{\sqrt{b\tau}} e^{-ik\Delta z_0 \theta(\tau - t_0)} \Big) e^{-2\gamma t} \\ & \times (2 + e^{-ik\Delta z_0 \theta(t-t_0)} + e^{ik\Delta z_0 \theta(t-t_0)}) \end{aligned} \tag{3.8}$$

The motion, Fig. 3.3(a), is applied to targets with 0.1μm and 0.66μm thickness for the modified intensity Fig. 3.3(c)(e). While it is the intensity of 0.33μm and 1μm that represented in Fig. 3.3(d)(f) with the motion, Fig. 3.3(b). The Fig. 3.3(c)-(f) describes the effect of motion on the time intensity. The orange solid line plots $I_{\text{step}}(t > 0)$ in all four figures (c)-(f). The independently calculated singly scattered fields part (in broken blue) and radiative coupling field part (in broken green) are presented together to explain the effect of the motion to $I_{\text{step}}(t > 0)$. The computed results support the interference effect at the time intensities. The I_{step} is the same as the time intensity of $I_{\text{rest}}(t > 0)$ (grey), in Eq. (3.4)(c)-(f), before the motion at 10ns and 20ns. After the displacement. it is governed by the radiative coupling field $|T_{BA}(t)|^2_{\text{step}}$ (green) because of motionally induced destructive interference featured as $|T_A(t) + T_B(t)|^2_{\text{step}}$ (blue)=0.

Although it is difficult to solve the radiative coupling scattering field thoroughly, its upper boundary is obtainable as followed. The detailed discussion is presented at the Appendix A.4

$$|T_{BA}(t)|^2_{\text{step}} \leq |T_{BA}(t)|^2_{\text{rest}}, \tag{3.9}$$

where the intensity of the radiative coupling scattering field of the step motioning targets cannot exceed that of the static case. The agreeing numerical result can be found by comparing each subplots of Fig. 3.3 and Fig. 3.2. Lastly, the decreasing radiative coupling scattering field after the motion can be also understood with the sign flips in the integrand of $T_{BA}(t)|_{\text{step}}$ in Eq. (3.8). The $|T_{BA}(t)|^2_{\text{step}}$ starts increasing again since when decreasing integration crosses zero.

Ramp(uniform) motion

The next set of motions in consideration is,

$$\begin{cases} \Delta z_A(t) = 0 \\ \Delta z_B(t) = vt \times \theta(t), \end{cases} \tag{3.10}$$

where the v is a constant velocity for the B target. The motion of the B target starts immediately after the arrival of the synchrotron pulse while the A target doesn't move. The figure of applied motion is provided in Fig. 3.4(a) with $v = 0.05[\frac{\lambda}{\text{ns}}]$ =4.3mm/s.

Substituting the motion variables into Eq. (3.5),

$$\begin{aligned} E_{\text{ramp}}(t > 0) = \quad & \delta(t)e^{-i\omega_0 t} - b\frac{J_1(\sqrt{2bt})}{\sqrt{bt}}e^{-\gamma t}e^{-i\omega_0 t} - b\frac{J_1(\sqrt{2bt})}{\sqrt{bt}}e^{-\gamma t}\underbrace{e^{-i(\omega_0 - kv)t}}_{\text{Doppler Shift}} \\ & + \Big(\int_0^t b^2 \frac{J_1(\sqrt{2b(t-\tau)})}{\sqrt{b(t-\tau}}\frac{J_1(\sqrt{2b\tau})}{\sqrt{b\tau}}e^{-ikv\tau}d\tau\Big)e^{-\gamma t}\underbrace{e^{-i(\omega_0 - kv)t}}_{\text{Doppler Shift}} \end{aligned} \tag{3.11}$$

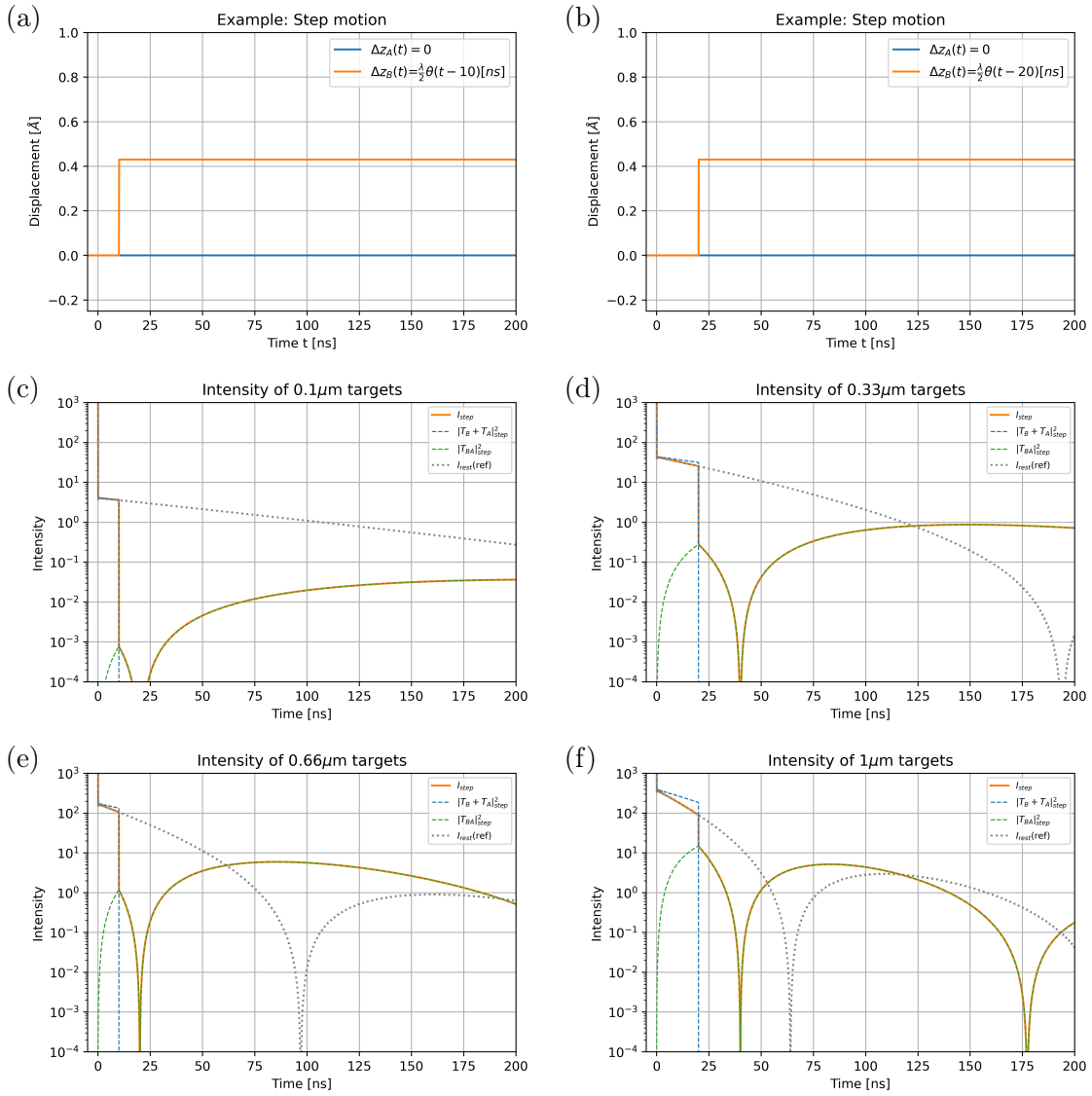

Figure 3.3: (a),(b) The motions of two targets with different step motion parameters. (c),(e) The time intensities of 0.1μm, 0.66μm targets with '(a)' motion. The effect of motion cancels two singly scattered fields (blue) and only remained radiative coupling scattering field (green) explains the scattering field (blue). (d),(f) The time intensities of the 0.33μm, 1μm targets with '(b)' motion.

While the two earlier examples have the same frequency for all scattered fields, the scattered field of the uniformly moving target radiates in a shifted frequency due to **the Doppler shift**, as marked with underbrace in Eq. (3.11). Notice that the same Doppler-shifted scattering field can be found in the radiative coupling scattering field as a function motion of the B target($\Delta z_B(t)$) because the radiative coupling scattering is also radiated from the B target.

The scattering of moving targets with a constant velocity is available to be expressed in terms of the frequency response function of static targets, analytically.

First, the non-interacting part transforms as,

$$\int_{-\infty}^{\infty} \delta(t) e^{-i\omega_0 t} e^{-i\omega t} dt = 1$$

We understand Fourier transform of the singly scattered field of the static A target is,

$$-\int_{-\infty}^{\infty} b \frac{J_1(\sqrt{2bt})}{\sqrt{bt}} e^{-\gamma t} e^{-i\omega_0 t} e^{-i\omega t} \theta(t) dt = T_A(\omega) = R_A(\omega) - 1,$$

with $R(\omega) = e^{\frac{-ib}{\hbar(\omega-\omega_0)+i\gamma}}$

The B target's Doppler shifted singly scattered is calculated as,

$$-\int_{-\infty}^{\infty} b \frac{J_1(\sqrt{2bt})}{\sqrt{bt}} e^{-\gamma t} e^{-i(\omega_0 - kv)t} e^{-i\omega t} \theta(t) dt = T_B(\omega - kv) = R_B(\omega - kv) - 1$$

The part of radiative coupling scattering can be re-expressed to,

$$\begin{aligned}
\{T_B(t) \otimes (T_A(t) e^{-ikvt})\} e^{ikvt} &= \int T_B(t-\tau) T_A(\tau) e^{-ikv\tau} e^{ikvt} d\tau \\
&= \int T_B(t-\tau) e^{ikv(t-\tau)} T_A(\tau) d\tau \\
&= (T_B(t) e^{ikvt}) \otimes T_A(t)
\end{aligned}$$

The Fourier transformation transforms the convolution operation into a simple multiplication operation.

$$\int_{-\infty}^{\infty} (T_B(t) e^{ikvt}) \otimes T_A(t) e^{-i\omega t} dt = (R_B(\omega - kv) - 1)(R_A(\omega) - 1),$$

where $T_B(t)e^{ikvt}$ is the Doppler shifted singly scattered field of B target.

The total scattered field can be represented as

$$\begin{aligned}
E_{\text{ramp}}(\omega) &= R_B(\omega - kv) R_A(\omega) E_0(\omega) \\
&= \big(1 + (R_A(\omega) - 1) + (R_B(\omega - kv) - 1) \\
&\qquad + (R_B(\omega - kv) - 1)(R_A(\omega) - 1)\big),
\end{aligned} \tag{3.12}$$

where $E_0(\omega)$ is 1 if a synchrotron pulse is incident to the targets.

Each response function has a value of about 1 for most of the frequencies, except regions near transition frequency ω_0 or $\omega_0 - kv$ with the same $\gamma = 4.66$neV width. Recalling that 0.194mm/s corresponds to the one linewidth, the radiative coupling scattering channel is able to be set **off-resonant scattering condition** by even slow velocity. If we assume the applied velocity is enough fast to create a off-resonant scattering condition, we can see that radiative coupling scattering field can be neglected with the following argument.

First, we discuss ω near ω_0 and introduce $\Delta = \omega - \omega_0$.

$$\begin{aligned}(R_B(\omega - kv) - 1)(R_A(\omega) - 1) &= (1 + \frac{-ib}{\hbar(\Delta - kv) + i\gamma} + \cdots - 1)(e^{\frac{-ib}{\hbar\Delta + i\gamma}} - 1) \\ &\simeq (\frac{-b\gamma}{(\hbar kv)^2 + \gamma^2} + \frac{-i\hbar bkv}{(\hbar kv)^2 + \gamma^2}) \times (e^{\frac{-ib}{\hbar\Delta + i\gamma}} - 1) \\ &\simeq \underbrace{(\frac{-b\gamma}{(\hbar kv)^2} + \frac{-ib}{\hbar kv})}_{\simeq 0} \times (e^{\frac{-ib}{\hbar\Delta + i\gamma}} - 1) \simeq 0,\end{aligned}$$

where $\Delta \ll kv$ is assumed for first approximation. Neither $\frac{b}{\hbar kv}$ nor $\frac{\gamma}{\hbar kv}$ has a comparable value at the second approximation. Similar discussions are valid for ω near $\omega_0 - kv$ and other frequencies. Therefore, the vanishing radiative coupling scattering field can be held.

The spectrum is

$$\begin{aligned}I_{\text{ramp}}(\omega) &\simeq 1 + |R_A(\omega) - 1|^2 + |R_B(\omega - kv) - 1|^2 \\ &\quad + 2\text{Re}(R_A(\omega) - 1) + 2\text{Re}(R_B(\omega - kv) - 1) \\ &= |R_B(\omega - kv)|^2 + |R_A(\omega)|^2 - 1, \end{aligned} \tag{3.13}$$

where the productions of two different response functions are assumed zero for the same reason.

The spectrum $I_{\text{ramp}}(\omega)$ (blue dot) of uniformly moving B target with $v_B = 0.05[\frac{\lambda}{\text{ns}}]$ and static A target is plotted in Fig. 3.4(b). The $I_{\text{ramp}}(\omega)$ features two absorption curves at $\omega = 0[\gamma]$ and near $\omega = -44.3[\gamma]$. The spectrum of scattered part of $1 - |R_B(\omega - kv)|^2$(red) is calculated independently to demonstrate moving target B is responsible for the shifted absorption curve. Notice that $|R_B(\omega - kv) - 1|^2$ doesn't contain the interference term. Expectedly, the manually produced transition centers at the same $\omega = -kv = -44.3[\gamma]$. While the scattered field of static A target's spectrum is represented as $1 - |R_A(\omega)|^2$(orange) at the $\omega = 0$. It also well displays the created off-resonant scattering conditions between two transitions. The spectrum of produced $|(R_B(\omega - kv) - 1)(R_A(\omega) - 1)|^2$ (green) confirms that the scattering field has extremely low contributions from the radiative coupling scattering channel.

Equivalently, the radiative coupling scattering field can be considered negligible for the scattering field in time if we transform each term of Eq. (3.12).

$$E_{\text{ramp}}(t>0) \simeq \delta(t)e^{-i\omega_0 t} - b\frac{J_1(\sqrt{2bt})}{\sqrt{bt}}e^{-\gamma t}e^{-i\omega_0 t}(1+e^{ikvt}), \tag{3.14}$$

The time intensity is obtained as,

$$I_{\text{ramp}}(t>0) \simeq \delta(t) + \underbrace{|b\frac{2J_1(\sqrt{2bt})}{\sqrt{bt}}e^{-\gamma t}|^2}_{|T_A(t)+T_B(t)|^2_{\text{ramp}}} \overbrace{\cos^2(kvt/2)}^{\text{induced beating}} \tag{3.15}$$

The main information of the Fig. 3.4(c)-(f) is in the I_{ramp}(orange). The I_{ramp}(orange) is calculated without assuming the vanishing raidiative coupling field with Eq. (3.11). Each figure confirms the validity of approximation in Eq. (3.15). The I_{ramp}(orange) are well explained by the singly scattered fields, $|T_A(t)+T_B(t)|^2_{\text{ramp}}$ (blue). The reasons can be found in the created weak raditive coupling field represented as green lines ($|T_{BA}|^2_{\text{ramp}}$) in all figures. The motions also make the arriving time intensity to beat. The targets in Fig. 3.4(c)(e) show the 2.5 cycles($=5\pi$) of beatings for every 50ns. That is consistent with applied motion variables $\Delta\phi = kv\Delta t = \frac{2\pi}{\lambda}\times 0.05[\frac{\lambda}{\text{ns}}]\times 50[\text{ns}]= 5\pi$. The same information can be found in Fig. 3.4(d)(f), but the $v = 0.025[\frac{\lambda}{\text{ns}}]$ is applied. As a result, half speed of induced beating is observed for these two examples. The two other lines are related to the existing radiative coupling field that is assumed vanishing for this subsection. Despite its low intensity, it has value and it will be discussed in the next subsection after finding an approximation.

3.1.4 Radiative coupling scattering in off-resonant condition

In this subsection, we will find the proper approximation for the radiative coupling scattering field in off-resonant conditions.

Let's consider the following two samples having different transition frequencies at $\omega = \omega_0 - kv$ and ω_0 respectively. The two different transition frequencies are achieved with the Doppler shift at uniform motion example. Rewritting the scattering field in frequency,

$$\begin{aligned} E(\omega) &= R_B(\omega-kv)R_A(\omega)E_0(\omega) \\ &= 1 + (e^{\frac{-ib}{\hbar(\omega-\omega_0)+i\gamma}}-1) + (e^{\frac{-ib}{\hbar(\omega-\omega_0+kv)+i\gamma}}-1) + (e^{\frac{-ib}{\hbar(\omega-\omega_0+kv)+i\gamma}}-1)(e^{\frac{-ib}{\hbar(\omega-\omega_0)+i\gamma}}-1) \qquad (3.16) \\ &\overset{!}{=} 1 + (e^{\frac{-ib}{\hbar(\omega-\omega_0)+i\gamma}}-1)(1+\kappa_0) + (e^{\frac{-ib}{\hbar(\omega-\omega_0+kv)+i\gamma}}-1)(1+\kappa_1), \qquad (3.17) \end{aligned}$$

where $E_0(\omega)$ is the incident field which is considered as 1 for the synchrotron pulse.

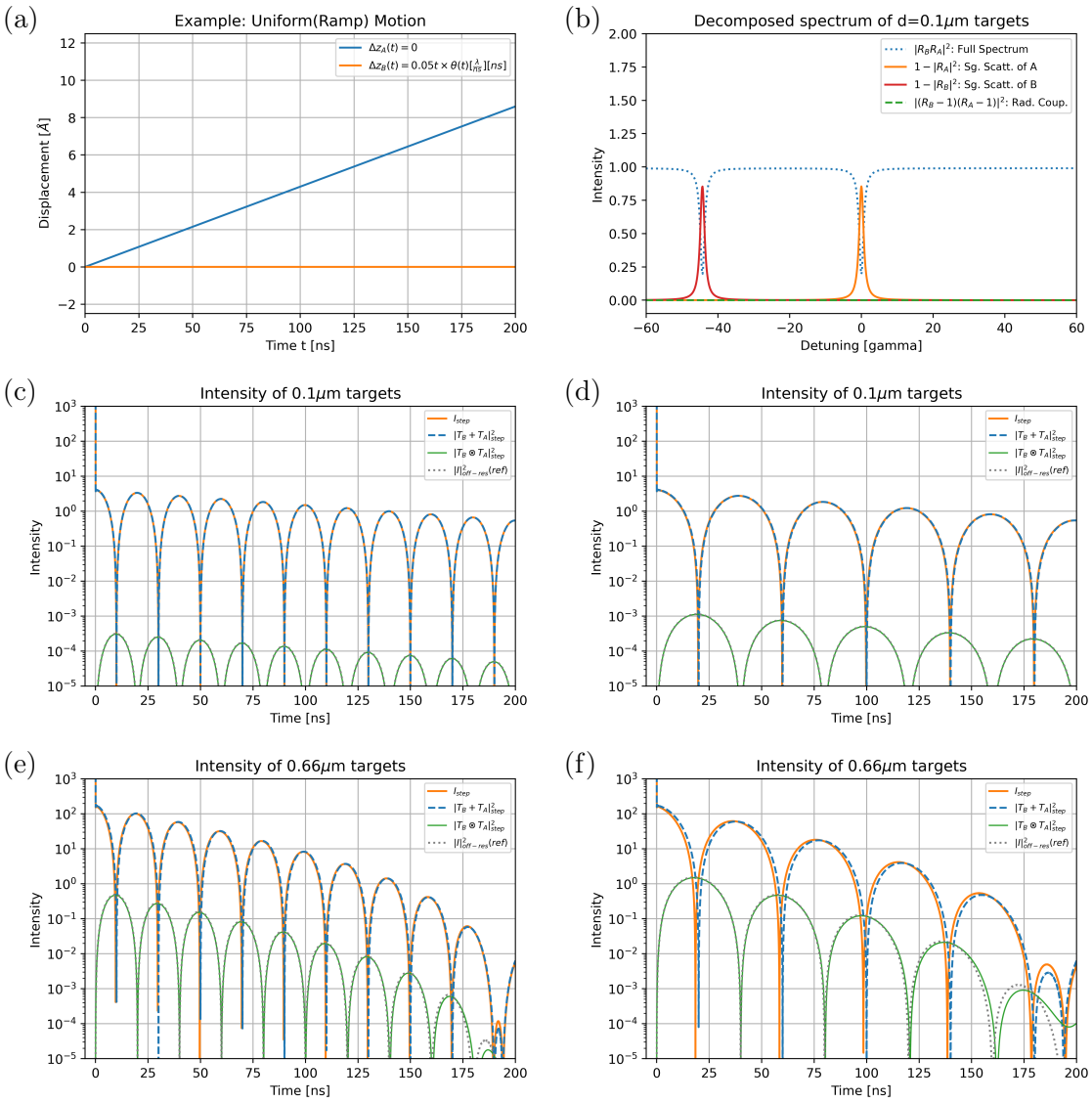

Figure 3.4: (a) The exemplary motions of two targets with uniform motion parameters with $\Delta z_A = 0$ $\Delta z_B = 0.05t[\frac{\lambda}{\text{ns}}][\text{ns}]$. (b) The spectrum of the 0.1μm thick targets in the (a) motion. Auxillary two spectra $1-|R_B(\omega-kv)|^2$ and $1-|R_A(\omega)|^2$ are presented together to demonstrate the Doppler shift. It also verifies the vanishing radiative coupling scattering field (green). (c)(e) The time intensity Eq. (3.11) is plotted in orange for 0.1μm, 0.66μm thick targets in (a) motion. Because of the weak radiative coupling field (green), most of the I_{ramp} is explained with the $|T_A+T_B|^2_{\text{ramp}}$ (blue), as seen in Eq. (3.15). (d)(f) The same targets' time intensities are calculated with $\Delta z_A = 0[\lambda]$ $\Delta z_B = 0.025t[\frac{\lambda}{\text{ns}}][\text{ns}]$ motion to see the different beating. One approximation of radiative coupling field ($I_{\text{off-res}}$ in Eq. (3.20)) explains the thickness and detuning dependency of the off-resonant radiative coupling field.

The κ_0 and κ_1 are introduced to describe the radiative coupling field in off-resonant condition. We want to solve κ_0 and κ_1 that make Eq. (3.17) satisfy Eq. (3.16). Starting from the simplest case, the simplest candidates for the κ_0 and κ_1 are the constant values. So that we can approximate the total scattering by giving constant modification to each transition. The physical meaning of the constant κ_0 and κ_1 is weak coupling between two transitions. One possible approach is to use the asymptotical method. The approximation must hold for every ω, we can find κ_0 and κ_1 with the values of $E(\omega)$ in $\omega \to \omega_0$ and $\omega \to \omega_0 - kv$ limits.

In case of $\omega \to \omega_0$ and $\omega_0 - kv$, the Eq. (3.16) is evaluated as,

$$\begin{aligned} E(\omega \to \omega_0) &= 1 + (e^{-\frac{b}{\gamma}} - 1) + (e^{\frac{-ib}{\hbar kv + i\gamma}} - 1) + (e^{\frac{-ib}{\hbar kv + i\gamma}} - 1)(e^{-\frac{b}{\gamma}} - 1) \\ &= e^{-\frac{ib}{\hbar kv + i\gamma}} e^{-\frac{b}{\gamma}} \\ E(\omega \to \omega_0 - kv) &= e^{\frac{ib}{\hbar kv + i\gamma}} e^{-\frac{b}{\gamma}} \end{aligned}$$

While the Eq. (3.17) is give as,

$$\begin{aligned} E(\omega \to \omega_0) &= 1 + (e^{-\frac{b}{\gamma}} - 1)(1 + \kappa_0) + (e^{-\frac{ib}{\hbar kv + i\gamma}} - 1)(1 + \kappa_1) \\ E(\omega \to \omega_0 - kv) &= 1 + (e^{-\frac{b}{\gamma}} - 1)(1 + \kappa_1) + (e^{\frac{ib}{\hbar kv + i\gamma}} - 1)(1 + \kappa_0) \end{aligned}$$

Solving two coupled equations with matrix,

$$\begin{pmatrix} e^{-\frac{ib}{\hbar kv + i\gamma}} e^{-\frac{b}{\gamma}} - 1 \\ e^{\frac{ib}{\hbar kv + i\gamma}} e^{-\frac{b}{\gamma}} - 1 \end{pmatrix} = \begin{pmatrix} e^{-\frac{b}{\gamma}} - 1 & e^{-\frac{ib}{\hbar kv + i\gamma}} - 1 \\ e^{\frac{ib}{\hbar kv + i\gamma}} - 1 & e^{-\frac{b}{\gamma}} - 1 \end{pmatrix} \begin{pmatrix} 1 + \kappa_0 \\ 1 + \kappa_1 \end{pmatrix}$$

Using off-resonant condition $e^{\pm\frac{ib}{\hbar kv + i\gamma}} \simeq 1 \pm \frac{ib}{\hbar kv} + \cdots$ and considering terms by $O(\frac{b}{\hbar kv})$,

$$\begin{cases} \kappa_0 \simeq -i\frac{b}{2\hbar kv} \\ \kappa_1 \simeq i\frac{b}{2\hbar kv}, \end{cases} \tag{3.18}$$

where the κ_0 and $\kappa_1 = \pm(9.18 \times 10^{-3})i$ with $\hbar kv = -44.3\gamma$, respectively. And the $b = \Gamma_c d$ with Γ_c is the enhanced decay width defined as $\frac{\lambda}{2\pi} f_{LM} \frac{1}{1+\alpha} \frac{1}{2j_0+1} \Gamma$, introduced in Eq. (2.47).

The time intensity of the radiative coupling field with the off-resonant conditions is then calculated as,

$$E_{\text{off-res}}(t) = -i\frac{b}{2\hbar kv} \times b\frac{J_1(\sqrt{2bt})}{\sqrt{bt}} e^{-\gamma t}(e^{-i\omega_0 t} - e^{-i(\omega_0 + kv)t})\theta(t), \tag{3.19}$$

$$I_{\text{off-res}}(t) = |\frac{b}{2\hbar kv}|^2 |2b\frac{J_1(\sqrt{2bt})}{\sqrt{bt}}|^2 e^{-2\gamma t} \sin^2(\frac{kv}{2}t), \tag{3.20}$$

which states the intensity of the radiative coupling field is dependent on the detuning and the thickness.

The direct calculation of radiative coupling field is difficult from the Eq. (3.11) specifically for the off-resonant condition. Instead, the Eq. (3.20) can approximate the radiative coupling field in static off-resonant condition. The numerical results are presented in the Fig. 3.4(c)-(f) as green and grey lines. Green lines indicate the intensity of off-resonant radiative coupling field in Eq. (3.11). And the grey lines are the apporximated equations, Eq. (3.20). All results are calculated with PYNUSS [81]. Overall, the approximation explains well the $|T_{BA}|^2_{\mathrm{ramp}}$(green), except some deviations near zero of Dynamical beating. Expectedly, the detuning depedent radiative coupling field can be observed between (c)(d) and (e)(f). The thickness also affect to the intensity of the off-resonant radiative coupling field (c)(e) as the relative intensity between I_{ramp}(orange) and $|T_{BA}|^2_{\mathrm{ramp}}$(green). The thickness dependency can be caomparable only as relative intensity between I_{ramp}(orange) and $|T_{BA}|^2_{\mathrm{ramp}}$(green) because of different Dynamical beating amplitude for different thickness. Furthermore, it also explains the same speed of induced beating patterns as well as the advanced phases by $\pi/2$ compare to Eq. (3.15).

3.2 Recipe for shaping waveform into short pulses

A couple of simple motions of two targets and their effect on the time intensity have been investigated. Then, **one might ask what can we achieve with such motionally induced phase modifications?**. A recipe for shaping scattering waveform into short pulses will be proposed based on the same principles we have seen. The two targets are controlled in a way that the **destructive interference** condition is kept for the most of measurement times. Such interference conditions will be relaxed in purpose to produce a pulse. An **induced beating** from the Doppler-shifted scattering field enables to produce a pulse in a desired time. Specifically, the long lifetime of nuclear excitation allows the pulses to be **coherent** for a long time 141ns, for ^{57}Fe nuclei.

3.2.1 Assumptions

Over this chapter, few assumptions will be made on the target for the sake of simple discussion.

- Thin-enough homogenous targets
- Vanishing hyperfine interaction
- Fast and precise piezotransducer control

The suggested scheme is sensitive to the amplitude of the radiative coupling field. We will see the scheme succeeds to produce a good pulse only when the radiative coupling field satisfies a condition in Section 3.2.4. A thicker target exhibits rapidly

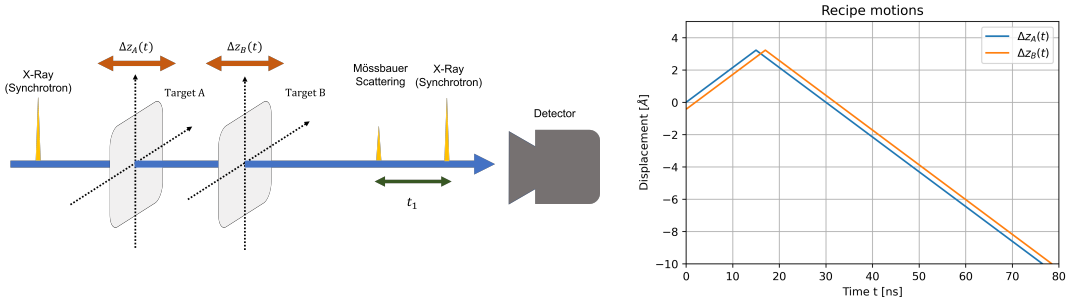

(a) Setting for the waveform modification

(b) Recipe motions for waveform shaping

Figure 3.5: (a) This figure captures a Mössbauer scattering shaping scheme into pulses. The pulses include a synchrotron pulse and produced pulses from the scattering. Well-designed motions of two targets can shape the scattering field into pulses of nanosecond duration. The produced pulse can arrive at the detector at a chosen time. Lastly, it is the coherent property of the synchrotron and nuclear resonant scattering that promise a well-defined phase for two arriving pulses. (b) Example motions of shaping scattering waveform into pulse-shape that locates 15ns later of synchrotron pulse.

increasing radiative coupling field [80], which imposes a more strict condition for the pulse generation. A thin-enough targets assumption is encouraged to consider this restriction at a minimum extend during the discussion. The section will start without considering the restriction at the beginning, however, we will return to this assumption. Moreover, the vanishing hyperfine interaction is assumed to keep the discussion for the sake of simplicity. The fast piezotransducer is assumed to get a timely narrow pulse. The speed isn't necessarily comparable to chosen velocity over this section. However, speed becomes an important parameter for a successful generation if targets are showing strict time conditions, dynamical beating, and, most of all, quantum beating.

3.2.2 Recipe motions

Let's consider the following set of motions of two Mössbauer targets.

$$\begin{cases} \Delta z_A(t) = & vt \times (\theta(t) - \theta(t - t_1)) \\ & -v(t - 2t_1) \times \theta(t - t_1) \\ \Delta z_B(t) = & vt \times (\theta(t) - \theta(t - t_1 - \tau)) \\ & -v(t - 2t_1 - 2\tau) \times \theta(t - t_1 - \tau) - \frac{\lambda}{2}\theta(t) \end{cases} \tag{3.21}$$

To describe the scattering in the target rest frame, it is desirable to separate the time into three intervals according to the relative motions of two targets.

- $0 < t < t_1 : \Delta z_A(t) = vt \ \& \ \Delta z_B(t) = vt - \frac{\lambda}{2}$
- $t_1 < t < t_1 + \tau : \Delta z_A(t) = -v(t - 2t_1) \ \& \ \Delta z_B(t) = vt - \frac{\lambda}{2}$

- $t_1 + \tau < t < \infty$: $\Delta z_A(t) = -v(t - 2t_1)$ & $\Delta z_B(t) = -v(t - 2t_1) + \frac{\lambda}{2}$

The Fig. 3.5(b) describes the recipe motion of A and B targets. The onset of motion is synchronized with the arriving synchrotron pulse at $t = 0$. A constant velocity($v = \frac{1}{4}[\frac{\lambda}{\text{ns}}] = 21.5\text{mm/s}$) is applied to the A target before the $t_1 = 15\text{ns}$, and the A target is driven by a new velocity $v_{new} = -v$ for the remained time. The same velocity($v = \frac{1}{4}[\frac{\lambda}{\text{ns}}] = 21.5\text{mm/s}$) is applied to the B target until the $t_1 + \tau = 17\text{ns}$. Afterward, the B target follows the same motion($v_{new} = -v$) which A target has already started since 15ns.

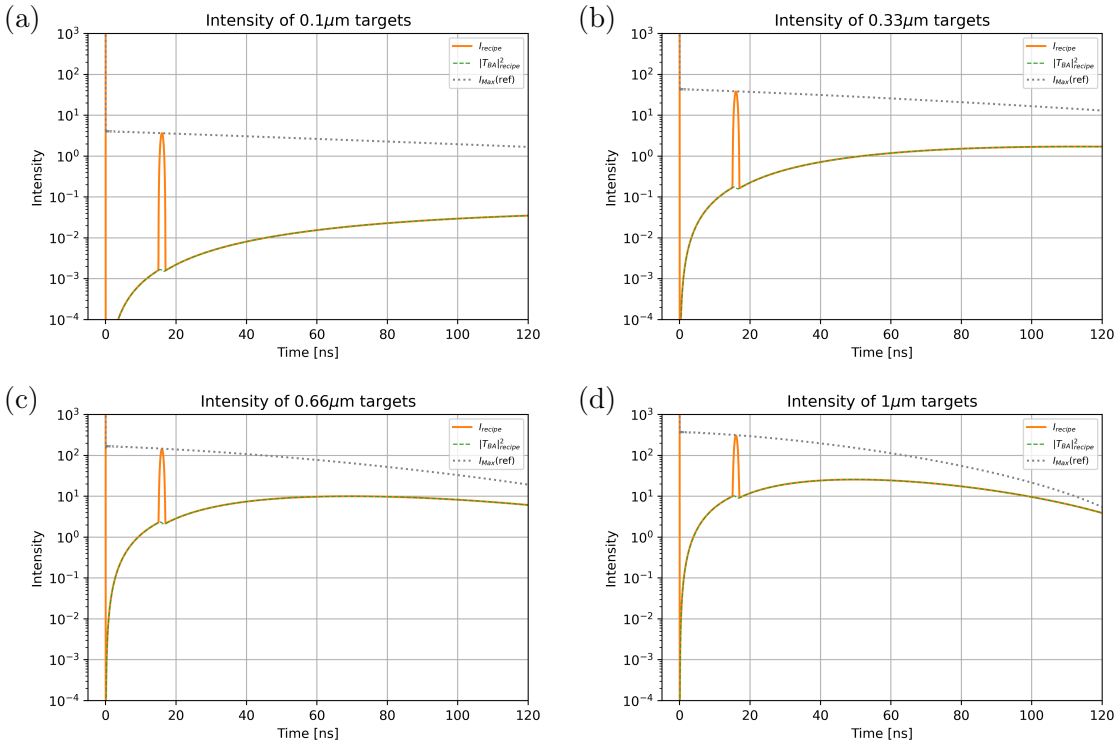

Figure 3.6: (a)-(d) The time intensity of two moving targets of various thicknesses targets. With a magnificient synchrotron pulse at $t = 0\text{ns}$, the controlled moving targets create a second pulse at $t = 15\text{ns}$. The radiative coupling field composes the intensity of each side of the pulses. The related motions are presented at Fig. 3.5(b).

3.2.3 Scattering equation with recipe motion

The scattering field with controlled motions is naturally divided into the same three time intervals. In this subsection, the resultant scattering fields are discussed for each time interval according to motions.

Preliminary step

The purpose of this preparatory step is to prepare the destructive interference con-

dition between two targets at the beginning. The selected method is to use one step motion at $t = 0$ because of its mathematical simplicity. We assume to the step motion is taking place to the B target right after the pulse arrival. The effect of the step motion is the addition of the phase to the singly scattering field of the B target, while the radiative coupling scattering field remains the same. It satisfies the destructive interference after $t = 0$ when the step distance is controlled to $\lambda/2$.

1st time interval $0 < t < t_1$:
The A and B targets start designed motions immediate after the arrival of the synchrotron pulse,

$$\begin{cases} \Delta z_A(t) = vt \times \theta(t) \\ \Delta z_B(t) = (vt - \lambda/2) \times \theta(t), \end{cases} \tag{3.22}$$

where $\Delta z_A(0)$=$\Delta z_B(0) = 0$.

The motion variables decide the property of the scattering fields, substituting motions into Eq. (3.5),

$$\begin{aligned} E_{1\mathrm{st}}(t) =& \delta(t)e^{-i\omega_0 t} \underbrace{-b\frac{J_1(\sqrt{2bt})}{\sqrt{bt}}e^{-\gamma t}e^{ikvt}e^{-i\omega_0 t} - b\frac{J_1(\sqrt{2bt})}{\sqrt{bt}}e^{-\gamma t}e^{ikvt}e^{-i\pi}e^{-i\omega_0 t}}_{=(T_A(t)+T_B(t))_{1\mathrm{st}}} \\ & \underbrace{+\Big(\int_0^t b^2\frac{J_1(\sqrt{2b(t-\tau)})}{\sqrt{b(t-\tau)}}\frac{J_1(\sqrt{2b\tau})}{\sqrt{b\tau}}e^{i\pi}d\tau\Big)e^{-\gamma t}e^{ikvt}e^{-i\pi}e^{-i\omega_0 t}}_{=(T_{BA}(t))_{1\mathrm{st}}} \\ =& \delta(t)e^{-i\omega_0 t} + \Big(\int_0^t b^2\frac{J_1(\sqrt{2b(t-\tau)})}{\sqrt{b(t-\tau)}}\frac{J_1(\sqrt{2b\tau})}{\sqrt{b\tau}}d\tau\Big)e^{-\gamma t}e^{ikvt}e^{-i\omega_0 t}, \end{aligned} \tag{3.23}$$

where the $t > 0$ is dropped since the time information is already given by each time interval.

Two singly scattered fields have opposite signs due to finely tuned relative distance implied as $e^{i\pi}$ at the singly scattered field of B target. Two out-of-phased singly scattered fields cancel each other. Remained radiative coupling field governs the time intensity during this time period, underbraced as $(T_{BA}(t))_{1\mathrm{st}}$. Since the radiative coupling scattering is scattered off from the B target, its phase is relevant to the motion of the B target. It contains the same Doppler-shifted frequency as that of the singly scattered field of the B target. Because the radiative coupling field is also scattered from the B target. The net phase e^{ikvt} modifies the radiative coupling field because the enlarged relative distance, $\Delta z_A(t) - \Delta z_B(t) = \lambda/2$, is offset by $\Delta z_B(t) = kvt - \lambda/2$.

The time intensity is,

$$I_{1\mathrm{st}}(t) = \delta(t) + |\Big(\int_0^t b^2 \frac{J_1(\sqrt{2b(t-\tau)})}{\sqrt{b(t-\tau)}} \frac{J_1(\sqrt{2b\tau})}{\sqrt{b\tau}} d\tau\Big) e^{-\gamma t}|^2 \tag{3.24}$$

The consistent result can be found in Fig. 3.6(a)-(d) during 0ns$< t <$ 15ns. The $I_{1\mathrm{st}}(t)$ is plotted in an orange line for three different thicknesses. The $\delta(t)$ explains the high intensity of synchrotron pulse located at the $t = 0$. The manually produced radiative coupling field $|T_{BA}(t)|^2_{1\mathrm{st}}$ (green) proves that the $I_{1\mathrm{st}}(t)$ after $t = 0$ is only composed of radiative coupling scattering field. Comparing from Fig. 3.6(a) to (d), the $|T_{BA}(t)|^2_{1\mathrm{st}}$ is dependent to the chosen thickness of the targets and tend to have higher intensity for the thick targets. Often the evaluation of the $|T_{BA}(t)|^2_{1\mathrm{st}}$ requires the numerical calculation.

2nd time interval $\mathbf{t_1 < t < t_1 + \tau}$:
The second set of motions is designed to produce a pulse.

$$\begin{cases} \Delta z_A(t) = -v(t - 2t_1) \times (\theta(t - t_1) - \theta(t - t_1 + \tau)) \\ \Delta z_B(t) = (vt - \lambda/2) \times (\theta(t - t_1) - \theta(t - t_1 + \tau)) \end{cases} \tag{3.25}$$

The feature of this time period is two different velocities for the two targets, as seen in Fig. 3.5(b) during 15ns$< t <$ 17ns. This allows two singly scattered fields to make up the time intensity together with the radiative coupling field.

Substituting the motional variables of this time period into Eq. (3.5),

$$E_{2\mathrm{nd}}(t) = \underbrace{-b\frac{J_1(\sqrt{2bt})}{\sqrt{bt}} e^{-\gamma t} e^{-ikvt} e^{-i\omega_0 t} e^{i\phi_1} \theta(t) - b\frac{J_1(\sqrt{2bt})}{\sqrt{bt}} e^{-\gamma t} e^{ikvt} e^{-i\pi} e^{-i\omega_0 t} \theta(t)}_{=(T_A(t)+T_B(t))_{2\mathrm{nd}}}$$
$$\underbrace{+\Big(\int_0^t b^2 \frac{J_1(\sqrt{2b(t-\tau)})}{\sqrt{b(t-\tau)}} \frac{J_1(\sqrt{2b\tau})}{\sqrt{b\tau}} e^{-i\Delta z_{BA}(\tau)} d\tau\Big) e^{-\gamma t} e^{ikvt} e^{-i\pi} e^{-i\omega_0 t}}_{=(T_{BA}(t))_{2\mathrm{nd}}},$$

where the $e^{i\phi_1} = e^{2ikvt_1}$ is a constant phase determined by the velocity and chosen time.

Purposely, the $\Delta z_{BA}(\tau)$ is not substituted in the radiative coupling field term. Because we need to separate the integration according to two different $\Delta z_{BA}(t)$ at $0 < t < t_1$ and $t > t_1$.

$$
\begin{aligned}
& \Big(\int_0^t b^2 \frac{J_1(\sqrt{2b(t-\tau)})}{\sqrt{b(t-\tau)}} \frac{J_1(\sqrt{2b\tau})}{\sqrt{b\tau}} e^{-i\Delta z_{BA}(\tau)} d\tau\Big) e^{-\gamma t} e^{ikvt} e^{-i\pi} e^{-i\omega_0 t} \\
= \quad & \underbrace{\Big(\int_0^{t_1} b^2 \frac{J_1(\sqrt{2b(t-\tau)})}{\sqrt{b(t-\tau)}} \frac{J_1(\sqrt{2b\tau})}{\sqrt{b\tau}} e^{i\pi} d\tau\Big)}_{\text{Const.}} e^{-\gamma t} e^{ikvt} e^{-i\pi} e^{-i\omega_0 t} \\
& + \underbrace{\Big(\int_{t_1}^t b^2 \frac{J_1(\sqrt{2b(t-\tau)})}{\sqrt{b(t-\tau)}} \frac{J_1(\sqrt{2b\tau})}{\sqrt{b\tau}} e^{-2iv\tau} e^{i\phi_1} e^{i\pi} d\tau\Big)}_{\simeq 0} e^{-\gamma t} e^{ikvt} e^{-i\pi} e^{-i\omega_0 t} \\
\simeq \quad & \Big(\int_0^t b^2 \frac{J_1(\sqrt{2b(t-\tau)})}{\sqrt{b(t-\tau)}} \frac{J_1(\sqrt{2b\tau})}{\sqrt{b\tau}} e^{i\pi} d\tau\Big) e^{-\gamma t} e^{ikvt} e^{-i\pi} e^{-i\omega_0 t}
\end{aligned}
$$

The first integration shows exponential decay while the second integration can be assumed zero since it contains the radiative coupling field with off-resonant conditions. Therefore, the overall radiative coupling field stops increasing but exponentially decays during this time period. The existing radiative coupling field can be understood in a way that the decay of nuclear excitation at $t > t_1$ which was pumped during the $0 < t < t_1$ by scattered field from A target. The radiative coupling channel was opened during the $0 < t < t_1$ since two targets move at the same velocity and the in-resonant condition has been satisfied. The last approximation is valid when considered time is near t_1, $t \simeq t_1$, and the decay rate γ is small. Considering we desire to produce a timely narrow pulse and long lifetime of the ^{57}Fe¸ above condition are valid.

Using above appoximation, an equation of timely narrow pulse is read as

$$
\begin{aligned}
E_{\text{2nd}}(t) \simeq & -b \frac{J_1(\sqrt{2bt})}{\sqrt{bt}} e^{-\gamma t} e^{i\phi_1/2} e^{-i\omega_0 t} (e^{-i(kvt-\phi_1/2)} - e^{i(kvt-\phi_1/2)}) \\
& + \Big(\int_0^t b^2 \frac{J_1(\sqrt{2b(t-\tau)})}{\sqrt{b(t-\tau)}} \frac{J_1(\sqrt{2b\tau})}{\sqrt{b\tau}} e^{i\pi} d\tau\Big) e^{-\gamma t} e^{ikvt} e^{-i\pi} e^{-i\omega_0 t}
\end{aligned} \tag{3.26}
$$

The time intensity is,

$$
\begin{aligned}
I_{\text{2nd}}(t) \simeq \quad & \underbrace{|2b \frac{J_1(\sqrt{2bt})}{\sqrt{bt}} e^{-\gamma t}|^2 |\sin(kvt - \phi_1/2)|^2}_{\text{Pulse term 1}} \\
& + \underbrace{4b^3 \frac{J_1(\sqrt{2bt})}{\sqrt{bt}} e^{-2\gamma t} \Big(\int_0^t \frac{J_1(\sqrt{2b(t-\tau)})}{\sqrt{b(t-\tau)}} \frac{J_1(\sqrt{2b\tau})}{\sqrt{b\tau}} d\tau\Big) |\sin(kvt - \phi_1/2)|^2}_{\text{Pulse term 2}} \\
& + \underbrace{|\Big(\int_0^t b^2 \frac{J_1(\sqrt{2b(t-\tau)})}{\sqrt{b(t-\tau)}} \frac{J_1(\sqrt{2b\tau})}{\sqrt{b\tau}} d\tau\Big) e^{-\gamma t}|^2}_{=|T_{BA}(t)|^2_{\text{2nd}}},
\end{aligned} \tag{3.27}
$$

where one trigonometry identity, $1 - \cos 2x = 2\sin^2 x$, is used for the second term.

The pulse equation contains two more terms in addition to the radiative coupling field. These two terms imprint a beating pattern to the time intensity. The pulse terms are zero at t_1 with $kvt_1 - \phi_1/2 = 0$. And its maximum intensity of the pulse is equal to $|T_A + T_B - T_{BA}|^2$ at $t = t_1 + \tau/2$, where the T_A, T_B, T_{BA} are the singly scattered fields and radiative coupling field of static two targets scattering equation, Eq. (3.2).

$$\mathrm{Max}\{I_{\mathrm{2nd}}(t)\} = |T_A + T_B - T_{BA}|^2_{t=t_1+\tau/2} \tag{3.28}$$

where the I_{rest} is defined as $|T_A + T_B + T_{BA}|^2$ in Eq. (3.4) for the reference.

The speed of beating imposes a condition for the current time interval and pulse duration. By restricting the beating to oscillate once, we can see a single beating that can be regarded as a pulse in time intensity. If the two targets follow the proposed motion(Eq. (3.25)) for a longer time, the time intensity keeps oscillating and several beating patterns will be observed.

The time condition for the one beating pattern is,

$$\tau = \frac{\lambda}{2v} \tag{3.29}$$

The Eq. (3.27) and Eq. (3.29) explain a produced pulse in Fig. 3.6(a)-(d) located 15ns$< t <$ 17ns. Because pulse terms are zero at t_1, the intensity starts from $I_{\mathrm{2nd}}(t_1) = |T_{BA}(t_1)|^2_{\mathrm{2nd}}$. Later, the intensity (orange) is increased because of the pulse terms during this period. The intensity reaches the maximum point at the $t = t_1+\tau/2 = 16$ns which is equal to $|T_A+T_B-T_{BA}|^2(t)$(grey), labeled as $I_{\mathrm{MAX}}(t)$ to show maximum pulse intensity at a different choice of t_1. And it starts decreasing down. At the $t = t_1 + \tau = 17$ns, the intensity becomes to $I_{\mathrm{2nd}}(t_1 + \tau) = |T_{BA}(t_1 + \tau)|^2_{\mathrm{2nd}}$.

3rd time interval $\mathbf{t_1 + \tau < t}$

Assuming the earlier set of motions is continued during $\tau = \frac{\lambda}{2v}$, new positions of two targets are ready to satisfy the second destructive interference condition. Driving the B target into the same velocity as the A target, the destructive interference can be recovered after the pulse. Then it produces another radiative coupling field governing period.

$$\begin{cases} \Delta z_A(t) = -v(t - 2t_1) \times \theta(t - t_1 + \tau) \\ \Delta z_B(t) = -(v(t - 2t_1) - \lambda/2) \times \theta(t - t_1 + \tau) \end{cases} \tag{3.30}$$

Substituting motional variables into Eq. (3.5), a similar scattering field equation is obtained with that of the first time interval.

$$
\begin{aligned}
E_{3\mathrm{rd}}(t) = & -b\frac{J_1(\sqrt{2bt})}{\sqrt{bt}}e^{-\gamma t}e^{-ikvt}e^{i\phi_1}e^{-i\omega_0 t} - b\frac{J_1(\sqrt{2bt})}{\sqrt{bt}}e^{-\gamma t}e^{-ikvt}e^{i\pi}e^{i\phi_1}e^{-i\omega_0 t} \\
& + \Big(\int_0^{t_1} b^2\frac{J_1(\sqrt{2b(t-\tau)})}{\sqrt{b(t-\tau)}}\frac{J_1(\sqrt{2b\tau})}{\sqrt{b\tau}}e^{i\pi}d\tau\Big)e^{-\gamma t}e^{-ikvt}e^{i\pi}e^{i\phi_1}e^{-i\omega_0 t} \\
& + \Big(\int_{t_1}^{t_1+\tau} b^2\frac{J_1(\sqrt{2b(t-\tau)})}{\sqrt{b(t-\tau)}}\frac{J_1(\sqrt{2b\tau})}{\sqrt{b\tau}}e^{-2iv\tau}d\tau\Big)e^{-\gamma t}e^{-ikvt}e^{i\pi}e^{i\phi_1}e^{-i\omega_0 t} \\
& + \Big(\int_{t_1+\tau}^{t} b^2\frac{J_1(\sqrt{2b(t-\tau)})}{\sqrt{b(t-\tau)}}\frac{J_1(\sqrt{2b\tau})}{\sqrt{b\tau}}e^{-i\pi}d\tau\Big)e^{-\gamma t}e^{-ikvt}e^{i\pi}e^{i\phi_1}e^{-i\omega_0 t} \\
\simeq & \quad \Big(\int_0^{t} b^2\frac{J_1(\sqrt{2b(t-\tau)})}{\sqrt{b(t-\tau)}}\frac{J_1(\sqrt{2b\tau})}{\sqrt{b\tau}}d\tau\Big)e^{-\gamma t}e^{-ikvt}e^{i\phi_1}e^{-i\omega_0 t}, \qquad (3.31)
\end{aligned}
$$

where the two singly scattered fields don't contribute to the time intensity because of recovered destructive interference. If pulse generating motion is finished after a very short period of time, the radiative coupling field equation corresponding to t_1 to $t_1 + \tau$ becomes negligible and the last approximation can be held.

The intensity is approximated in a similar fashion,

$$
I_{3\mathrm{rd}}(t) \simeq |\Big(\int_0^{t} b^2\frac{J_1(\sqrt{2b(t-\tau)})}{\sqrt{b(t-\tau)}}\frac{J_1(\sqrt{2b\tau})}{\sqrt{b\tau}}d\tau\Big)e^{-\gamma t}|^2 \qquad (3.32)
$$

The second radiative coupling field governing period is observed after the pulse (17ns<t) in Fig. 3.6(a)-(d). The radiative coupling field has increased over most of the measurement time, but its intensity is still lower than the intensity of the produced pulse. Comparing each figure, it becomes clear that the advantage of using a thin target. The thinner targets provide a higher intensity contrast between the produced pulse and the intensity of the radiative coupling field.

3.2.4 Time condition for delay time of pulse

The pulse origins from the singly scattered fields and contributes to the time intensity which were referred as pulse terms in Eq. (3.27). However, the added pulse terms are not always making the intensity increase, the time intensity during this time can also fall if too late time is chosen for a pulse generation. The $t_1 = 15$ns has chosen to make the sum of pulse terms to be positive for all targets.

The pulse is generated when the sum of the two pulse terms is positive in Eq. (3.27).

Formulating the condition,

$$
\begin{aligned}
0 \;<\; & \underbrace{|2b\frac{J_1(\sqrt{2bt})}{\sqrt{bt}}e^{-\gamma t}|^2|\sin(kvt-\phi_1/2)|^2}_{\text{Pulse term 1}} \\
& + \underbrace{4b^3\frac{J_1(\sqrt{2bt})}{\sqrt{bt}}e^{-2\gamma t}\big(\int_0^t \frac{J_1(\sqrt{2b(t-\tau)}}{\sqrt{b(t-\tau)}}\frac{J_1(\sqrt{2b\tau})}{\sqrt{b\tau}}d\tau\big)|\sin(kvt-\phi_1/2)|^2}_{\text{Pulse term 2}}
\end{aligned}
$$

Dividing by $|\sin(kvt-\phi/2)|^2$ and adding $|\big(\int_0^t b^2\frac{J_1(\sqrt{2b(t-\tau)}}{\sqrt{b(t-\tau)}}\frac{J_1(\sqrt{2b\tau})}{\sqrt{b\tau}}d\tau\big)e^{-\gamma t}|^2$ at both hand sides,

$$
\begin{aligned}
& |\big(\int_0^t b^2\frac{J_1(\sqrt{2b(t-\tau)}}{\sqrt{b(t-\tau)}}\frac{J_1(\sqrt{2b\tau})}{\sqrt{b\tau}}d\tau\big)e^{-\gamma t}|^2 \\
< \;& |\big(\int_0^t b^2\frac{J_1(\sqrt{2b(t-\tau)}}{\sqrt{b(t-\tau)}}\frac{J_1(\sqrt{2b\tau})}{\sqrt{b\tau}}d\tau\big)e^{-\gamma t}|^2 \\
& + |2b\frac{J_1(\sqrt{2bt})}{\sqrt{bt}}e^{-\gamma t}|^2 + 4b^3\frac{J_1(\sqrt{2bt})}{\sqrt{bt}}e^{-2\gamma t}\big(\int_0^t \frac{J_1(\sqrt{2b(t-\tau)}}{\sqrt{b(t-\tau)}}\frac{J_1(\sqrt{2b\tau})}{\sqrt{b\tau}}d\tau\big)
\end{aligned}
$$

This inequation can be re-expressed in terms of the $T_A(t)$, $T_B(t)$ and $T_{BA}(t)$ defined in Eq. (3.2) for the static two targets. The left-hand side is equal to the intensity of the radiative coupling field $|T_{BA}(t)|^2$. And the right-hand side is turned to $|T_A(t)+T_B(t)-T_{BA}(t)|^2$ at $t>0$.

$$
|T_{BA}(t)|^2 < |T_A(t)+T_B(t)-T_{BA}(t)|^2 \tag{3.33}
$$

The motion will shape the waveform into pulse if the chosen t_1 satiesfies the given conditions. However, the produced pulse is also necessary to be more intensive than background over the measurement time. Besides, the relative intensity between radiative coupling field and the produced pulse's intensity can be another consideration to set the maximum delay time for the pulse.

In these reasons, we can set the effective maxium pulse delay at $t=t_M$ satisfying $\{|T_{BA}(t_M)|^2\}| = \text{Max}\{|T_{BA}(t)|^2\}$. Then, there are following benefits. First, the time before $\text{Max}\{|T_{BA}(t)|^2\}$ always satisfy Eq. (3.33). Second, it allows an acceptable relative intensity between the produced pulse and the radiative coupling field, though the exact values are only accessible by numerical calculation. Imagine that if the t_1 is chosen at 100ns for 1μm target. The pulse will be undesirably produced with its maximum intensity as $|T_A(t)+T_B(t)-T_{BA}(t)|^2_{t=100\text{ns}}$(grey) after the huge intensity of the radiative coupling field. We can safely set the maximum pulse-to-pulse delay by the $\text{Max}\{|T_{BA}(t)|^2\}$. Numerically computing the effective maximum pulse delay, it is 198.94ns(20.05), 113.44ns(7.968), 69.40ns(6.097), 49.65ns(5.497) can be found for 0.1μm, 0.33μm, 0.66μm, and 1μm. The numbers in bracket refer respective relative intensity at the effective maximum pulse delay.

3.2.5 Pulse-to-pulse coherence

The motivation of the study is to find an alternative way to imply the coherent pump and probe measurement in the hard X-ray regime. Following the recipes, the motions of the two targets successfully generate a pulse with nanoseconds duration at the desired time $t = t_1$ which follows after the synchrotron pulse at $t = 0$. But the pulse-to-pulse coherence is not yet answered during the last subsection.

The pulse to pulse coherence is imprinted from the property of a synchrotron pulse and coherent scattering of the Mössbauer targets. It might sound unreasonable to use a synchrotron pulse for coherent two pulses scheme since the synchrotron pulse is known for its poor temporal coherence [30]. It seems even unable to coherently excite two distanced targets. However, the key is photons with frequency ω_i can preserve its phase quite well even after long propagation despite of fast loss of coherence with other ω_j photons [54]. Such a phenomenon is not a unique property of the synchrotron pulse, rather it is the property of any light source even one white bulb can show. Back to the suggested scheme, the concept of coherent two pulses can be well established if we restrict the scattering to process near natural frequency, ω_0 where a large advantage comes with a long lifetime of nuclear excitation of ^{57}Fe.

3.2.6 General motion for shaping

Lastly, the Eq. (3.21) might mislead that two linear motions are necessary for the shaping waveform into pulses. The key to the suggested scheme is controlling interference conditions for long periods of time except for the short period for a pulse. Recalling the destructive interferences are only dependent on the targets' relative distance and the beating can be produced with other motions, there are several more options that can be adopted for the other scheme.

The general motions are

$$\begin{cases} 0 < t < t_1 : & \Delta z_A(t) = \Delta z_B(t) \pm \frac{\lambda}{2} \\ t_1 < t < t_1 + \tau : & \Delta z_A(t), \text{ and } \Delta z_B(t) \\ t_1 + \tau < t : & \Delta z_A(t) = \Delta z_B(t) \pm \frac{\lambda}{2}, \end{cases} \tag{3.34}$$

where corresponding pulse duration equation can be found as

$$k \int_{t_1}^{t_1+\tau} (\partial_t \Delta z_B(t) - \partial_t \Delta z_A(t)) dt = \pi. \tag{3.35}$$

In other words, the motions can generate a pulse if the relative distance is controlled as $\frac{\lambda}{2}$ for most of the time, and its relative motions make the evolving phase (or pulse area) equal to π during pulse generation time.

3.3 Application: shaping scheme with enhanced intensty contrast

A perfectly generated pulse would expect absolute suppressions of intensity before and after the pulse. However, the scattering field is ceaselessly impinged at detector via radiative coupling channel and set the time condition as well as lower intensity contrast for the produced pulse. The radiative coupling scattering is difficult to cancel with the motional control since its amplitude is more complicate than the singly scattered fields and have no counterpart.

There might be largely two different approaches to improve the proposed scheme. The first idea is to enhance the intensity of the pulse, directly. The latter is to suppress down the level of radiative coupling field. The beating-origined pulse already restricts a dramatic improvement by the first approach Eq. (3.28). Hyperfine interaction enables the nuclei to exhibit polarization depedent scattering. Using the polarization dependent scattering, the radiative coupling field will be suppressed and the consequently intensity contrast of pulse will be enhanced. The principle of the supression can be found in the different propagation effect depending on polarization state of the incident field. The polarization dependent scattering makes the in-resonant radiative coupling fields interfere destructively [82] and the radiative coupling fields in off-resonant condition only contribute to the time intensity.

3.3.1 Nuclear forward scattering with $\hat{k}$,$-\hat{k}$ targets

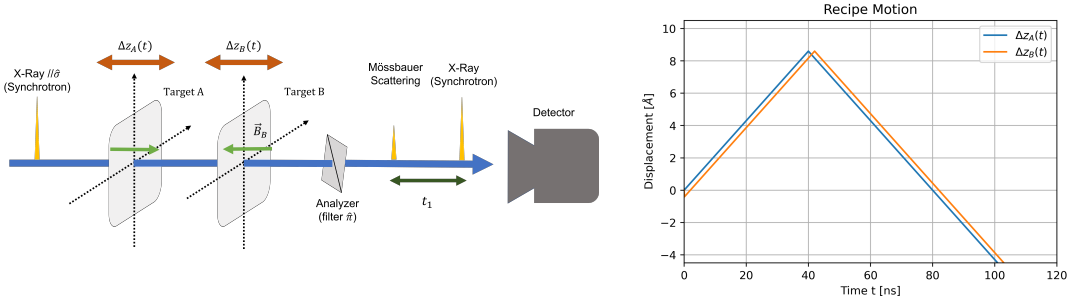

(a) Setting of two targets in $\hat{k}$,$-\hat{k}$ configuration **(b)** Recipe motion for waveform shaping

Figure 3.7: (a) The figure shows a set of aligned Mössbauer targets to realize high intensity contrast pulse. Magnetic dipole moments of two targets are aligned along $\hat{k}$ and $-\hat{k}$, respectively. This alignment cancels in-resonant radiative coupling channel. The analyzer is installed at the backstream of the two targets to screen fields scattered to $\hat{\pi}$ polarization state. (b) The example motions of waveform shaping with pulse at 40ns. The shaped waveform equation is discussed in Section 3.3.2.

External magnets can align the internal nuclear magnetic dipole moments in a desired direction [68]. In this chapter the nuclear dipole moments are set to $\hat{k}$

and -$\hat{k}$ direction for high intensity contrast pulse, where $\hat{k}$ points the propagation direction of synchrotron pulse.

Nuclear forward scattering matrix

The total scattering of the two targets system are described as series of two scatterings at A and B targets in order.

$$\begin{pmatrix} E_\sigma(\omega) \\ E_\pi(\omega) \end{pmatrix} = e^{i\mathbf{N_B}d} e^{i\mathbf{N_A}d} E_0(\omega) = e^{i\mathbf{N_B}d} e^{i\mathbf{N_A}d} \begin{pmatrix} E_{0\sigma}(\omega) \\ E_{0\pi}(\omega) \end{pmatrix}, \tag{3.36}$$

where the $E_0(\omega)$ represents the incoming pumping field to the two nuclear targets. The $E_0(\omega)$ has two polarization components $\hat{\sigma}$ and $\hat{\pi}$. The scattering is described with the nuclear forward scattering matrix of each target, $e^{i\mathbf{N_A}d}$ and $e^{i\mathbf{N_B}d}$.

The nuclear forward scattering matrix of the resting A target aligned in $\hat{k}$ is calculated from Eq. (2.40),

$$\mathbf{N_A} = \frac{3}{8}\frac{\lambda}{2\pi} \begin{pmatrix} F_1 + F_{-1} & -i(F_1 - F_{-1}) \\ i(F_1 - F_{-1}) & F_1 + F_{-1} \end{pmatrix} \tag{3.37}$$

The two transition amplitudes $F_{\pm 1}$, are defined as,

$$F_1 = f_{LM}\left(\frac{1}{1+\alpha}\right)\left(\frac{1}{2j_0+1}\right) \times \left(\frac{\Gamma}{\hbar(\omega_1 - \omega) - i\Gamma/2} + \frac{1}{3}\frac{\Gamma}{\hbar(\omega_4 - \omega) - i\Gamma/2}\right) \tag{3.38}$$

$$F_{-1} = f_{LM}\left(\frac{1}{1+\alpha}\right)\left(\frac{1}{2j_0+1}\right) \times \left(\frac{1}{3}\frac{\Gamma}{\hbar(\omega_3 - \omega) - i\Gamma/2} + \frac{\Gamma}{\hbar(\omega_6 - \omega) - i\Gamma/2}\right), \tag{3.39}$$

where the Clebsch-Gordan coefficients are explictly evaluated, and each ω_i represents the transition frequency of corresponding transitions Eq. (2.37).

Diagonalize the nuclear forward scattering matrix,

$$\begin{aligned} \mathbf{N_A} =& \frac{3}{4}\frac{\lambda}{2\pi} \begin{pmatrix} \frac{1}{\sqrt{2}} & \frac{i}{\sqrt{2}} \\ \frac{i}{\sqrt{2}} & \frac{1}{\sqrt{2}} \end{pmatrix} \begin{pmatrix} F_1 & 0 \\ 0 & F_{-1} \end{pmatrix} \begin{pmatrix} \frac{1}{\sqrt{2}} & -\frac{i}{\sqrt{2}} \\ -\frac{i}{\sqrt{2}} & \frac{1}{\sqrt{2}} \end{pmatrix} \\ =& \mathbf{U_A}\mathbf{F_A}\mathbf{U_A^\dagger}, \end{aligned} \tag{3.40}$$

where matrix $\mathbf{U_A}$ and $\mathbf{U_A^\dagger}$ absorb $\frac{1}{2}$ from the coefficient.

We will use the following definitions for a simple notation.

- $\mathbf{U_A} = \begin{pmatrix} \frac{1}{\sqrt{2}} & \frac{i}{\sqrt{2}} \\ \frac{i}{\sqrt{2}} & \frac{1}{\sqrt{2}} \end{pmatrix}$
- $\mathbf{F_A} = \frac{3}{4}\frac{\lambda}{2\pi} \begin{pmatrix} F_1 & 0 \\ 0 & F_{-1} \end{pmatrix}$
- $\mathbf{U_A^\dagger}$ represents the complex conjugate of $\mathbf{U_A}$

The similar result can be found at the nuclear forward scattering matrix of the B target which is aligned in anti-parallel direction, -$\hat{k}$.

$$\begin{aligned}\mathbf{N_B} &= \frac{3}{8}\frac{\lambda}{2\pi}\begin{pmatrix} F_1+F_{-1} & i(F_1-F_{-1}) \\ -i(F_1-F_{-1}) & F_1+F_{-1}\end{pmatrix} \\ &= \frac{3}{4}\frac{\lambda}{2\pi}\begin{pmatrix} \frac{1}{\sqrt{2}} & -\frac{i}{\sqrt{2}} \\ -\frac{i}{\sqrt{2}} & \frac{1}{\sqrt{2}}\end{pmatrix}\begin{pmatrix} F_1 & 0 \\ 0 & F_{-1}\end{pmatrix}\begin{pmatrix} \frac{1}{\sqrt{2}} & \frac{i}{\sqrt{2}} \\ \frac{i}{\sqrt{2}} & \frac{1}{\sqrt{2}}\end{pmatrix} \\ &= \mathbf{U_B F_A U_B^\dagger} \end{aligned} \tag{3.41}$$

with following definitions.

- $\mathbf{U_B} = \begin{pmatrix} \frac{1}{\sqrt{2}} & -\frac{i}{\sqrt{2}} \\ -\frac{i}{\sqrt{2}} & \frac{1}{\sqrt{2}}\end{pmatrix} = \mathbf{U_A^\dagger}$
- $\mathbf{F_B} = \frac{3}{4}\frac{\lambda}{2\pi}\begin{pmatrix} F_1 & 0 \\ 0 & F_{-1}\end{pmatrix} = \mathbf{F_A}$
- $\mathbf{U_B^\dagger}$ represents the complex conjugate of $\mathbf{U_B}$

The matrix exponential is easily calculated with a diagonalized matrix.

$$\begin{aligned} e^{i\mathbf{N_A}d} &= (1 + \mathbf{U_A F_A U_A^\dagger} + \frac{1}{2!}\mathbf{U_A F_A^2 U_A^\dagger} + \cdots) \\ &= \mathbf{U_A} e^{i\mathbf{F_A}d}\mathbf{U_A^\dagger}, \end{aligned}$$

where the identity matrix outcomes from the matrix calculation of $\mathbf{U_A}$ and $\mathbf{U_A^\dagger}$, $I = \mathbf{U_A U_A^\dagger}$.

Similarly,

$$\begin{aligned} e^{i\mathbf{N_B}d} &= (1 + \mathbf{U_B F_B U_B^\dagger} + \frac{1}{2!}\mathbf{U_B F_B^2 U_B^\dagger} + \cdots) \\ &= \mathbf{U_B} e^{i\mathbf{F_B}d}\mathbf{U_B^\dagger} \\ &= \mathbf{U_A^\dagger} e^{i\mathbf{F_A}d}\mathbf{U_A}, \end{aligned}$$

where the $\mathbf{U_B} = \mathbf{U_A^\dagger}$ and $\mathbf{F_B} = \mathbf{F_A}$ are used at the last equation.

The scattering field of the two targets is,

$$\begin{aligned} E(\omega) &= e^{i\mathbf{N_B}d} e^{i\mathbf{N_A}d} E_0(\omega) \\ &= \mathbf{U_A^\dagger} e^{i\mathbf{F_A}d}\mathbf{U_A U_A} e^{i\mathbf{F_A}d}\mathbf{U_A^\dagger} E_0(\omega) \\ &= i\mathbf{U_A^\dagger} e^{i\mathbf{F_A}d}\begin{pmatrix} 0 & 1 \\ 1 & 0\end{pmatrix} e^{i\mathbf{F_A}d}\mathbf{U_A^\dagger}\begin{pmatrix} E_{0\sigma}(\omega) \\ E_{0\pi}(\omega)\end{pmatrix}, \end{aligned} \tag{3.42}$$

where $\mathbf{U_A U_A}$ and two polarization components for the incident field are explictly written at the last equation.

And the $\mathbf{F_A}$ also satisfies

$$e^{i\mathbf{F_A}d} = \begin{pmatrix} e^{i\frac{3}{4}\frac{\lambda}{2\pi}F_1 d} & 0 \\ 0 & e^{i\frac{3}{4}\frac{\lambda}{2\pi}F_{-1}d} \end{pmatrix} = \begin{pmatrix} e^{\frac{3}{4}\frac{-ib}{\hbar(\omega-\omega_1)+i\gamma}+\frac{1}{4}\frac{-ib}{\hbar(\omega-\omega_4)+i\gamma}} & 0 \\ 0 & e^{\frac{1}{4}\frac{-ib}{\hbar(\omega-\omega_3)+i\gamma}+\frac{3}{4}\frac{-ib}{\hbar(\omega-\omega_6)+i\gamma}}, \end{pmatrix},$$

with three definitions $\gamma = \Gamma/2$, $b = \Gamma_c d$, and the $\Gamma_c =$ is the enhanced decay width defined as $\frac{\lambda}{2\pi} f_{LM} \frac{1}{1+\alpha} \frac{1}{2j_0+1}\Gamma$.

Each component of the $e^{i\mathbf{F_A}d}$ describes the scattering with certain transitions. Because hyperfine transitions of iron are far separated than its ultranarrow transition width γ, the each transition can be regarded independently.

$$e^{\frac{3}{4}\frac{-ib}{\hbar(\omega-\omega_1)+i\gamma}+\frac{1}{4}\frac{-ib}{\hbar(\omega-\omega_4)+i\gamma}} \simeq e^{\frac{3}{4}\frac{-ib}{\hbar(\omega-\omega_1)+i\gamma}} + e^{\frac{1}{4}\frac{-ib}{\hbar(\omega-\omega_4)+i\gamma}} \equiv R_1(\omega) + R_4(\omega), \tag{3.43}$$

where the response function of ω_1 and ω_4 transitions are defined, respectively.

The response function of ω_3 and ω_6 transitions are defined in the same way for the (2,2) component of $e^{i\mathbf{F_A}d}$.

$$e^{\frac{1}{4}\frac{-ib}{\hbar(\omega-\omega_3)+i\gamma}+\frac{3}{4}\frac{-ib}{\hbar(\omega-\omega_6)+i\gamma}} \simeq e^{\frac{1}{4}\frac{-ib}{\hbar(\omega-\omega_3)+i\gamma}} + e^{\frac{3}{4}\frac{-ib}{\hbar(\omega-\omega_6)+i\gamma}} \equiv R_3(\omega) + R_6(\omega), \tag{3.44}$$

Substituting Eq. (3.43) and Eq. (3.44), into Eq. (3.42), the scattering field is represented as followed.

$$\begin{aligned} \begin{pmatrix} E_\sigma(\omega) \\ E_\pi(\omega) \end{pmatrix} &= i\mathbf{U}_\mathbf{A}^\dagger \begin{pmatrix} 0 & \underbrace{(R_1^B + R_4^B)}_{\text{Target B}}\underbrace{(R_3^A + R_6^A)}_{\text{Target A}} \\ \underbrace{(R_3^B + R_6^B)}_{\text{Target B}}\underbrace{(R_1^A + R_4^A)}_{\text{Target A}} & 0 \end{pmatrix} \mathbf{U}_\mathbf{A}^\dagger \begin{pmatrix} 1 \\ 0 \end{pmatrix} \\ &= \frac{1}{2}\begin{pmatrix} (R_1^B + R_4^B)(R_3^A + R_6^A) + (R_3^B + R_6^B)(R_1^A + R_4^A) \\ i\big((R_1^B + R_4^B)(R_3^A + R_6^A) - (R_3^B + R_6^B)(R_1^A + R_4^A)\big) \end{pmatrix}, \end{aligned}$$

where the target's $\hat{\sigma}$ is aligned parallel to polarization direction of synchrotron pulse, $E_{0\sigma}(\omega) = 1$ and $E_{0\pi}(\omega) = 0$ in Eq. (3.42). The superindices 'B' and 'A' indicate the owner of the response function. Order of each matrix component follows in a way that scattering response function of the B target comes after scattering response function of the A target.

σ analyzer

The $\hat{k}$,$-\hat{k}$ dipole alignment scatters incoming field into both $\hat{\sigma}$, $\hat{\pi}$ polarized states. Because we plan to use both the synchrotron pulse and the Mössbauer scattering field for the coherent two pulses, let us apply an analyzer parallel to $\hat{\sigma}$ at the backstream

of the target B.

$$\begin{pmatrix} E_\sigma(\omega) \\ E_\pi(\omega) \end{pmatrix} = \frac{1}{2} \underbrace{\begin{pmatrix} 1 & 0 \\ 0 & 0 \end{pmatrix}}_{\sigma \text{ analyzer}} \begin{pmatrix} (R_1^B + R_4^B)(R_3^A + R_6^A) + (R_3^B + R_6^B)(R_1^A + R_4^A) \\ i\big((R_1^B + R_4^B)(R_3^A + R_6^A) - (R_3^B + R_6^B)(R_1^A + R_4^A)\big) \end{pmatrix}$$
$$= \frac{1}{2} \begin{pmatrix} (R_1^B + R_4^B)(R_3^A + R_6^A) + (R_3^B + R_6^B)(R_1^A + R_4^A) \\ 0 \end{pmatrix} \tag{3.45}$$

Scattering field of static targets

Response functions are decomposed into two parts, non-interacting part and the scattered part: $R_i(\omega) + R_j(\omega) = 1 + T_i(\omega) + T_j(\omega)$, where the $R_i(\omega)$ refers the response function of ω_i transition and its scattered part is $T_i(\omega)$, as defined in Eq. (3.43), and Eq. (3.44).

Considering only the $\hat{\sigma}$ component,

$$\begin{aligned} E_\sigma(\omega) &= \frac{1}{2}((R_1^B + R_4^B)(R_3^A + R_6^A) + (R_3^B + R_6^B)(R_1^A + R_4^A)) \\ &= 1 + \frac{1}{2}(T_1^A + T_3^A + T_4^A + T_6^A) + \frac{1}{2}(T_1^B + T_3^B + T_4^B + T_6^B) \\ &+ \frac{1}{2}(T_1^B T_3^A + T_4^B T_3^A + T_1^B T_6^A + T_4^B T_6^A + T_3^B T_1^A + T_3^B T_4^A + T_6^B T_1^A + T_6^B T_4^A), \end{aligned} \tag{3.46}$$

where all functions are defined in the frequency space. The noticible feature of this configuration is found on the radiative coupling scattering terms. There is **no radiative coupling channel between same transitions**, such terms: $T_i^B T_i^A$. Instead, the radiation from A target interacts with B target under off-resonant conditions [82].

Because of similarity we can use the same method in Section 3.1.4 to approximate the complicate radiative coupling field. Then, all terms relevant to off-resonant radiative coupling field can be expressed as read.

$$\begin{aligned} E_\sigma(\omega) &= 1 + (T_1^A + T_3^A + T_4^A + T_6^A) + (T_1^A T_3^A + T_4^A T_3^A + T_1^A T_6^A + T_4^A T_6^A) \\ &\simeq 1 + T_1^A(1 + \kappa_1) + T_3^A(1 + \kappa_3) + T_4^A(1 + \kappa_4) + T_6^A(1 + \kappa_6) \end{aligned} \tag{3.47}$$

where the calculation can be found in Appendix A.5.

And the κ_1 and κ_3 are evaluated as

$$\kappa_1 = -\kappa_6 = -i\frac{1}{4}(\frac{1}{2}\frac{b}{\Delta_{13}} + \frac{1}{2}\frac{3b}{\Delta_{16}}) \tag{3.48}$$

$$\kappa_3 = -\kappa_4 = -i\frac{1}{4}(\frac{1}{2}\frac{3b}{\Delta_{31}} + \frac{1}{2}\frac{b}{\Delta_{34}}), \tag{3.49}$$

where the detuning between the two transitions are defined as $\Delta_{ij} = \hbar(\omega_i - \omega_j)$ in Table 2.1. The κ_1 and κ_3 for the 0.1μm, $\kappa_1 = (2.55\times10^{-3})i$ and $\kappa_3 = -(4.43\times10^{-3})i$ are evaluated, and the κ_1 and κ_3 increases proportional to the target's thickness.

Our interest is the time intensity measurement. Transforming each term to obtain the scattering field function in time with off-resonant radiative coupling field,

$$\begin{aligned} E_\sigma(t) = \delta(t)e^{-i\omega t} &- \frac{3}{4}b\frac{J_1\big(\sqrt{2\times\frac{3}{4}bt}\big)}{\sqrt{\frac{3}{4}bt}} \times e^{-\gamma t}(e^{-i\omega_1 t} + e^{-i\omega_6 t}) \\ &- \frac{1}{4}b\frac{J_1\big(\sqrt{2\times\frac{1}{4}bt}\big)}{\sqrt{\frac{1}{4}bt}} \times e^{-\gamma t}(e^{-i\omega_3 t} + e^{-i\omega_4 t}) \\ &+ O(\text{weak radi. coup.}), \end{aligned} \tag{3.50}$$

where the O(weak radi. field) is the transformed radiative coupling field.

$$\begin{aligned} O(\text{weak radi. field}) = \quad & \kappa_1 \times \frac{3}{4}b\frac{J_1\big(\sqrt{3bt/2}\big)}{\sqrt{3bt/4}}e^{-\gamma t}(e^{-i\omega_1 t} - e^{-i\omega_6 t}) \\ &+ \kappa_3 \times \frac{b}{4}\frac{J_1\big(\sqrt{bt/2}\big)}{\sqrt{bt/4}}e^{-\gamma t}(e^{-i\omega_3 t} - e^{-i\omega_4 t}), \end{aligned} \tag{3.51}$$

3.3.2 Shaped pulse waveform with high contrast

Motions

The scattering waveform for the $\hat{k}$, -$\hat{k}$ configurations can be shaped into short pulses with the same recipe motion, Eq. (3.21).

$$\begin{cases} \Delta z_A(t) = & vt \times (\theta(t) - \theta(t - t_1)) \\ & -v(t - 2t_1) \times \theta(t - t_1) \\ \Delta z_B(t) = & vt \times (\theta(t) - \theta(t - t_1 - \tau)) \\ & -v(t - 2t_1 - 2\tau) \times \theta(t - t_1 - \tau) - \frac{\lambda}{2}\theta(t) \end{cases}$$

The Fig. 3.7(b) shows a set of motions with v=$\frac{1}{4}[\frac{\lambda}{\text{ns}}]$, $t_1 = 40$ns to compute Fig. 3.8(a)-(d).

Scattering field of moving targets

The Eq. (3.50) and Eq. (3.51) describe the scattering field for the resting two targets in $\hat{k}$ and $-\hat{k}$ configuration. We need to evaluate the scattering fields based on Eq. (3.5). The singly scattered fields are easily evaluated for the moving targets, and

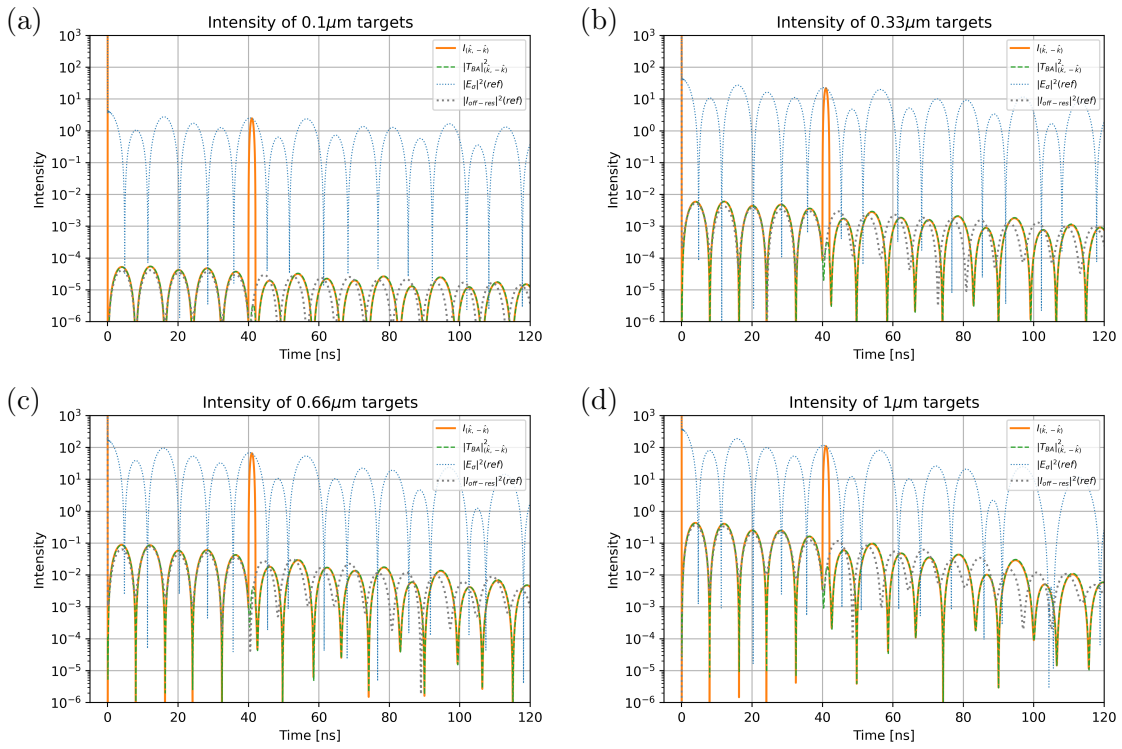

Figure 3.8: (a)-(d) Shaped scattering waveforms into a high contrast pulse at 40ns with various thicknesses. The orange line represents the calculated intensity $I_{\hat{k},-\hat{k}}$ from PYNUSS [81]. The decomposed $|T_{BA}|^2_{\hat{k},-\hat{k}}$(green) supports that the field at each side of the pulse are explained by the radiative coupling field. We approximated the complicate the radiative coupling field into relatively simple equation ($I_{\text{off-res}}$, Eq. (3.53))(grey) that partially explains the radiative coupling field $|T_{\hat{k},-\hat{k}}|^2$(green). The blue line represents the achievable maximum intensity of the pulse for different choice of t_1. (*)The relevant motion can be found in Fig. 3.7(b).

are simple to write. On the other hand, the eight numbers of complicate radiative coupling channels exist for this setting as seen in Eq. (3.46). For $T_1^B T_3^A$ coupling example,

$$
\begin{aligned}
&(T_1^B(t) \otimes T_3^A(t) e^{-ik(\Delta z_{BA}(t) - \Delta z_{BA}(0))}) e^{ik\Delta z_B(t)} e^{-ik\Delta z_B(0)} \\
=&\frac{3}{16} b^2 \Big(\int_0^t \frac{J_1(\sqrt{\frac{3}{2}b(t-\tau)})}{\sqrt{\frac{3}{4}b(t-\tau)}} \frac{J_1(\sqrt{\frac{1}{2}b\tau})}{\sqrt{\frac{1}{4}b\tau}} e^{-i(\omega_3-\omega_1)\tau} e^{-ik(\Delta z_{BA}(\tau) - \Delta z_{BA}(0))} d\tau \Big) \\
&\times e^{-2\gamma t} e^{-i\omega_1 t} e^{ik\Delta z_B(t)} e^{-ik\Delta z_B(0)}
\end{aligned}
$$

Furthermore, the detuning of the coupled transitions are no longer constant when targets' velocities are varying. This makes difficult to apply the approximation for

the radiative coupling field used at Eq. (3.19) or Eq. (3.50) in general motions. It even cannot be considered weak field since the Doppler effect is able to make two transitions back in-resonant condition.

Instead of finding formulas of radiative coupling field, let's denote as the O'(radi. field) for the scattering fields of two moving targets in $\hat{k}$ and $-\hat{k}$ configuration.

$$\begin{aligned} E_{\text{motion}}(t) = \quad & \delta(t)e^{-i\omega_0 t} + \frac{1}{2}T_k(t)(e^{-ik(\Delta z_A(t)-\Delta z_A(0))} + e^{-ik(\Delta z_B(t)-\Delta z_B(0))}) \\ & + O'(\text{radi. field}) \end{aligned} \tag{3.52}$$

with

$$T_k(t) = -\frac{3}{4}b\frac{J_1(\sqrt{2\times\frac{3}{4}bt})}{\sqrt{\frac{3}{4}bt}}e^{-\gamma t}(e^{-i\omega_1 t}+e^{-i\omega_6 t}) - \frac{1}{4}b\frac{J_1(\sqrt{2\times\frac{1}{4}bt})}{\sqrt{\frac{1}{4}bt}}e^{-\gamma t}(e^{-i\omega_3 t}+e^{-i\omega_4 t})$$

But we can make one approximation with given recipe motion Eq. (3.51). It can be found that the $\Delta z_{BA}(t) = \Delta z_B(t) - \Delta z_A(t)$ are kept as $\pm\frac{\lambda}{2}$ for most of time, except the time for the short pulse generation period ($t_1 < t < t_1 + \tau$). This condition sets the detunings for all radiative coupling channels are kept same for long period of time. Based on this we can apply the same approximation as Eq. (3.51).

$$O'(\text{radi. field}) \simeq O(\text{weak radi. field})e^{-ik(\Delta z_B(t)-\Delta z_B(0))}, \tag{3.53}$$

where O(weak radi. field) is defined as off-resonant radiative coupling field for stationary targets.

1st time interval $0 < t < t_1$:
Substituting motions into Eq. (3.52), the weak radiative coupling field becomes the most dominant field in this time period due to constructed interference condition. The scattering field is,

$$E_{1\text{st}}(t) = \delta(t)e^{-i\omega_0 t} + O'(\text{radi. field}), \tag{3.54}$$

The time intensity is

$$\begin{aligned} I_{1\text{st}}(t) &= \delta(t) + |O'(\text{radi. field})|^2 \\ &\simeq \delta(t) + |\kappa_1 \times \frac{3}{4}b\frac{J_1(\sqrt{3bt/2})}{\sqrt{3bt/4}}e^{-\gamma t}(e^{-i\omega_1 t} - e^{-i\omega_6 t}) \\ &\qquad + \kappa_3 \times \frac{b}{4}\frac{J_1(\sqrt{bt/2})}{\sqrt{bt/4}}e^{-\gamma t}(e^{-i\omega_3 t} - e^{-i\omega_4 t})|^2, \end{aligned} \tag{3.55}$$

where $\kappa_1 = -2.55 \times 10^{-3}$ and $\kappa_3 = 4.43 \times 10^{-3}$ are evaluated for the 0.1μm. It increases proportional to the thickness, as seen in Eq. (3.48).

In Fig. 3.8(a)-(d), the time intensity with applied motions and magnetic dipole moment configuration is represented as $I_{\hat{k},-\hat{k}}(t)$ (orange). It displays the synchrotron pulse at $t = 0$ and the suppressed intensity prior to the pulse $t < 40$ns. The green curve($|T_{BA}|^2_{\hat{k},-\hat{k}}$) proves that the radiative coupling field still explains the suppressed time intensity during this time period. Because the radiative coupling field is difficult to calculate, we have made approximation to simply explain the off-resonant scattering field. The grey line is the approximated intensity, Eq. (3.55), not including synchrotron pulse, that shows good agreements with the $I_{\hat{k},-\hat{k}}(t)$ for all targets. According to Eq. (3.55), the suppression is a function of thicknesses as well as the energy differences.

2nd time interval $\mathbf{t_1 < t < t_1 + \tau}$:
The constructed interference condition is broken during this time period in purpose to generate a pulse. Assuming the motionally induced beating is faster than the Quantum beating and Dynamical beating, we can regard the intensity as slowly varying envelope modulated by the rapidly oscillating motionally induced beating.

$$E_{\rm 2nd}(t) \simeq -\underbrace{\{\frac{3}{4}b\frac{J_1(\sqrt{2\times\frac{3}{4}bt})}{\sqrt{\frac{3}{4}bt}}(e^{-i\omega_1 t}+e^{-i\omega_6 t})+\frac{1}{4}b\frac{J_1(\sqrt{2\times\frac{1}{4}bt})}{\sqrt{\frac{1}{4}bt}}(e^{-i\omega_3 t}+e^{-i\omega_4 t})\}e^{-\gamma t}}_{\text{Slower varying envelope}}$$
$$\times e^{i\phi_1/2}(e^{-i(kvt-\phi_1/2)}-e^{i(kvt-\phi_1/2)})+O'(\text{radi. field}) \tag{3.56}$$

where $e^{i\phi_1} = e^{2ikvt_1}$ is a constant phase determined by the choice of t_1 and ϕ_1.

Using the defined T_k in Eq. (3.52) to write down the envelope of singly scattered fields,

$$\begin{aligned} I_{\rm 2nd}(t) = \quad & 4b^2|T_k|^2\sin^2(kvt-\phi_1/2) \\ & + 4bT_k \times O(\text{weak. radi. field}) \times \sin^2(kvt-\phi_1/2) \\ & + |O(\text{weak. radi. field})|^2 \end{aligned} \tag{3.57}$$

where the O(weak radi. field)$e^{-ik(\Delta z_B(t)-\Delta z_B(0))}$ substitutes the O'(radi. field) according to Eq. (3.53)

Following previous disussion, its maximum intensity of pulse is located at $kvt - \phi_1/2 = \pi/2$ or equivalently at $t = t_1 + \tau/2$. Because $\sin^2(kvt-\phi_1/2)|_{t=t_1+\tau} = 1$, the maximum intensity can be represented in terms of the fields of resting taregts, $\simeq |E_\sigma(t) - 2O(\text{weak. radi. field})|^2$. (Eq. (3.50)).

$$\text{Max}\{I_{\rm 2nd}(t)\} \simeq |E_\sigma(t) - 2O(\text{weak radi. field})|^2 \simeq |E_\sigma(t)|^2, \tag{3.58}$$

where the last approximation holds when we don't consider O(weak radi. field) terms, it is further approximated into $|E_\sigma(t)|^2$.

The same condition is required for the motionally induced beating to oscillate once.

$$\tau = \frac{\lambda}{2v} \tag{3.59}$$

Expectedly, a short pulse is produced at the 40ns$< t <$ 42ns in Fig. 3.8(a)-(d). Because the pulse is generated from the beating, its maximum intensity is bound to $|E_\sigma(t)|^2$(blue dot lines) as discussed in Eq. (3.50).

3$^{\mathbf{rd}}$ time interval $\mathbf{t_1 + \tau < t}$

After production of a pulse, the new positions of two targets are back to the favorable condition for the destructive interference. The singly scattered fields interfere if the new motion is applied to the second target.

The radiative coupling channel governs this time intensity measurement.

$$E_{3rd}(t) \simeq O'(\text{radi. coup.})$$

It calculates the time intensity as,

$$\begin{aligned} I_{3\text{rd}}(t) &\simeq |O'(\text{weak radi. field})|^2 \\ &= |\kappa_1 \frac{3}{4} b \frac{J_1(\sqrt{3bt/2})}{\sqrt{3bt/4}} e^{-\gamma t}(e^{-i\omega_1 t} - e^{-i\omega_6 t}) + \kappa_3 \frac{b}{4} \frac{J_1(\sqrt{bt/2})}{\sqrt{bt/4}} e^{-\gamma t}(e^{-i\omega_3 t} - e^{-i\omega_4 t})|^2 \end{aligned} \tag{3.60}$$

Seeing the $I_{\hat{k},-\hat{k}}(t)$, the desirable low-intensity period is created with the motion and polarization depedent scattering at $t > 42$ after the pulse, in Fig. 3.8(a)-(d). When we decompose the $I_{\hat{k},-\hat{k}}(t)$, we can see it is still the radiative coupling field ($|T_{BA}|^2_{\hat{k},-\hat{k}}$)(green) that makes up this time period. However, the approximation of this radiative coupling field (Eq. (3.60))(grey) starts showing deviation from real time intensity (orange). The reason can be found in the temporary created radiative coupling channels during the pulse generation time, 40ns$< t <$ 42ns. Different features are all related to the created different conditions for the radiative coupling scattering channels. First, the approximated calculation(grey) advances by 2ns. It is because the approximation (Eq. (3.53)) keeps radiating during the 40ns$< t <$ 42ns while the real radiative coupling field scatters off with different conditions. During this short time, the different detuning condition assigns different evolution for the coefficients, thereby κ_1 and κ_3 are modified. Despite the rough approximation, the approximation can still be used to explain the magnitude of the radiative coupling field after the pulse because the pulse duration was too short to change the coefficients by a lot.

High intensity contrast pulse and time condition

First, compared to the discussed waveform shaping scheme in the previous Section 3.2, the produced pulse has similar limitations regarding its maximum intensity in Eq. (3.28), Eq. (3.58) and pulse duration in Eq. (3.29), Eq. (3.59). But, the enhanced pulse's contrast is achieved by suppressing the intensity at both sides of the produced pulse. One method to quantify the pulse's contrast is to compare the relative intensity between the intensity of pulse and the intensity at its wings [83]. In our case, it computes to 3.129×10^4, 2.33×10^3, 5.86×10^2, and 1.78×10^2 for 0.1μm, 0.33μm, 0.66μm, 1μm thick targets, where it shows order of 10^1 to 10^3 improvement from the non-hyperfine iron example. It is difficult to select the intensity level for the non-hyperfine iron, therefore the maximum radiative coupling field intensity is assumed for the calculation within $t < 141$ns.

In addition to the enhanced contrast, the $\hat{k}$, -$\hat{k}$ configuration provides each one advantage and one drawback regarding the time condition. The significantly suppressed radiative coupling field for the $\hat{k}$, -$\hat{k}$ configuration enables to produce pulse at a longer time with good intensity contrast. Following the similar arguement in Section 3.2.4, the motion can shape the scattering waveform into short pulses if following condition is met,

$$|O(\text{weak. radi. field})(t)|^2 < |E_\sigma(t) - 2O(\text{weak. radi. field})(t)|^2 \simeq |E_\sigma(t)|^2,$$

where the last inequation assumes $O(\text{weak. radi. field}) << E_\sigma(t)$. Because the coefficients κ_1, κ_3 are enough small, the inequation puts no effective restriction regarding the delay time. The inequation holds for longer than 1000ns for all examined targets.

On the other hand, the existing Quantum and Dynamical beating imposes condition for the choice of the delay time. As read in Eq. (3.57), if the chosen delay t_1 makes amplitude (T_k) zero, the generated pulse $I_{2\text{nd}}(t)$ cannot have high intensity. This condition decides that t_1 cannot be chosen at 4.7ns, 12.53ns, 20.45ns, and $\cdots$ for the all targets. Most of zeros are irrelevant to the thickness because it is the Quantum beating related to $(e^{-i\omega_1 t} + e^{-i\omega_6 t})$ term that oscillates at fastest speed.

Chapter 4

Characterization of the electronic response of the piezo transducers

In this chapter, the electronic response function of the electronics and piezo transducer will be discussed as a part of motion system charcterization.

First, we will introduce part of synchrotron experiments to explain the used electronic set-ups. The electronics has been built for the past beamtime to test the peizo transducer. We need to understand its arrangement because it is related to the obtained raw data. The specific information of the electroncis will be also presented together during the introduction. At Section 4.2, we will discuss the data process to get response function of the system from the raw data. Averaging, choosing the 768ns data, threshold for the response function calculateion, time-jitter elimination will be discussed in order. With the processed response functions, the analysis on the system will be followed at the end of this project.

Brief on motion system

The real motion of Mössbauer target in experiment doesn't exactly follow the desired profile because of the motion units' imperfect/non-linear response [54, 55]. To diagnose the problem in the experiment, first, we need to understand that the motion system is composed of largely two parts. The first part is the piezoelectric crystal which expands as a response of an induced electric field [84, 85]. The next part is the Mössbauer nuclei from where the scattered fields are radiated out. The motion of Mössbauer nuclei is achieved in a way that piezoelectric crystal experiences a lattice deformation. Later, crystal's mechanical deformation transfer the motion to the Mössbauer nuclei which are mounted on the top of the piezo transducer. This way promises the control of displacement in wavelength order [49, 53].

The principle gives us natural separation for the research, the electronic response of the piezoelectric transducer, and the mechanical response of the both piezoelectric transducer and Mössbauer nuclei. The electronic response includes the accumulation of charge on the lattice as a response of the external voltage source. While the mechanical response of the target is more complicates that it includes the lattice deformation of the piezo transducer and the delivery of motions to the Mössbauer target from the lattice deformation. The characterization of mechanical response of the system requires us to measure the position of the targets in Ångstrom meter precision. It can currently only be achievable at synchrotrons or XFELs [54, 82]. However, the electronic response of the piezo transducer can be easily prepared and

studied in the laboratory with electronics [54].

4.1 Experimental components

Our measurement set-up has already been set-up to give a test before beamtimes over the last years [54]. In this reason, it is designed to resemble the data acquisition environment in the synchrotron experiment. Before describing the design of the electronics in our laboratory, first, the brief set-up of the synchrotron experiment will be introduced.

4.1.1 Synchrotron experiment

Mentioning all details of the synchrotron would be out of scope of this thesis, instead, describing the relevant parts may provide enough information to understand our electronic set-up [30, 54, 57, 82].

Photon

Synchrotron radiation is a tool of an excellent light source from far-infrared to hard X-ray regimes. The synchrotron radiation is achieved when a bunch of electrons experiences transverse acceleration. The property of the electron bunch determines many of produced pulse's properties. For example, its time duration ($\simeq$ 100 ps) is set by the electron's bunch length (44 psec at PETRA III). And the energy of the generated light (near 14.4keV for ^{57}Fe Mössbauer scattering) is determined by the speed of the electrons. Many of the synchrotron stores several electron bunches in the storage ring, where two electron bunches are timely separated by 8 ns (960 bunches) to 192 ns (40 bunches) for PETRA III [30].

Therefore a target is bombarded by the timely narrow pulses every 192ns. However, the limitation of synchrotron radiation brilliance produces less than one resonant photon on average for each pulses at hard X-ray regime. This environment sets the detector to measure at most one scattered photon between two synchrotron pulses.

The stored electron bunches offer a master clock for all electronics in the synchrotron experiment, called **bunch clock** [30]. When each electron bunch passes an installed module inside the storage ring, the induced electricity is generated that informs the time and spatial information of each electron bunch. Based on this information, it is possible to trace the pulse arrival time for the targets and detectors.

Mössbauer target

The mechanical motion system is of special interest to understanding our electronic set-up. First, the input voltage signal is synchronized with the pulse arrival time by the bunch clock. So that desired phase control can be implied properly. The experiment sets one sequence of measurement to take 4×192ns, so four pulses can arrive meantime. One trace of the motion usually consists of four sub-motions:

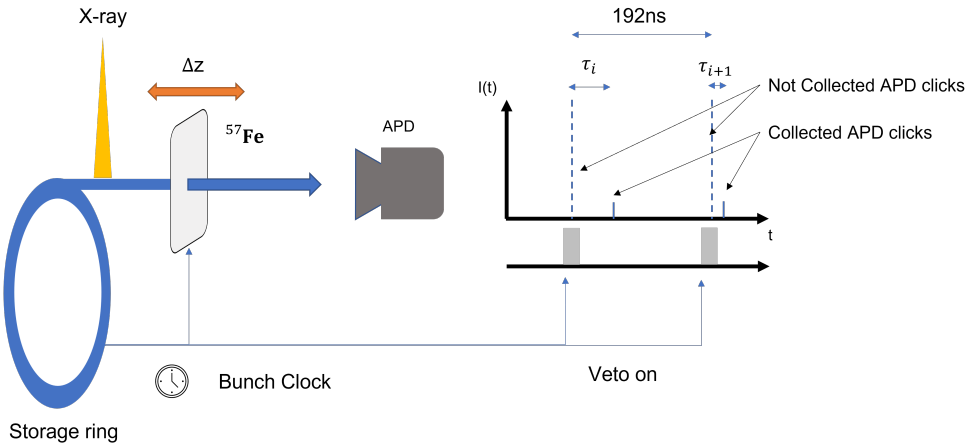

Figure 4.1: The figure captures the principle of the detection scheme of scattered fields in the synchrotron experiment with the APD. All electronics are synchronized to the bunch clock.

first pulse + a displacement (192ns) → second pulse +target at rest (386ns) → third pulse + another displacement (576ns)→ and the last pulse + second stationary phase (768ns) [82]. In this way, we can measure the effect of motion at first and third pulses while the second and fourth measurement will function as reference measurements for the fluctuating synchrotron's intensity [54, 55]. Besides, the motion is designed in a way that it returns the Mössbauer target at fixed starting point for every 768ns.

Detector

The Avalanche Photodiode Detector (APD) is employed to measure the photon arrival times. The APD also needs a bunch clock to run the APD in veto mode because the measurement of a pulse can saturate the APD up to about 15ns [30, 57]. When the APD runs in veto mode, the Data Acquisition stops collecting photon count so that photons of the synchrotron pulses are ignored and only the photons from the ^{57}Fe are collected. Lastly, considering the low number of the resonant photons at the hard X-ray regime, the experiment needs to take numerous repetitions to construct the time spectrum.

4.1.2 Electronics

The studies of the electronic response of piezo don't necessarily require X-ray photon sources. Instead, we can produce **a fake APD clicks** which will trigger the Data Acquisition and start collecting a trace of the voltage signal that contains the response of piezo about the given input.

The virtual synchrotron environment set-up requires 5 electronics.

- Function generator, Agilent 81160A
- Delay Unit, Stanford Research Systems DG645

- Quadra Constant Fraction Discriminator (Quad CFD), Tennelec TC454
- Data Acquisition System(DAQ), Roentdek
- Piezo transducer, with PVDF element by Measurement Specialities Inc

The electronic set-up is presented in Fig. 4.2(a) and its details will be introduced in the following.

Function generator

The Function generator locates at the top of the shelf, in the left top corner in Fig. 4.2(a). Two independent voltage patterns can be outlet from the Function generator (Agilent 81160A) which are synched with internal frequency divider. The Agilent 81160A can provide good signal sampling rates (2.5GSa/sec) and an internal speed when it runs in arbitral-function-generation mode [86] for both channels. Moreover, the Agilent has an internal impedance of 50Ω and transition times of 1ns. The first voltage signal is used to measure the electronic response of the system for our purpose, but its role in the synchrotron can be found as motion inducement. Since the motion of Mössbauer targets repeats for every 4 pulses in the synchrotron experiment, the generated voltage pattern also repeats for every 4×192ns, 1.25MHz rate.

The purpose of the second voltage signal is to produce a raw "fake APD signal" which will onset the data acquisition process. A box-shape voltage is chosen to trigger the next electronics, the Delay unit. The produced box-shape voltage contains rising/falling time of 1ns with amplitude of $1.4V_{pp}$ and 10ns width. The voltage is produced with inverted polarity.

	Ch1	Ch2
Purpose:	to induce motions	to generate fake APD
Repetition rate:	every 768ns	every 196μs
Voltage signal:	Designed functions (see Section 4.2.3)	box-shape (details in text)

Table 4.1: Specifications of generated signals in Agilent 81160A

Delay unit

The Delay unit receives a box-shape voltage from the Function generator via BNC cable, placed above the Function generator in Fig. 4.2(a). The internal impedance of the Delay unit, Function generator, and BNC cable are matched to 50Ω to avoid reflections at each terminal. The Delay unit produces a precisely defined pulse with good timing and low time-jitter which will be used as the fake APD signals [87]. The Delay unit is set to external trigger mode at the falling edge of the input voltage with trigger level of 750mV. Once the Delay unit is triggered, the inputs will be neglected for 600μs. Meantime it produces a fast inverted pulse with 20ns duration, which is one electronic standard named after its developer, Nuclear Instrumentation Module

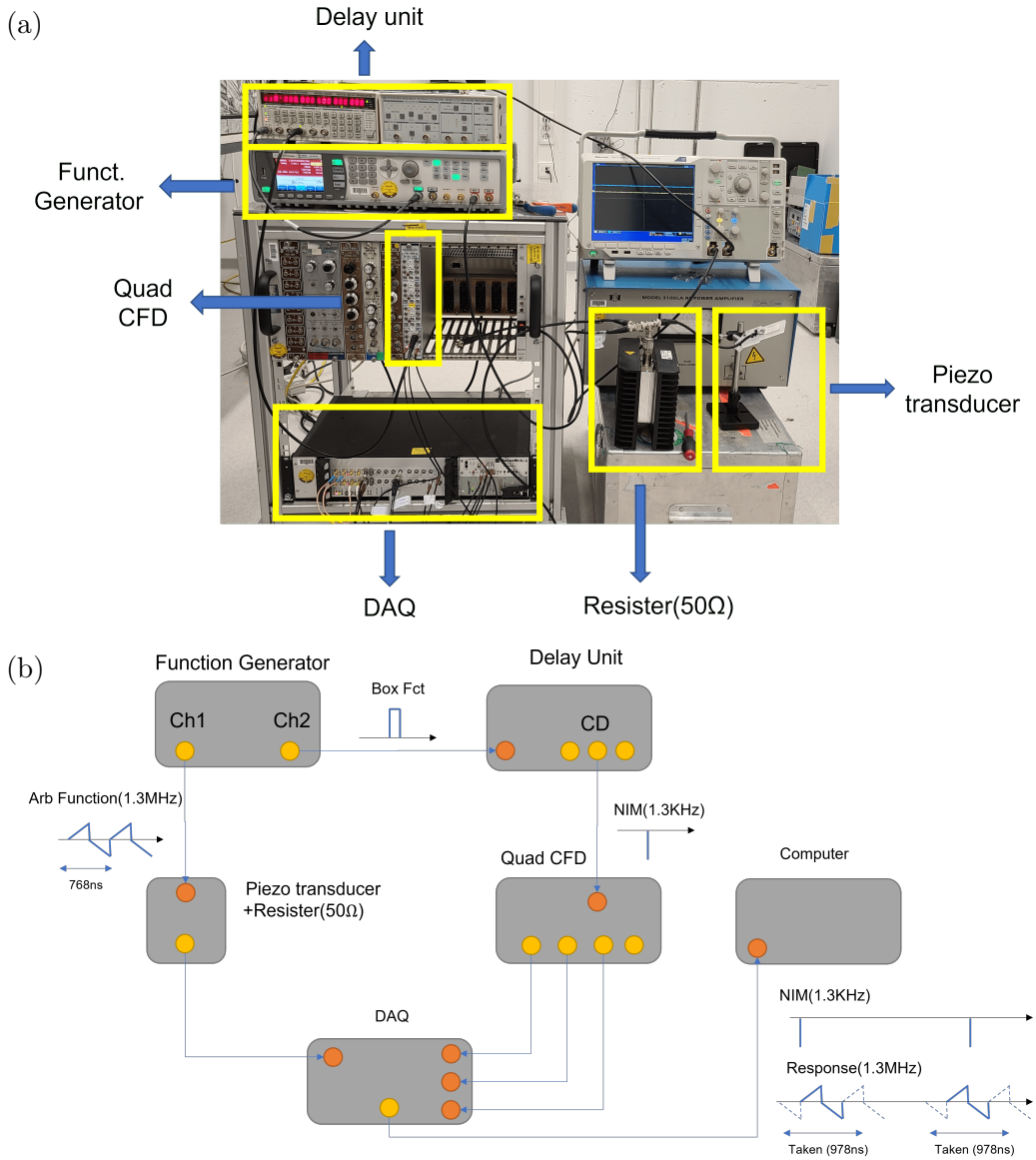

Figure 4.2: (a)The actual electronic set-up. Each electronic device is marked with a yellow box in the photo and is labeled outside the figure. (b) The above electronic set-up is presented in a schematic diagram. (Yellow circles refer the outputs of the system and orange circles indicate the inputs for the system) The installed piezo reacts to the one trace of voltage (768ns). The responsed voltage signal flows into the DAQ. Another voltage is sent to the Delay unit to be converted into the fake APD signal. With a successful generation of fake APD signals (NIM pulse), it triggers the DAQ at a 1.67kHz rate after passing Quad CFD. The triggered DAQ collects the voltage signals from the piezo during the 978ns, which is longer than one trace time.

(NIM). The usage of the Delay unit can be found its precise timing. The Function generator Agilent produces the signal with frequency divider, which is not greater than 255. On the other hand, the produced NIM signal is precisely determined with the Delay unit [54].

- Trigger mode: External trigger at falling edges
- Output: NIM (CD channel w/ 600 μs, and 20ns for stable operation)

It is important to point the chosen delay parameters are not related to the property of the APD. Rather, the APD installed in the PETRA III can resolute less than a couple of nanoseconds [88]. The 600μs rate and 20ns width are chosen because of its stable functioning.

Quad CFD

The NIM pulse flows into the QUAD CFD box, located on the shelf (left) in Fig. 4.2(a), which copies the input signal (fake APD clicks) into four equivalent outputs. Three of outputs enter the DAQ unit for triggerings.

Piezo transducer

Another voltage pattern is transmitted to the piezo transducer from a different channel of the Agillent 81160A, right bottom in Fig. 4.2(a). Considering the internal impedance of the Function generator, the same impedance of the BNC cable is used and the 50Ω resister is added at another termination of the BNC cable for the best signal transmission to the piezotransducer. The charges are stacked on one side of the crystal as a response of the timely varying input voltage.

The used piezo element is a thin polyvinylidene fluoride piezoelectric transducer(PVDF) manufactured by Measurement Specialities Inc [89]. Each PVDF is glued onto a 4mm thick acrylic glass plate with two-part epoxy glue to reduce the vibrations [82]. To understand the electronic response of each piezo by thickness, three different piezo transducers are examined in this project. Labels (4) and (6) distinguish two same thickness of piezo transducers.

- Model: DT1-028K (4) (thickeness: 28μm)
- Model: DT1-028K (6) (thickeness: 28μm)
- Model: DT1-052K (thickeness: 52μm)

Data Acquisition System Both the response of the piezo and the fake APD signal flow into the DAQ unit. The DAQ is triggered when the fake APD signal arrives and starts storing the arrived voltage traces over 978ns [90]. The DAQ digitizes the arriving voltage traces every 0.8ns and resolutes the voltage values with 10 bit resolution (details in Section 4.3.3). Besides, the DAQ cannot resolute two photon clicks if they are too timley close in the synchrotron experiment. In this reason the Delay unit is also desired to avoid the occuring errors in DAQ [54].

4.2 Response function

4.2.1 Definition

The response function is defined as a ratio of the output function and input function of a given system in the frequency domain. The response function is used to understand the response of the linear system or subsystem for given inputs [91, 92]. The system needs to respond linearly for characaterization by response function, otherwise, the analysis on frequency domain lost the meanings and we need to study the system in time domain, instead.

The responsed output voltage is represented as the multiplication of the system's response function and input voltage. From this,

$$H_{\mathrm{sys}}(\omega) = \frac{V_{\mathrm{sys}}(\omega)}{V_{\mathrm{input}}(\omega)}$$

In this study, the response function will be defined as the ratio between the measured voltage after one electronic set-up and one ideal input voltage. The electronic set-up varies in choice of piezo tranceducer. If no piezo transducer is applied, calculated $H_{\mathrm{el}}(\omega)$ contains response of electronics, only. Depending on the type of installed piezo transducer, the $H_{\mathrm{pz+el}}$ can contain the combined transfer of the piezo transducer and the electric components including the resister, BNC cable, etc.

$$\begin{cases} H_{\mathrm{pz+el}}(\omega) = \frac{V_{\mathrm{piezo+elec}}(\omega)}{V_{\mathrm{input}}(\omega)} \\ H_{\mathrm{el}}(\omega) = \frac{V_{\mathrm{elec}}(\omega)}{V_{\mathrm{input}}(\omega)} \end{cases} \tag{4.1}$$

The above definition is decided for this study because $V_{\mathrm{input}}(\omega)$ doesn't contain any error and it is the combined response that we aim to characterize to understand for future synchrotron experiments.

4.2.2 Conventional characterization method

The conventional characterization method of the response function uses a lot of single sinusoidal functions to probe the system's response one frequency by one frequency [92, 93]. The entire response function of the system is constructed by repeating the measurements. Although this method provides a concrete method for characterization, it takes too long times and many repetitions to fully understand one single piezo considering the frequency range in interest.

4.2.3 Employed characterization method

Our approach and used method in synchrotron experiment employ (analytic) functions as an input voltage, instead [54]. Chosen functions are composed of a wide range of frequency bands. By measuring the system's response with the function,

we can measure a wide range of response function at once. As known from the Fourier transformation, a timely narrow function has a corresponding Fourier transformed function defined in broad frequency ranges. Another type of function we can choose is the functions defined with a discontinuous point, such as the Heaviside function. In these fashions, following several functions are chosen to test the response functions of the system. The examples of employed functions (orange) are given in Fig. 4.3(a)-(d), Gaussian with 8ns FWHM, DESY Ramp function, two Rectangular and Exponential functions. The relevant measurement data (blue) are plotted together with its input signal to display the response of the piezo transducer and electronics. However, the measured voltage signal requires few processes to be understood. The data processes and plots will be discussed at Section 4.3.2 and will give short explaintion at there.

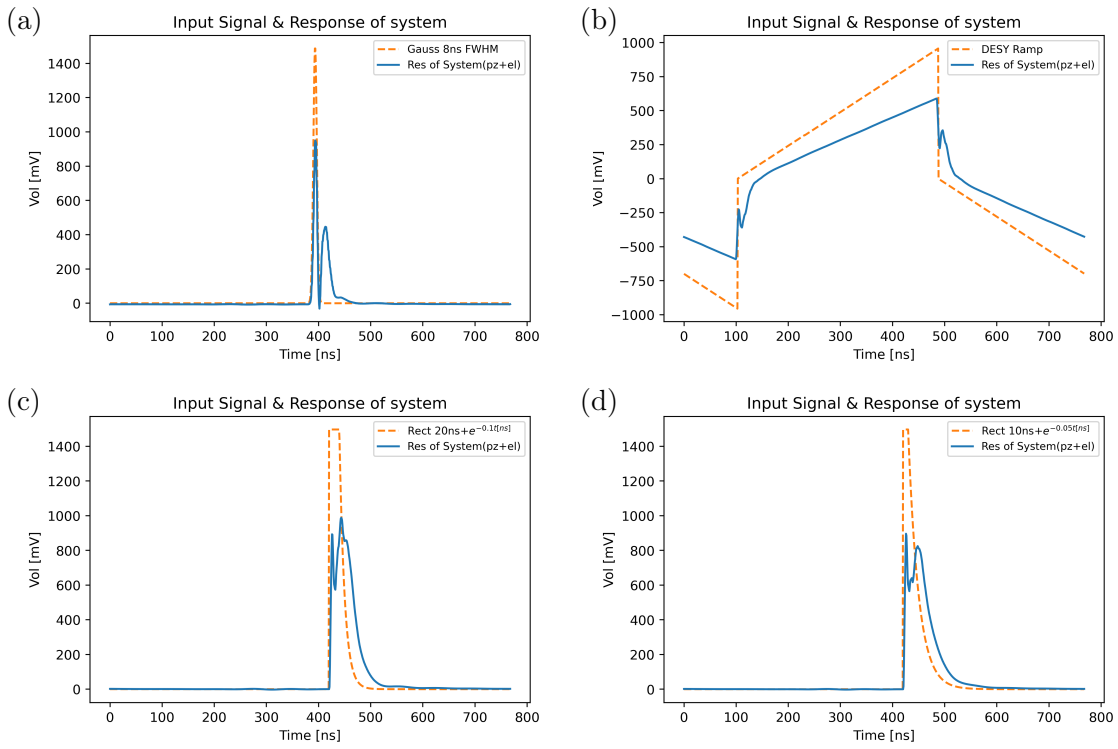

Figure 4.3: (a)-(d) The examples of input voltage signal (in broken orange) and averaged response of the piezo transducer (in solid blue) are plotted: Gaussian function with 8ns FWHM, DESY Ramp function, Rectangular function + Exponential decay functions. The Rectangular function has 20ns or 10ns of width. The Exponential, $e^{-\gamma t}$, has decay coefficients $\gamma = 0.1$, and 0.05GHz. To convert from the raw data to the proper voltage responses (blue), it requires averaging, tailoring, calibration measurement. The responsed voltage shares common properties: attenuated voltage, long response time of the system, phase retard at rising edges. However, it is difficult to extract meaningful data from the time domain.

Gaussian function

Well-known analytic functions (Gaussian, Sinc, etc) are tested at the early measurements with several parameters. The Gaussian is specifically chosen because its Fourier transformed function is also Gaussian function and it was expected to probe a broad frequency range at once.

$$V(t) = e^{-\frac{1}{2}\frac{(t-\mu)^2}{\sigma^2}} \tag{4.2}$$

Corresponding transformed function is,

$$V(\omega) = \sigma\sqrt{2\pi}e^{-\frac{1}{2}\omega^2\sigma^2} \tag{4.3}$$

The chosen parameter, $\sigma_{\mathrm{t}} = 3.39$ns from 8ns FWHM, is equivalent to the $\sigma_\omega = 295$MHz and it is expected to provide responses of piezo transducer and electronics over broad frequency at once.

DESY ramp function

The DESY Ramp function is a type of function tested to understand the suspicious charge losses in the static targets in past beamtime. The function is composed of two slow ramp functions with opposite gradients so that it can compensate the charge losses [54].

The DESY Ramp function has chosen because we thought its discontinuous point and slowly increasing/decreasing slopes will offer a good test for the electronic response of the piezo transducer.

The DESY Ramp function is represented as

$$V(t) = v_0 t \times \theta(t) - 2v_0 t \times \theta(t - \mathrm{T}/2) + v_0 t \times \theta(t - \mathrm{T}), \tag{4.4}$$

where T is 768ns and $v_0 = \frac{990}{384}[\frac{\mathrm{mV}}{\mathrm{ns}}]$.

The corresponding function in frequency is,

$$\begin{aligned} V(\omega) &= -\frac{v_0}{\omega^2} \times (1 - 2e^{-i\omega\frac{\mathrm{T}}{2}} + e^{-i\omega\mathrm{T}}) - \frac{v_0}{4}T^2 \times \mathrm{sinc}(\frac{\omega\mathrm{T}}{4})e^{-i\omega\frac{3}{4}\mathrm{T}} \\ &= -\frac{v_0}{\omega^2} \times (2 - 2e^{-in\pi}) - \frac{v_0}{4}T^2 \times \mathrm{sinc}(\frac{n\pi}{2})e^{-i\frac{3}{2}n\pi}, \end{aligned} \tag{4.5}$$

where the last equation uses the property of the Fast Fourier Transformation, $\omega = \frac{2n\pi}{\mathrm{T}}$. Despite of its repeating zeros for every even n, the DESY Ramp function allows us to investigate the broad range. To answer how broad range we can measure with this function, we need to understand when the component of signal ($V(\omega)$) gets smaller than components of the noise. It is difficult to expect the probable frequency range with the formula and current measurement data, however, it allows us to measure the response of the system by 400 MHz range.

Rectangular + Exponential decay functions

Although it were able to get a wide range of frequency components with the DESY Ramp function, more cases are needed to verify the obtained response function. Because we have supposed that the measured data is carrying non-linear response of the piezo transducer and the electronics.

To double-check the linear responses, we bring a type of functons which is composed of Rectangular function + Exponential decay. We assume that the same non-linear response will appear for the Rectangular function because it is the same the Heaviside function mathematically. The various width (10ns or 20ns) of the Rectangular function and the different decay speed (0.1 or 0.05 GHz) of Exponentials are chosen for the purpose.

The functions can be represented as,

$$V(t) = \mathrm{V}_0 \times (\theta(t) - \theta(t - t_1)) + \mathrm{V}_0 e^{-\gamma t} \times \theta(t - t_1), \tag{4.6}$$

where t_1 is a variable of the width of the Rectangular function (5 or 10ns) and the γ determines the decay speed of the Exponential function (0.1 or 0.05 GHz) next to the Rectangular function, and V_0 is a height of the Rectangular function which is fixed to 1.5V.

The corresponding function in frequency space is,

$$V(\omega) = \mathrm{V}_0 \times (\frac{e^{-\gamma t_1}}{\gamma + i\omega} e^{-i\omega t_1} + \frac{1}{i\omega}(1 - e^{-i\omega t_1})), \tag{4.7}$$

which offers a way to characterize a broad frequency range at once. It is also difficult to predict the available frequency range, but this function also provides the response function by 400MHz.

4.3 Measurement and Data process

The measurement collects the voltage traces that contains information about the responses of the systems as a function of given input voltage. The measurements are also conducted with varying type of piezo transducers. We aim to extract the response of the piezo transducer and relevant electronics in the frequency space. However, the acquired data is the voltage traces in time which contains both signals and errors, including the time-jitter (different time-zeros for each data, the details will be discussed in Section 4.3.5), thermal nosie as well as the systemical errors. The collected data needs few processes before being calculated to the response function. The schematic diagram plots the required data process, in Fig. 4.4. Each section will discuss about each steps of the diagram

4.3.1 Statistic

To run proper statistics, in total 150,000 to 200,000 voltage traces are collected for each measurement. By calculating deviations of total traces of one measurement,

it is possible to check raw data before running the statistics. Even though it rarely takes place, one over several hundreds of thousands of raw data, the raw data is excluded if the wrong voltage trace is saved for a better statistical process. After running the averaging the data, it is expected to reduce some random noises such as thermal noise. However, the averaged data still contains time-jitter and systemical errors. Despite the measured traces have respective time-zeros, we will average the data first and will eliminate this time-jitter in Section 4.3.5.

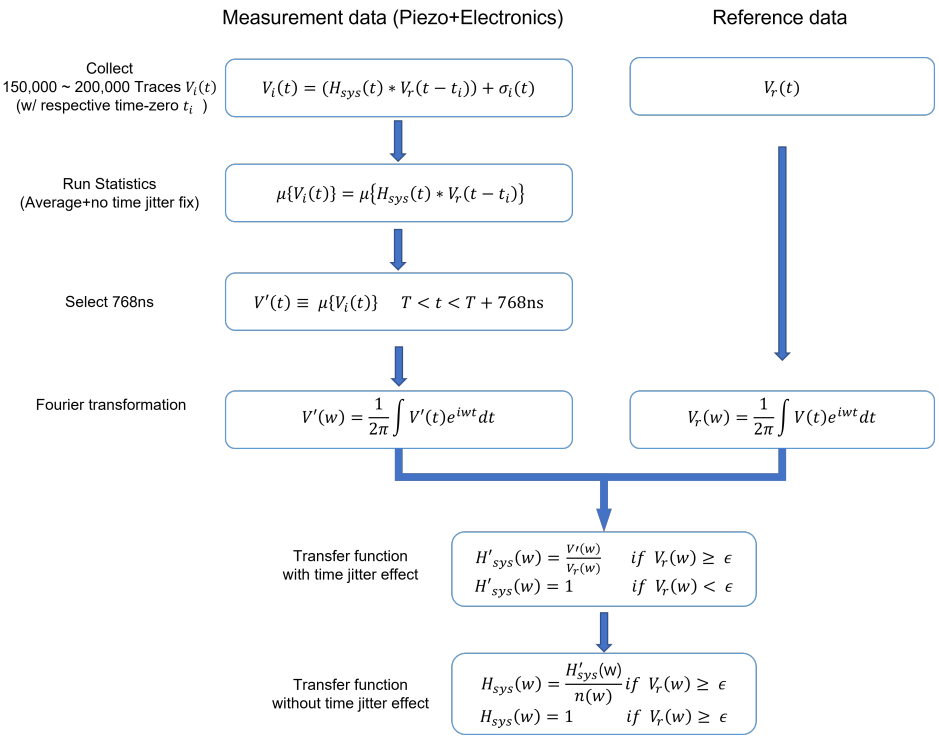

Figure 4.4: The diagram describes the data process to calculate a response function. The raw data will be processed as followed order: Averaging, time selection, fourier transformation, response function calculation, time-jitter elimination

4.3.2 Time trace selection

The 968ns long averaged traces are needed to be tailored into 768ns for the Fourier transformation. Because it is 768ns that system's response repeats, not 968ns. We can simply obtain the 768ns length of data for most of the averaged voltage traces by choosing the proper part of the data. It is important to cut irrelevant part of the averaged voltage and chosen data to contain all characteristic points, for example, the rising (falling) edges, curves, etc.

4.3.3 Calibration measurement

When the responsed voltage enters the DAQ after interactions, the DAQ digitizes the voltage traces into 1024 pixels [90]. It is required to understand the internal calibration of the DAQ to represent the stored data into voltage correctly. For this reason, an additional calibration measurement is performed to understand the internal conversion ratio.

For this purpose, we directly connected the Function generator to the DAQ system without any other electronics and generated a slow sine function, with period of 192ns, at the Function generator to minimize signal attenuation via installed electronics. The amplitude is chosen to $V_{\text{amp}} = 1.5\text{V}$ because we suspected that the DAQ has $\pm 1\text{V}$ acceptance range. And we know that the installed DAQ resolute the measured voltage in 1024 pixels (10bit resolution) from the data and manual book [90]. It enables us to trace the total voltage range from the measured maximum and minimum of the sine function. The produced amplitude of the sine function is stored as ± 374 pixels in the DAQ. Therefore, we conclude that the DAQ can receive $\pm 2V$ signals with 10bit points.

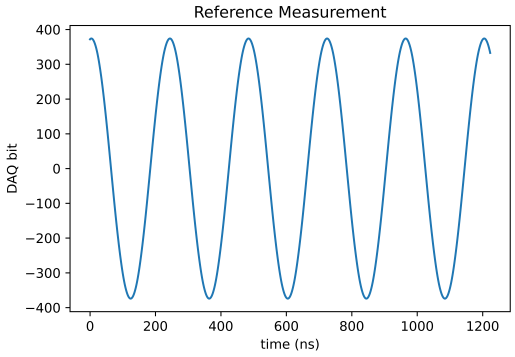

Figure 4.5: This figure shows the raw data of calibration measurement. The sine function oscillating every 192 ns with maximum/minimum at ± 374 pixels is used for the calibration. It verifies that the installed DAQ system converts 1.5 V_{amp} to 374 pixels. The calibration measurement concludes that the DAQ has ± 2V band with 10-bit resolution.

Now, we can discuss about the second curves in Fig. 4.3(a)-(d). The blue curves represent the measured voltage traces after having statistics, trace selection which is converted into Voltage after the calibration. The measured voltage traces are manually shifted to locate near the input function to give an easy observation. It is difficult to extract meaningful information from the time trace, except few trivial information: attenuated voltage, slowly responing system as well as phase retard at rising edges. This motivates us to investigate the system in the frequency domain with the response function.

4.3.4 Raw response function

With tailored traces, the conversion ratio of the DAQ, and the input signal, everything is prepared to calculate the response functions with Eq. (4.1).

Because the raw response function is not a final product for the study, let's focus on the how those functions are calculated. In Eq. (4.1), we used the ideal input function to calculate the response functions to minimize the effect of errors. Despite we carefully choose input functions that are composed of broad range of frequency components, there is certain point since where the component of error is larger than the component of function. Not to contain such region in the calculated response function, the threshold is introduced for the calculation. Normally 10^{-5} is chosen for other response functions. But, the threshold of the response functions of the Gaussian input is set to 10^{-4} because of quantization errors.

Considering the Function generator produces the voltage at speed of 2.5GSa/sec, the Gaussian with FHWM 8ns is consist of 17 samplings for the $\pm\sigma_t$. We suspect insufficient number of samples cause a **quantization error**. The small number of sampling points causes the produced voltage to deviate from the real Gaussian function. If this quantization error assigns non-zero values for the high frequency components, it can cause zero-division errors because the real values approaches to zero at this ranges. The threshold value is chosen to exclude this potential zero-division errors starting after 150MHz and restricts the available frequency range. Although it turns out that the timely narrow functions are not a good option for the characterization method, still its response functions are consistent with the other figures within 150MHz.

The calculated raw response functions are presented in Fig. 4.6(a)-(f). Each figure contains the response of different piezo transducer + electronics (dashed lines) with various input voltages functions. The figures include the response function of pure electronics (blue), which is a measured response function after uninstalling piezo transducer. Especially, we can find the limited frequency ranges for the Gaussian input. The response function of DESY Ramp shows only one data point for every two points. Discussed in Eq. (4.5), the transformed voltage has repeating zeros for every even n. The Fig. 4.6(c) contains an unexpected measurement result at the pure electronic response. We suspect unknown-error took place on this measurement. If it is the real response of the system, the similar effects should be observed at the response functions of combined system, $H_{\mathrm{pz+el}}$ represented in colored lines.

4.3.5 Time-jitter elimination

All response functions in Fig. 4.6 show severe damping over the entire frequency range. The reason of the damping can be found at the time-jittered voltage traces which were survived after the statistics. The measured each raw voltage traces has had respective time-zero, so that one data looks like being translated to the another data as shown in Fig. 4.7(a). We determined the time-jitter at the characteristic

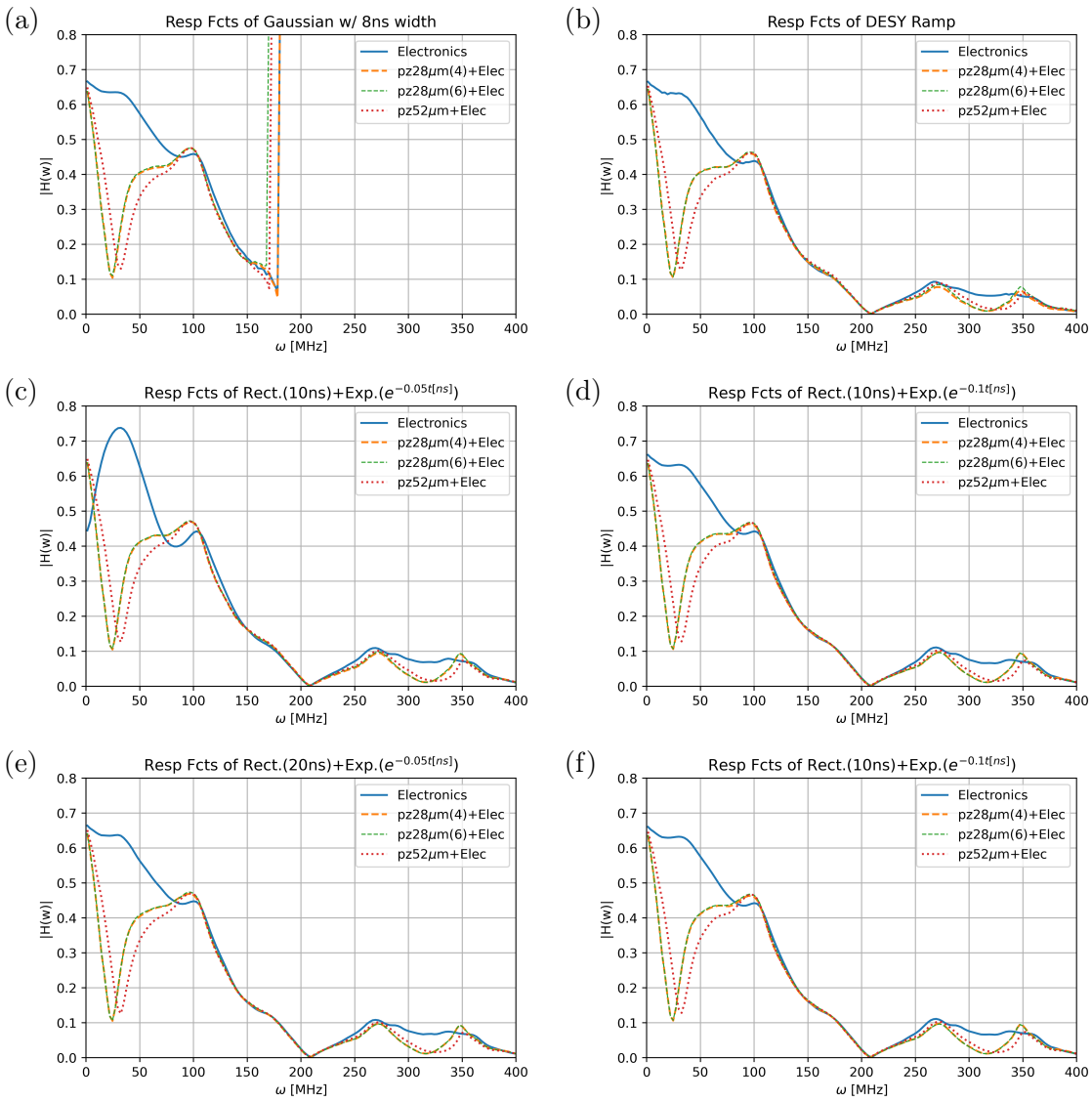

Figure 4.6: (a)-(f) The raw response functions as a function of different piezo transducers and different voltage signal inputs. The Gaussian response function is severely limited because of quantization error. The Fig. 4.6(c) contains an unexpected measurement error at pure electronic response function. The raw response functions contains the time-jitter effect that is featured as the modulation over whole frequency and zeros at near 200MHz. The strong time-jitter effect will be deconvoluted in Section 4.3.5.

point of the raw data (voltage traces). The maximum point is chosen for most of the raw data after assuming the maximum point is real response of the system.

The Fig. 4.7(a) displays randomly chosen 5 raw traces with 28μm thick piezo transducer and Rectangular+Exp input. The histogram of maximum position of entire voltage traces is presented in next subplot. As seen, maximum positions are nearly equally distributed between 503.2ns and 508ns. Indirectly, the agreeing time jitter is observed at the voltage functions produced at the Function generator with the oscilloscope. In this reason, we suspect the time jitter is originated from the produced input voltage, rather than other electronics we employed.

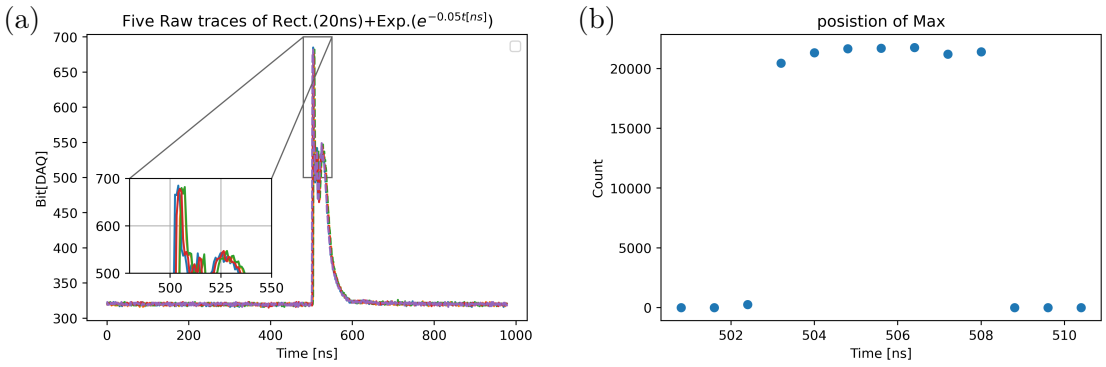

Figure 4.7: (a)Plot of ramdomly chosen 5 raw data to show the error density function. The raw data is composed of 968ns, and represented in bit. (b) Histogram of the maximum position of the same raw traces for entire set of measurements. The raw trace is digitized by every 0.8ns. Maximum points only locate between 503.2ns and 508ns (7 dots with more than 20,000 counts), if we neglect 17 counts and 1 count at 502.4 and 508.8ns time bins.

Then let's fomulize the effect of the time jitter. When one voltage signal finally flows into the DAQ after interactions, it is delayed by t_0 compare to the input voltage due to response as well as transmissions, which both can be treated as signal. But real data doesn't have consistent t_0 for all traces. Instead, each trace has jittered time-zero $t_i = t_0 + \Delta t_i$ around true time-zero t_0.

As mentioned, averaging cannot solve the time-jitter errors. We will define $V'(t)$ as $\mu(V_i(t))$ to represent that it still contains the effect of time jitter.

$$\mu(V_i(t)) = V'(t) = \frac{1}{N}\sum_{i=0}^{N}\{V_i(t - t_i) + \sigma_i(t)\}$$

There might be the voltage traces sharing the same jittered time-zeros. Such traces are defined as $V(t - t_0 - \Delta t_i)$ with the jittered-time zero as $t_0 + \Delta t_i$. We can count how many traces are having the $t_0 + \Delta t_i$ as time-zero. The $n(\Delta t_i)$ is density function of error which is defined with above information after being divided by the

total sample number N.

$$V'(t) = \sum_{\Delta t_i=-\infty}^{\infty} n(\Delta t_i)V(t - t_0 - \Delta t_i) + 0$$
$$\simeq \int_{-\infty}^{\infty} n(\Delta t_i)V(t - t_0 - \Delta t_i)d\Delta t_i = n(t) \otimes V(t - t_0), \tag{4.8}$$

where the discreted convolution equation approximated into continuous convolution after assuming a large number of measurements and continuous time jitter assumption which is centered at 0, so that $\mu(\Delta t_i) = 0$.

The influence of time jitter is represented as a convolution of true signal $V(t-t_0)$ with the error density function. As shown, the $n(t)$ of the our system is measured by counting the maximum point for one input functions. The result is that $n(t)$ is a uniform distribution with 4.8ns wide, in Fig. 4.7(b).

When the two producted functions are Fourier transformed,

$$V'(\omega) = n(\omega)V(\omega), \tag{4.9}$$

where the corresponding $n(\omega)$ is defined as $\mathrm{Sinc}(\frac{\omega}{208[\mathrm{MHz}]})$. It describes that the time-jitter modulates the original signal function $V(\omega)$ by the Sinc function determined by the Fourier transformation of error density function $n(t)$.

Then the true signal can be simply obtained as,

$$V(\omega) = V'(\omega)/n(\omega) \tag{4.10}$$

The effect of time jitter can be eliminated from the already-calculated raw response functions in the same method.

$$H_{\text{no jitter}}(\omega) = H_{\text{raw}}(\omega)/n(\omega) \tag{4.11}$$

The time-jitter free response function are presented in Fig. 4.8(a)-(f) with varying different piezo transducers and input functions. Each subplot contains responses of the system (piezo transducers+electronics) in broken lines and a pure electronic response function in blue. After getting rid of the time-jitter effect, the most features are remained same for the calculated response function. First, we checked the response function of Gaussian inputs are still severly restricted by the quantization errors, though computed response functions are in good agreement with the other input functions within the computable range, in Fig. 4.8(a). Moving to the general feautres, we can observe the strong piezo transducers' response at near 25MHz while no response is observed for the electronics at this frequency ranges (blue). The response functions of two 28μm piezo transducers are nearly consistent over most of the frequency range for all inputs voltage. The piezo transducer with 52μm absorbs higher frequency than the 28μm piezo transducers does. The piezo transducers rarely respond to the frequencies faster than the 120MHz therefore it is the response of electronics (blue) that determines the response of the system at this

regime. Because, the raw response function are divided by the Sinc function (time jitter error density function), significant deviations are observed at near 208MHz frequency. The second responses of piezo transducers are observed at the higher frequency regime near 300MHz. It requires additional measurement to understand the origins of this features. Lastly, it is difficult to answer the origin of overall 40MHz oscillation with current data except it is irrelevant to the piezo transducer because the response function without piezo transducer(blue) already shows the same feature.

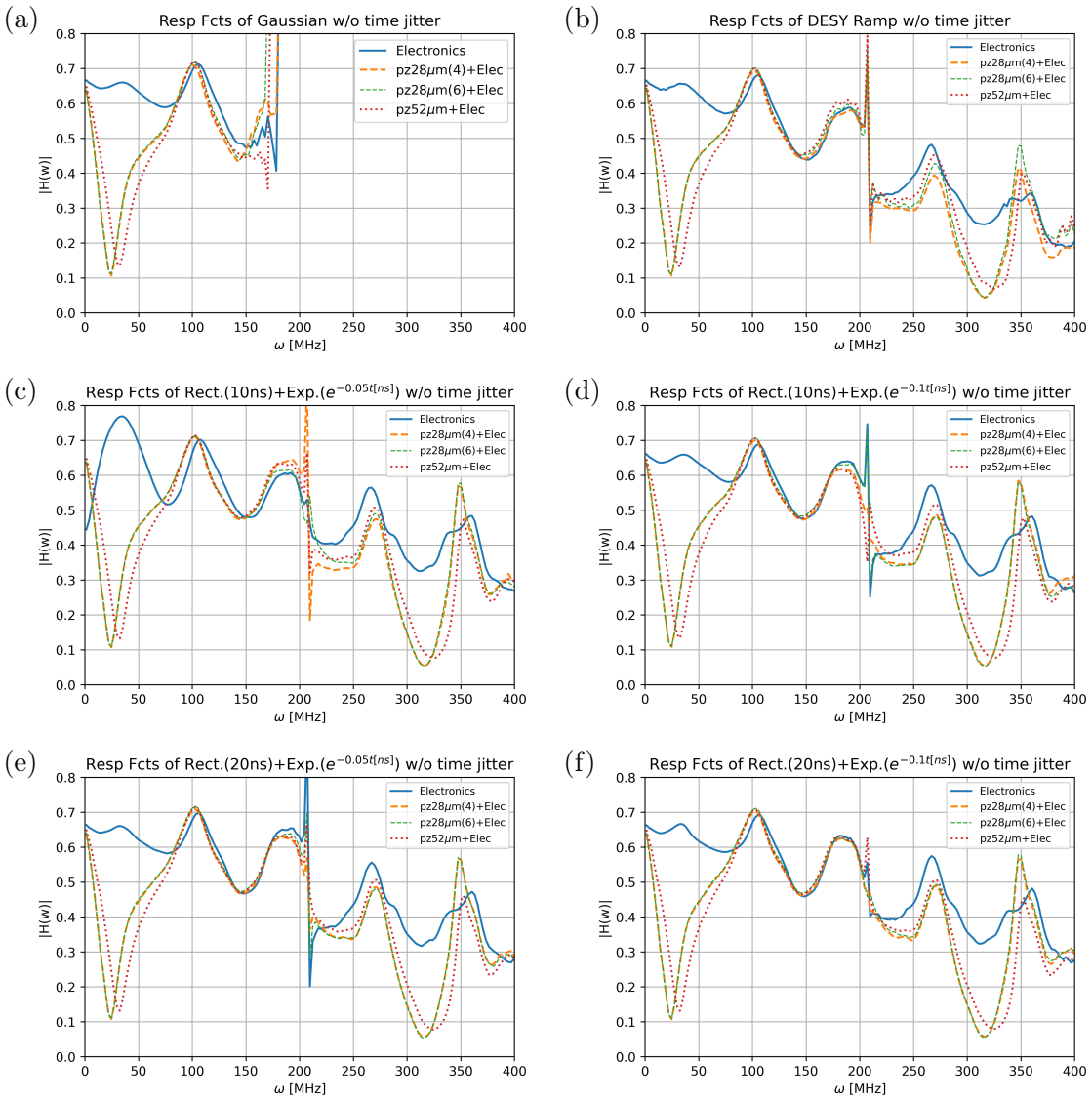

Figure 4.8: (a)-(f) The response functions of different voltage signals after eliminating the time jitter noise. The unusual features around 208MHz are due to zero-division error. The response function of pure electronics is in (c) contains an errored measurement at near 25MHz.

Despite of the general similarity, the response functions of DESY Ramp function starts deviating after 150MHz compared to the Rectangular and Exponential functions. The overall response function with DESY Ramp function shows diminished amplitudes than that of the Rectangular and Exponential functions. To understand this feature, we decompose the computed response function into two parts, electronics part and the pure piezo transducer part.

We can obtain the pure piezo transducer's reponse with $H_{pz}(\omega) = \frac{V_{\mathrm{pz+el}}(\omega)}{V_{\mathrm{el}}(\omega)}$. The $V_{\mathrm{el}}(\omega)$ are already measured and used for H_{el} (blue lines in Fig. 4.8). The Fig. 4.9 presents the obtained response function of the piezo transducer part. Each subplot contains only the piezo transducer's response function with various input voltage functions. The left subplot displays the responses of 28μm piezo transducer and it is 52μm piezo transducer's response for the right subplot. With H_{pz}, we can trace the reason of different response in DESY ramp input. From the agreeing H_{pz} functions for same thicknesses, we succeed to trace the source of deviation. This signfies that the **employed piezo transducer responds linearly to the given signal within the** 400**MHz and** 1.5**V.** But the electronics can show a different response depending on the input function.

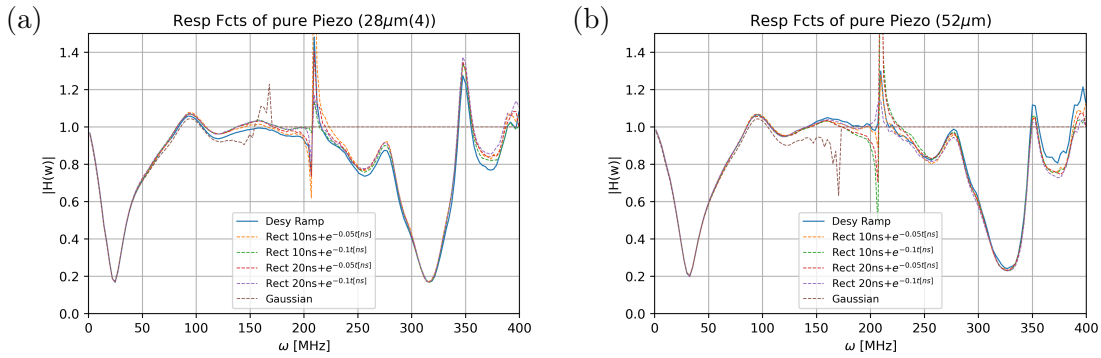

Figure 4.9: The response functions of pure piezo transducer responding to different types of input signals. This shows the responses of the piezo transducers are similar within the tested input voltages. The Gaussian's H_{pz} also fails after 150MHz due to quantization errors, therefore manually processed to have constant 1.

Chapter 5

Summary and Outlook

Summary

Two projects are carried over this Master's thesis. The Chapter 3 proposed a scheme shaping the waveform of the Mössbauer scattering field into short pulses with nanoseconds duration, with expectations of future application of nuclear coherent pump-probe measurement. And the second project aims to characterize the electronic response of the piezo transducer and relevant electronics to understand existing errors in motion of Mössbauer targets in Chapter 4. Complementing with future studies in mechanical response of system, it is expected to contribute to the control of the motion with better precision at future beamtime.

With a single Mössbauer target, the time intensity remains invariant though the motion can successfully modify its phases in the electric field. Instead, we used two Mössbauer targets to control the time intensity with the piezo transducers. When two targets are employed for the scattering, the intensity of the scattering field can be modified because the two scattering fields from two targets can interfere or beat depend on the applied motions.

Using the already-known scattering equation of two moving Mössbauer targets as a starting point, we first verified a few examples of the modified scattering field. The destructive interference of two fields is available with the step motions. When the step motion is applied, the two singly scattered fields are interfered and only the radiative coupling field are arriving at the detector. The second example is uniform motion where we saw the Doppler shifted field dresses a beating pattern at the time intensity. Furthermore, suppression of the radiative couplings was observed due to off-resonant condition. If the off-resonant condition is invariant over time, the intensity of the radiative coupling field can be approximated by the κ as a function of the detuning of two transitions and the targets' thicknesses.

The Section 3.2 introduces a way to control the waveform of the scattering field based on the destructive interference and beating effect. The proposed motions are composed of two linear motions for each target. When a low intensity is desired the motions create a destructive interference condition by driving two targets in the same profile of motion but keeping their relative distance as same to $(=\frac{\lambda}{2})$. So that two singly scattered fields are canceled each other. Purposely, if another set of motions is introduced to the targets, this interference condition is broken and a beating pattern emerges in the time intensity. If we control the duration of this motion, we can modify the decaying waveform into shape-pulse at a chosen time.

Soon after, the motions quickly recover the destructive interference conditions to introduce a second weak-intensity period before and after the produced pulse. The targets' thickness and velocity determine the time conditions of the pulse generation scheme, including the pulse's intensity, pulse duration, pulse-to-pulse delay. For the purpose of pulse generation, more variant motions can perform the same role to generate pulses. The conditions of the motions are discussed.

It is difficult to expect control of the intensity of radiative coupling field and singly scattered field by motions at the same time. Moreover, the maximum intensity of the pulse is also limited by the maximum intensity of the beating. To increase the contrast of the produced pulse, the property of polarization dependent scattering is exploited, alternatively, in Section 3.3. The proposed $\hat{k}, -\hat{k}$ configuration scatters the field in a way that its in-resonant radiative scattering field cancels each other due to the polarization mixing effect. Therefore, only a weak off resonant radiative scattering field can contribute to the intensities over the entire measurement time. The achieved lower intensity of radiative coupling field at the both sides of the produced pulse and pulse's intensity contrast gets enhanced.

The measurement reports that the displacement of Mössbauer targets don't follow the designed motion profile, exactly. To understand the reason for the imperfect motion, we investigate the electronic property of the motion system in the synchrotron experiment. By understanding the system we have used, we expect to have a better controlability at Mössbauer targets' motions and optimization of the motions for the coherent control of the Mössbauer scattering .

We measured the voltage traces that contains electronic response of the piezo transducer and electronics. The measurements are conducted with varying input voltage functions and different choices of the piezo transducers. The input voltage functions are chosen to characterize the response of the system over broad frequency components and the limitation of linear response. It is required to process the raw data to calculate the meaningful response function of the system. The average successfully reduces the thermal noise, and random noises. Because the DAQ stores more than 768ns, one sequence of the motion in synchrotron measurement, the data is tailored into 768ns long. The Fourier transformed averaged data then calculated into the response function with threshold. Then, the last time-jitter error is eliminated at the frequency space with using the time-jitter error function.

Restricting down to the response function of the piezo transducer, the study confirms that the piezo transducer responds fairly well and consistently to the input functions within 400MHz and 1.5V ranges. The linear response of the tested piezo transducer is what follows. The significant absorption takes place at the low frequency($<$100MHz). After thickness-dependent absorption features at low frequency($<$100MHz), the piezo transducer rarely responds to higher frequency ranges, though another unexpected but thickness-dependent absorption peak is found at 330MHz. And linear response of the piezo transducers are varying with their thicknesses. The thicker piezo transducer (52μm) has different absorption fre-

quencies (34MHz) than the piezo transducers (28μm) do (26MHz). On the other hand, we also observed the responses of electronics can show different response after 150MHz for different type of input functions.

Outlook

The pulse generation scheme requires a precise and fast speed of motion, which might be yet difficult to achieve in the laboratory. One possible project in the near future can direct to find an optimized motion. As discussed at the end of the pulse's property, other motions can replace the role of suggested recipe motions if they can control the destructive interference conditions. Specifically, the motions requiring instantaneous changes are difficult in a real experiment. Accepting the limitations in the achievable motions, more feasible motions can be studied. When the pulse is produced with continuously changing motions, it can bring additional points for the study. The instantaneous frequency of the pulse is determined by the instantaneous velocities of the two targets. For this reason, it has the application of generating a chirped pulse with the optimized motion.

The result of the second project can be re-stated as the verification of the piezo transducer's linear response within 400MHz and 1.5V amplitude. First, we can aim to build a more concrete understanding of obtained linear responses in the near future. The piezo transducer's linear response can be studied with various types of test input functions. Or the higher frequency range as well as the measurement with an amplifier can be carried out to see the limitation of linear responses. The result would accompany the understanding of the adopted electronics together. Of course, a few properties in response functions (overall 40MHz oscillation, second absorption feature of the piezo) are also required to be solved. Another important plan is to extend investigated response functions to include phases. The response function can carry different phase responses for the different frequency values, even if their magnitudes are the same. Without understanding the different phase response, the outcoming result would be far away from the expectations. After achieving a concrete understanding of the electronic response of the piezo, the next step would straightforwardly be to study the response of real displacement with the photon sources.

Appendix A

Additional material

A.1 Maxwell equation in medium and first order wave equation

The electromagnetic field inside material is expressed as the sum of external field and the induced internal field.

For the purpose the following auxiliary fields are defined [69].

$$\begin{cases} \overrightarrow{D} = \epsilon_0 \overrightarrow{E} + \overrightarrow{P} \\ \overrightarrow{H} = \frac{1}{\mu_0} \overrightarrow{B} - \overrightarrow{M} \\ \overrightarrow{J}_f = \sigma \overrightarrow{E} \end{cases} \tag{A.1}$$

The $\overrightarrow{P}$ is the Polarization, a measurable in the experiement. It is the averaged dipole moments over sizable area of medium. And the Displacement $\overrightarrow{D}$ is represented a sum of external field $\overrightarrow{E}$ and induced field $\overrightarrow{P}$. Similarly the auxiliary field $\overrightarrow{H}$ is adopted to represent the total magnetic field inside the material with sum of external magnetic field $\overrightarrow{B}$ and induced magnetic field, Magnetization $\overrightarrow{M}$. The last equation explains an induced current, proportional to external field and conductivity σ.

It is neccessary to consider the total fields in one position to describe the behavior of the electromagnetic fields [69].

$$\begin{cases} \overrightarrow{\nabla} \cdot \overrightarrow{D} = \rho_f \\ \overrightarrow{\nabla} \cdot \overrightarrow{B} = 0 \\ \overrightarrow{\nabla} \times \overrightarrow{E} = -\partial_t \overrightarrow{B} \\ \overrightarrow{\nabla} \times \overrightarrow{H} = \overrightarrow{J} + \partial_t \overrightarrow{D} \end{cases} \tag{A.2}$$

One of solution of the set of equations is the electromagnetic wave equation.

Taking curl operation for third Maxwell's equation,

$$\begin{aligned} \overrightarrow{\nabla} \times (\overrightarrow{\nabla} \times \overrightarrow{E}) = -\nabla \times (\partial_t \overrightarrow{B}) &= -\partial_t (\nabla \times \overrightarrow{B}) \\ &= -\mu_0 \partial_t (\nabla \times \overrightarrow{H}) \end{aligned} \tag{A.3}$$

Assuming there is no free current $\overrightarrow{J}_f = 0$, the wave equation in medium without free charge and free current is obtained.

$$\overrightarrow{\nabla} \times (\overrightarrow{\nabla} \times \overrightarrow{E}) = -\mu_0 \partial_{tt} \overrightarrow{D} \tag{A.4}$$

The second order wave equation in medium can be reduced into first order.

Using vector identity,

$$-\nabla^2 \overrightarrow{E} + \nabla(\nabla \cdot \overrightarrow{E}) = -\mu_0 \partial_{tt} \overrightarrow{D} \tag{A.5}$$

$$= -\mu_0 \partial_{tt} (\epsilon_0 \overrightarrow{E} + \overrightarrow{P}) \tag{A.6}$$

Since we are supposing the medium without free charge, $\rho_f = 0$, and isotropic medium, $\nabla \cdot \overrightarrow{P} = 0$,

$$\nabla^2 \overrightarrow{E} - \frac{1}{c^2} \partial_{tt} \overrightarrow{E} = (\nabla - \frac{1}{c} \partial_t)(\nabla + \frac{1}{c} \partial_t) \overrightarrow{E} = \mu_0 \partial_{tt} \overrightarrow{P}. \tag{A.7}$$

The operations can be replaced as $\nabla = ik$, and $\partial_t = -i\omega$.

$$(ik + i\frac{\omega}{c})(\nabla + \frac{1}{c} \partial_t) \overrightarrow{E} = -\mu_0 \omega^2 \overrightarrow{P}$$

$$\rightarrow (\nabla + \frac{1}{c} \partial_t) \overrightarrow{E} = i \frac{k}{2\epsilon_0} \overrightarrow{P}, \tag{A.8}$$

A.2 Scattering equation of two moving targets

When moving targets are in consideration, it is necessary to describe each scattering event in respective target's rest frame.

$E_0(z,t)$: Scattering field from the A target observed in the lab frame.

$$E_0(z,t) = \delta(t) e^{ikz} e^{-i\omega t} + T_A(t) e^{ikz} e^{ik\Delta z_A(t)} e^{-ik\Delta z_A(0)},$$

where the $T_A(t)$ indicates the amplitude of the A target. The effect of motion is included by the $\Delta z_A(t)$, the motion of the A target.

$E^i_{\mathrm{B}}(z',t)$: Incident field of the B target ($E_0(z,t)$) observed in the B target rest frame.

The total incident fields for the B target include the non-interacting part and the scattered field of the A target. In the B target rest frame, the two incident fields

are observed as,

$$\begin{aligned} E_B^i(z',t) &= E_0(\mathbf{T}_B\{z\},t) = E_0(z-\Delta z_B(t),t) \\ &= \delta(t)e^{ik(z-\Delta z_B(t))}e^{-i\omega t} + T_A(t)e^{ik(z-\Delta z_B(t))}e^{ik\Delta z_A(t)}e^{-ik\Delta z_A(0)} \\ &= \delta(t)e^{ik(z-\Delta z_B(t))}e^{-i\omega t} + T_A(t)e^{ikz}e^{-ik\Delta z_{BA}(t)}e^{-ik\Delta z_A(0)} \end{aligned}$$

The subscript 'B' of the electric field stand for the B target rest frame. The z' is the coordinate of the B target rest frame. The bold $\mathbf{T}_B$ represents the transformation from the lab frame to the rest frame of the B target. Similar to $\Delta z_A(t)$, $\Delta z_B(t)$ represents the motion of the B target. The $\Delta z_{BA}(t)$ is introduced after defining $\Delta z_{BA}(t) = \Delta z_B(t) - \Delta z_A(t)$.

E_B^{scatt}: Scattering at the B target in its rest frame.

$$\begin{aligned} E_B^{\text{scatt}}(z',t) =& R_B(t) \otimes E_B^i(z',t) \\ =& e^{ikz}\int \{\delta(t-\tau)e^{-i\omega(t-\tau)} + T_B(t-\tau)\} \\ & \times \{\delta(\tau)e^{-i\omega\tau}e^{-ik\Delta z_B(\tau)} + T_A(\tau)e^{-ik\Delta z_{BA}(\tau)}e^{-ik\Delta z_A(0)}\}d\tau \\ =& \delta(t)e^{ikz}e^{-i\omega t}e^{-ik\Delta z_B(0)} + T_B(t)e^{ikz}e^{-ik\Delta z_B(0)} \\ & + T_A(t)e^{ikz}e^{-ik\Delta z_{BA}(t)}e^{-ik\Delta z_A(0)} + \{T_B(t)\otimes T_A(t)e^{-ik\Delta z_{BA}(t)}\}e^{ikz}e^{-ik\Delta z_A(0)} \end{aligned}$$

The $R_B(t)$ is the response function of the resting target. It is possible to use $R_B(t)$ to describe the scattering of the moving target since the scattering is currently described in the B target's rest frame.

$E_{\text{lab}}^{\text{scatt}}(z,t)$: Scattering field in the lab frame.
The field is required to transform back to the lab frame object.

$$\begin{aligned} E_{\text{lab}}^{\text{scatt}}(z,t) &= E_B^{\text{scatt}}(\mathbf{T}_B^{-1}\{z'\},t) \\ &= E_B^{\text{scatt}}(z+\Delta z_B,t), \end{aligned}$$

where $\mathbf{T}_B^{-1}$ indicates the transformation matrix from the B target rest frame to the lab frame.

$$\begin{aligned} E_{\text{lab}}^{\text{scatt}}(z,t) =& \delta(t)e^{ikz}e^{-i\omega t} \\ & + T_B(t)e^{ik(z+\Delta z_B(t))}e^{-ik\Delta z_B(0)} \\ & + T_A(t)e^{ik(z+\Delta z_A(t))}e^{-ik\Delta z_A(0)} \\ & + (T_B(t)\otimes T_A(t)e^{-ik(\Delta z_{BA}(t)-z_{BA}(0))})e^{ik(z+\Delta z_B(t))}e^{-ik\Delta z_B(0)}, \end{aligned} \tag{A.9}$$

where the $z_{BA}(0)$ is put explicitly. The above equation describes the scattering fields of two moving targets with arbitral motions.

A.3 Radiative coupling scattering field calculation with PYNUSS

PYNUSS is a Python package, which is based on the software package conuss [94], used to compute for the NFS spectra of moving target over this thesis [81]. The PYNUSS calculates the spectra based on the frequency space with already-known variables for various kind of Mössbauer targets.

One simple approach to describe the scattering is to use response matrix as in Eq. (2.40). The response matrix contains the transition information as well as information about the polarization dependent scatterings. The response matrix of the employed targets are straightforward for the static cases. The scattering of two targets are described as,

$$E(\omega) = R_B(\omega)R_A(\omega)E_0(\omega)$$

On the other hand, the response matrix of the targets becomes different when the targets are moving. The PYNUSS calculates the new $R_A(\omega)$ and $R_B(\omega)$ with given motions to reflect the effect of the motions based on Eq. (2.54).

$$R'(\omega) = \int_{-\infty}^{\infty} \{\delta(t)e^{-i\omega t}e^{ikz} - b\frac{J_1(\sqrt{2bt})}{\sqrt{bt}}e^{-\gamma t}e^{-i\omega_0 t}e^{ikz}e^{ik\Delta z(t)}\theta(t)e^{-ik\Delta z(0)}\}e^{-i\omega t}dt$$

Therefore, the response function of moving targets are not equal to the static cases and the scattering equation should reflect the modified response functions.

$$E_{\text{moving}}(\omega) = R'_B(\omega)R'_A(\omega)E_0(\omega)$$

General idea

Following computation of PYNUSS for the two targets scattering, it always results the total time intensity which includes the synchrotron pulse, the singly scattered fields, as well as the radiative coupling scattering field.

The same approach is exploited to separate the each field from the $R'(\omega)$. We can suppose that one response function is composed of two part, non-interacting part matrix $I'(\omega)$ and the scattered part matrix $T'(\omega)$. The $I'(\omega)$ is not equal to identical matrix, rather its components are complex values because the field experiences a phase modification for all frequency values.

$$R'(\omega) = I'(\omega) + T'(\omega)$$

Second assumption needs to be made to find the $I'(\omega)$ from the $R'(\omega)$. We suppose that $R'(\omega)$ at $\omega \gg \omega_0$ contains only $I'(\omega)$ and further assume that $I'(\omega)$ is defined as same for all ω.

Decomposition

The scattering field can be expressed by each terms as,

$$\begin{aligned} E_{\text{moving}}(\omega) &= R'_B(\omega)R'_A(\omega) \times E_0(\omega) \\ &= (I'_B(\omega) + T'_B(\omega))(I'_A(\omega) + T'_A(\omega)) \times E_0(\omega) \\ &= (I'_B(\omega)I'_A(\omega) + I'_B(\omega)T'_A(\omega) + T'_B(\omega)I'_A(\omega) + T'_B(\omega)T'_A(\omega)) \times E_0(\omega) \end{aligned}$$

Our interest is to see sole value of the term $T'_B(\omega)T'_A(\omega)$.

To see the effect of $T'_B(\omega)T'_A(\omega)$, the same method will separate $R'_A(t)$ into $I'_A(\omega)$, and $T'_A(\omega)$ by running independent PYNUSS code with only A target is involved. The $I'_B(\omega)$, and $T'_B(\omega)$ can be obtained in an opposite way.

Then,

$$(R'_B(t) - I'_B(t))(R'_A(t) - I'_A(t)) \times E_0(\omega) = (T'_B(\omega)T'_A(\omega)) \times E_0(\omega)$$

Lastly, the manually computed field is transformed into time,

$$E_{\text{radi}}(t) = \frac{1}{2\pi}\int_{\infty}^{\infty} (T'_B(\omega)T'_A(\omega)) \times E_0(\omega)e^{i\omega t}d\omega.$$

A.4 Radiative coupling field of step motion

What we aim to prove is the upper boundary of amplitude of radiative coupling scattering field of the step motioning targets. The raidaitve coupling field of static targets is

$$\int_0^t b^2 \frac{J_1(\sqrt{2b(t-\tau)})}{\sqrt{b(t-\tau)}} \frac{J_1(\sqrt{2b\tau})}{\sqrt{b\tau}} d\tau \times e^{-\gamma t}e^{ikz}e^{-i\omega_0 t} = \int_0^t Y(t,\tau)e^{-\gamma t}e^{ikz}e^{-i\omega_0 t},$$

where $Y(t,\tau) = b^2 \frac{J_1(\sqrt{2b(t-\tau)})}{\sqrt{b(t-\tau}} \frac{J_1(\sqrt{2b\tau})}{\sqrt{b\tau}}$.

Since the resultant phase satisfies $|e^{-ik\Delta z_0\theta(t-t_0)}| \leq 1$, the following inequation also holds for each integrand:

$$|Y(t,\tau)e^{-ik\Delta z_0\theta(\tau-t_0)}| \leq |Y(t,\tau)|,$$

There is another inequation that always holds.

$$|\int_0^t (Y(t,\tau)e^{-ik\Delta z_0\theta(\tau-t_0)})d\tau| \leq \int_0^t |Y(t,\tau)e^{-ik\Delta z_0\theta(\tau-t_0)}|d\tau$$

Therefore,

$$|\underbrace{\int_0^t (Y(t,\tau)e^{-ik\Delta z_0\theta(\tau-t_0)})d\tau}_{T_B\otimes T_A e^{-ik\Delta z_0\theta(t-t_0)}}| \leq \int_0^t |Y(t,\tau)|d\tau = \underbrace{\int_0^t Y(t,\tau)d\tau}_{T_B\otimes T_A}$$

The last equation additionally holds when $|Y(t,\tau)| = Y(t,\tau)$ during entire integration times, equivalently when the t solving $Y(t,\tau) = 0$ doesn't locate within integration range. The proposed numerical result (Fig. 3.2) can answer the location of such t as a function of thickness. The figures confirm that such t locates beyond 150ns for thickness within 1μm.

Therefore it concludes the $|T_B \otimes T_A e^{-ik\Delta z_0\theta(t-t_0)}|^2 < |T_B \otimes T_A|^2$. The same conclusion can be found if $|Y(t,\tau)| = -Y(t,\tau)$, as well.

A.5 Radiative coupling field with off-resonant condition with HF iron

The idea can be directly extended to the iron with hyperfine structures. In our case, the scattering field is

$$\begin{aligned} E(\omega) &= R'(\omega)R(\omega)E_0(\omega) \\ &= 1 + (e^{\frac{-3ib/4}{\hbar(\omega-\omega_1)+i\gamma}} + e^{\frac{-ib/4}{\hbar(\omega-\omega_3)+i\gamma}} - 1) \\ &\quad + (e^{\frac{-ib/4}{\hbar(\omega-\omega_4)+i\gamma}} + e^{\frac{-3ib/4}{\hbar(\omega-\omega_6)+i\gamma}} - 1) \\ &\quad + (e^{\frac{-3ib/4}{\hbar(\omega-\omega_1)+i\gamma}} + e^{\frac{-ib/4}{\hbar(\omega-\omega_3)+i\gamma}} - 1)(e^{\frac{-ib/4}{\hbar(\omega-\omega_4)+i\gamma}} + e^{\frac{-3ib/4}{\hbar(\omega-\omega_6)+i\gamma}} - 1) \end{aligned} \tag{A.10}$$

Similarly, we can introduce κ_1 to κ_4 to reflect the off-resonant radiative coupling fields.

$$\begin{aligned} E(\omega) = 1 &+ (e^{\frac{-3ib/4}{\hbar(\omega-\omega_1)+i\gamma}} - 1)(1+\kappa_1) + (e^{\frac{-ib/4}{\hbar(\omega-\omega_3)+i\gamma}} - 1)(1+\kappa_3) \\ &+ (e^{\frac{-ib/4}{\hbar(\omega-\omega_4)+i\gamma}} - 1)(1+\kappa_4) + (e^{\frac{-3ib/4}{\hbar(\omega-\omega_6)+i\gamma}} - 1)(1+\kappa_6), \end{aligned} \tag{A.11}$$

Because the approximation has to hold for all ω, one can find the κ_1 to κ_6 with asymptotical approach.

Solving four sets of coupled equation with off-resonant conditions,

$$\kappa_1 = -\kappa_6 = -i\frac{1}{4}(\frac{1}{2}\frac{b}{\Delta_{13}} + \frac{1}{2}\frac{3b}{\Delta_{16}}) \tag{A.12}$$

$$\kappa_3 = -\kappa_4 = -i\frac{1}{4}(\frac{1}{2}\frac{3b}{\Delta_{31}} + \frac{1}{2}\frac{b}{\Delta_{34}}), \tag{A.13}$$

with Δ_{ij} is defined as $\Delta_{ij} = \hbar(\omega_i - \omega_j)$. The detunings and the thickness parameters are defined in the Table 2.1 and Eq. (2.28).

The scattering field is read as

$$\begin{aligned} E_{\text{far-off}}(t>0) =& \kappa_1 \times \frac{3b}{4}\frac{J_1(\sqrt{3bt/2})}{\sqrt{3bt/4}}e^{-\gamma t}(e^{-i\omega_1 t} - e^{-i\omega_6 t}) \\ &+ \kappa_3 \times \frac{b}{4}\frac{J_1(\sqrt{bt/2})}{\sqrt{bt/4}}e^{-\gamma t}(e^{-i\omega_3 t} - e^{-i\omega_4 t})) \end{aligned} \tag{A.14}$$

Bibliography

[1] T. H. Maiman et al. “Stimulated optical radiation in ruby”. In: (1960).

[2] D. Killinger. “Free space optics for laser communication through the air”. In: *Optics and photonics news* 13.10 (2002), pages 36–42.

[3] B. Muralikrishnan, S. Phillips, and D. Sawyer. “Laser trackers for large-scale dimensional metrology: A review”. In: *Precision Engineering* 44 (2016), pages 13–28.

[4] S. Svanberg. “Laser Spectroscopy”. In: *Atomic and Molecular Spectroscopy: Basic Aspects and Practical Applications*. Springer, 2023, pages 339–454.

[5] S. Stenholm. *Foundations of laser spectroscopy*. Courier Corporation, 2012.

[6] T. Ditmire et al. “Nuclear fusion from explosions of femtosecond laser-heated deuterium clusters”. In: *Nature* 398.6727 (1999), pages 489–492.

[7] C. Hönninger et al. “Q-switching stability limits of continuous-wave passive mode locking”. In: *JOSA B* 16.1 (1999), pages 46–56.

[8] H. A. Haus. “Mode-locking of lasers”. In: *IEEE Journal of Selected Topics in Quantum Electronics* 6.6 (2000), pages 1173–1185.

[9] D. Kuizenga and A. Siegman. “FM and AM mode locking of the homogeneous laser-Part I: Theory”. In: *IEEE Journal of Quantum Electronics* 6.11 (1970), pages 694–708.

[10] P. Maine et al. “Generation of ultrahigh peak power pulses by chirped pulse amplification”. In: *IEEE Journal of Quantum electronics* 24.2 (1988), pages 398–403.

[11] M. Pessot, P. Maine, and G. Mourou. “1000 times expansion/compression of optical pulses for chirped pulse amplification”. In: *Optics communications* 62.6 (1987), pages 419–421.

[12] E. Knoesel, A. Hotzel, and M. Wolf. “Ultrafast dynamics of hot electrons and holes in copper: Excitation, energy relaxation, and transport effects”. In: *Physical Review B* 57.20 (1998), page 12812.

[13] A. Woutersen, U. Emmerichs, and H. Bakker. “Femtosecond mid-IR pump-probe spectroscopy of liquid water: Evidence for a two-component structure”. In: *Science* 278.5338 (1997), pages 658–660.

[14] V. Giovannetti, S. Lloyd, and L. Maccone. “Advances in quantum metrology”. In: *Nature photonics* 5.4 (2011), pages 222–229.

[15] E. Polino et al. “Photonic quantum metrology”. In: *AVS Quantum Science* 2.2 (2020), page 024703.

[16] A. M. Childs, J. Preskill, and J. Renes. “Quantum information and precision measurement”. In: *Journal of modern optics* 47.2-3 (2000), pages 155–176.

[17] J. P. Marangos. “Electromagnetically induced transparency”. In: *Journal of Modern Optics* 45.3 (1998), pages 471–503.

[18] M. Engel et al. “Light–matter interaction in a microcavity-controlled graphene transistor”. In: *Nature communications* 3.1 (2012), page 906.

[19] C. Brif, R. Chakrabarti, and H. Rabitz. “Control of quantum phenomena: past, present and future”. In: *New Journal of Physics* 12.7 (2010), page 075008.

[20] S. Witte et al. “Deep-ultraviolet quantum interference metrology with ultrashort laser pulses”. In: *Science* 307.5708 (2005), pages 400–403.

[21] J. Lim et al. “Ultrafast Ramsey interferometry to implement cold atomic qubit gates”. In: *Scientific reports* 4.1 (2014), page 5867.

[22] D. A. Shapiro et al. “Chemical composition mapping with nanometre resolution by soft X-ray microscopy”. In: *Nature Photonics* 8.10 (2014), pages 765–769.

[23] D. Sayre and H. Chapman. “X-ray microscopy”. In: *Acta Crystallographica Section A: Foundations of Crystallography* 51.3 (1995), pages 237–252.

[24] P. Glatzel and U. Bergmann. “High resolution 1s core hole X-ray spectroscopy in 3d transition metal complexes—electronic and structural information”. In: *Coordination chemistry reviews* 249.1-2 (2005), pages 65–95.

[25] P. Norman and A. Dreuw. “Simulating X-ray spectroscopies and calculating core-excited states of molecules”. In: *Chemical reviews* 118.15 (2018), pages 7208–7248.

[26] T. J. Bürvenich, J. Evers, and C. H. Keitel. “Nuclear quantum optics with x-ray laser pulses”. In: *Physical review letters* 96.14 (2006), page 142501.

[27] T. Kanaya et al. “Relaxation transition in glass-forming polybutadiene as revealed by nuclear resonance X-ray scattering”. In: *The Journal of Chemical Physics* 140.14 (2014), page 144906.

[28] B. W. Adams et al. “X-ray quantum optics”. In: *Journal of modern optics* 60.1 (2013), pages 2–21.

[29] D. H. Bilderback, P. Elleaume, and E. Weckert. “Review of third and next generation synchrotron light sources”. In: *Journal of Physics B: Atomic, molecular and optical physics* 38.9 (2005), S773.

[30] DESY. *Machine Parameters PETRA III (Design Values)*. `http://photon-science.desy.de/facilities/petra_iii/machine/parameters/index_eng.html`. Acessed: 08.09.2021.

[31] R. Rüffer and A. I. Chumakov. "Nuclear resonance beamline at ESRF". In: *Hyperfine Interactions* 97.1 (1996), pages 589–604.

[32] A. Singer et al. "Hanbury Brown–Twiss interferometry at a free-electron laser". In: *Physical review letters* 111.3 (2013), page 034802.

[33] D. Pelliccia et al. "Experimental x-ray ghost imaging". In: *Physical review letters* 117.11 (2016), page 113902.

[34] A.-X. Zhang et al. "Tabletop x-ray ghost imaging with ultra-low radiation". In: *Optica* 5.4 (2018), pages 374–377.

[35] S. Shwartz et al. "X-ray parametric down-conversion in the Langevin regime". In: *Physical Review Letters* 109.1 (2012), page 013602.

[36] R. Santra, N. V. Kryzhevoi, and L. S. Cederbaum. "X-ray two-photon photoelectron spectroscopy: a theoretical study of inner-shell spectra of the organic para-aminophenol molecule". In: *Physical review letters* 103.1 (2009), page 013002.

[37] B. W. McNeil and N. R. Thompson. "X-ray free-electron lasers". In: *Nature photonics* 4.12 (2010), pages 814–821.

[38] M. Altarelli, R. Brinkmann, and M. Chergui. "The European X-ray free-electron laser. Technical design report". In: (2007).

[39] A. I. Chumakov et al. "Superradiance of an ensemble of nuclei excited by a free electron laser". In: *Nature Physics* 14.3 (2018), pages 261–264.

[40] A. Picon and S. Southworth. "STIRAP with XFEL pulses". In: *APS Division of Atomic, Molecular and Optical Physics Meeting Abstracts*. Volume 2015. 2015, J4–002.

[41] G. K. Wertheim. *Mössbauer effect: principles and applications*. Academic Press, 2013.

[42] U. Van Bürck et al. "Nuclear forward scattering of synchrotron radiation". In: *Physical Review B* 46.10 (1992), page 6207.

[43] Y. V. Shvyd'Ko et al. "Storage of nuclear excitation energy through magnetic switching". In: *Physical review letters* 77.15 (1996), page 3232.

[44] W.-T. Liao, A. Pálffy, and C. H. Keitel. "Coherent storage and phase modulation of single hard-x-ray photons using nuclear excitons". In: *Physical Review Letters* 109.19 (2012), page 197403.

[45] R. Röhlsberger et al. "Collective Lamb shift in single-photon superradiance". In: *Science* 328.5983 (2010), pages 1248–1251.

[46] J. MacGillivray and M. Feld. "Criteria for x-ray superradiance". In: *Applied Physics Letters* 31.2 (1977), pages 74–76.

[47] Y. V. Shvyd'Ko et al. "Fast switching of nuclear BRAGG scattering of synchrotron radiation by a pulsed magnetic field". In: *Europhysics Letters* 26.3 (1994), page 215.

[48] Y. V. Shvyd'ko, S. Popov, and G. Smirnov. "Coherent re-emission of gamma-quanta in the forward direction after a stepwise change of the energy of nuclear excitation". In: *Journal of Physics: Condensed Matter* 5.10 (1993), page 1557.

[49] K. P. Heeg et al. "Coherent X-ray- optical control of nuclear excitons". In: *Nature* 590.7846 (2021), pages 401–404.

[50] L. Bocklage et al. "Coherent control of collective nuclear quantum states via transient magnons". In: *Science advances* 7.5 (2021), eabc3991.

[51] G. Smirnov and W. Potzel. "Perturbation of nuclear excitons by ultrasound". In: *Hyperfine Interactions* 123.1-4 (1999), pages 633–663.

[52] F. Vagizov et al. "Coherent control of the waveforms of recoilless γ-ray photons". In: *Nature* 508.7494 (2014), pages 80–83.

[53] K. P. Heeg et al. "Spectral narrowing of x-ray pulses for precision spectroscopy with nuclear resonances". In: *Science* 357.6349 (2017), pages 375–378.

[54] J. Evers. private communication.

[55] M. Gerharz. private communication.

[56] R. L. Mössbauer. "Kernresonanzfluoreszenz von gammastrahlung in Ir 191". In: *Zeitschrift für Physik* 151 (1958), pages 124–143.

[57] R. Röhlsberger. *Nuclear condensed matter physics with synchrotron radiation: Basic principles, methodology and applications*. Volume 208. Springer Science & Business Media, 2004.

[58] W. Potzel et al. "Gravitational redshift experiments with the high-resolution Mössbauer resonance in 67 Zn". In: *Hyperfine Interactions* 72 (1992), pages 195–214.

[59] C. Schröder et al. "Field-portable Mössbauer spectroscopy on Earth, the Moon, Mars, and beyond". In: *Geochemistry: Exploration, Environment, Analysis* 11.2 (2011), pages 129–143.

[60] A. J. Bearden et al. "Mössbauer spectroscopy of heme and hemin compounds." In: *Proceedings of the National Academy of Sciences* 53.6 (1965), pages 1246–1253. DOI: 10.1073/pnas.53.6.1246.

[61] U. Van Burck et al. "Suppression of nuclear inelastic channels in nuclear resonance and electronic scattering of γ-quanta for different hyperfine transitions in perfect 57Fe single crystals". In: *Journal of Physics C: Solid State Physics* 11.11 (1978), page 2305.

[62] G. Smirnov. "General properties of nuclear resonant scattering". In: *Hyperfine Interactions* 123.1-4 (1999), pages 31–77.

[63] J. Hannon and G. Trammell. "Coherent γ-ray optics". In: *Hyperfine Interactions* 123 (1999), pages 127–274.

[64] M. O. Scully and M. S. Zubairy. *Quantum optics*. 1999.

[65] D. P. Siddons, U. Bergmann, and J. B. Hastings. "Polarization effects in resonant nuclear scattering". In: *Hyperfine Interactions* 123.1-4 (1999), pages 681–719.

[66] B. Fultz. "Mössbauer Spectrometry". In: *Characterization of Materials*. John Wiley & Sons, Ltd, 2002. ISBN: 9780471266969. DOI: https://doi.org/10.1002/0471266965.com069.

[67] K. P. Heeg. "X-Ray quantum optics with Mössbauer nuclei in thin-film cavities". PhD thesis. 2014.

[68] J. Mendez-Garza et al. "Synthesis and surface modification of spindle-type magnetic nanoparticles: gold coating and PEG functionalization". In: *Journal of Biomaterials and Nanobiotechnology* 4 (2013), pages 222–228.

[69] D. J. Griffiths. "INTRODUCTION TO ELECTRODYNAMICS Fourth Edition". In: (2021).

[70] Y. V. Shvyd'ko. "Nuclear resonant forward scattering of x rays: Time and space picture". In: *Physical Review B* 59.14 (1999), page 9132.

[71] P. Reiser. "Time domain control of x-ray quantum dynamics". PhD thesis. Ruprecht-Karls-Universität Heidelberg, 2014.

[72] W.-T. Liao and W.-T. Liao. "Nuclear coherent population transfer with x-ray laser pulses". In: *Coherent Control of Nuclei and X-Rays* (2014), pages 27–48.

[73] I. V. Hertel and C.-P. Schulz. *Atoms, molecules and optical physics*. Springer, 2014.

[74] Y. V. Shvyd'ko et al. "Hybrid beat in nuclear forward scattering of synchrotron radiation". In: *Physical Review B* 57.6 (1998), page 3552.

[75] M. Crisp. "Propagation of small-area pulses of coherent light through a resonant medium". In: *Physical Review A* 1.6 (1970), page 1604.

[76] M. Lax. "Multiple scattering of waves". In: *Reviews of Modern Physics* 23.4 (1951), page 287.

[77] R. L. Cohen. *Applications of Mössbauer spectroscopy*. Academic Press, 2013.

[78] J. Hastings et al. "Mössbauer spectroscopy using synchrotron radiation". In: *Physical review letters* 66.6 (1991), page 770.

[79] U. Fano. "Effects of Configuration Interaction on Intensities and Phase Shifts". In: *Phys. Rev.* 124 (6 Dec. 1961), pages 1866–1878. DOI: 10.1103/PhysRev.124.1866.

[80] G. Smirnov et al. "Nuclear γ resonance time-domain interferometry: Quantum beat and radiative coupling regimes compared in revealing quasielastic scattering". In: *Physical Review B* 73.18 (2006), page 184126.

[81] K. P. Heeg. private communication.

[82] M. Gerharz. "Temporal phase and polarization interferometry at x-ray energies: Reconstruction of phase-related observables and temporal pulse shaping". PhD thesis. Ruprecht-Karls-Universität Heidelberg, 2021.

[83] S. Y. Mironov, M. V. Starodubtsev, and E. A. Khazanov. "Temporal contrast enhancement and compression of output pulses of ultra-high power lasers". In: *Opt. Lett.* 46.7 (Apr. 2021), pages 1620–1623. DOI: 10.1364/OL.415430.

[84] A. Arnau et al. *Piezoelectric transducers and applications*. Volume 2004. Springer, 2004.

[85] P. Ueberschlag. "PVDF piezoelectric polymer". In: *Sensor review* 21.2 (2001), pages 118–126.

[86] *Keysight 81150A and 81160A Pulse Function Arbitrary Noise Generators*. Keysight Technologies. URL: https://www.keysight.com/de/de/assets/7018-01537/data-sheets/5989-6433.pdf.

[87] *Digital Delay Generator DG645*. Stanford Research Systems. URL: https://www.thinksrs.com/downloads/pdfs/catalog/DG645c.pdf.

[88] DESY. *Avalanche Photo Diodes PETRA III*. https://photon-science.desy.de/facilities/petra_iii/beamlines/p01_dynamics/nuclear_resonant_scattering_station/detectors/apds/index_eng.htmll.

[89] S. P. Division. *Piezo Film Sensors Technical Manual P/N 1005663-1 REV B*. Measurement Specialities Inc. URL: http://www.ehag.ch/PDF-Files/MSI/techman.pdf.

[90] *RoentDek TDC8HP System Manual*. RoentDek Handels GmbH. URL: http://www.roentdek.com/manuals/TDC8HP%20Manual.pdf.

[91] J. Van de Vegte. *Feedback control systems*. Prentice-Hall, Inc., 1994.

[92] C. L. Phillips and R. D. Harbor. *Feedback control systems*. Prentice-Hall, Inc., 1999.

[93] A. Stejskal. private communication.

[94] W. Sturhahn. "CONUSS and PHOENIX: Evaluation of nuclear resonant scattering data". In: *Hyperfine Interactions* 125.1 (2000), pages 149–172. DOI: 10.1023/A:1012681503686.

Acknowledgement

I would like to spare the last page to thank the all people who have influenced me during my studies. I feel like I was lucky that I have been being in the right place near the best people from whom I can seek advice and whom willing to help me with my studies and my life. I couldn't thank more to Jörg Evers regarding the overall advice and ideas reflected in my thesis. I shouldn't forget to say thanks to all of Miriam Gerharz, Lukas Wolff Ze-An Peng, and Ales Stejskal for the interesting discussions as well as their sincere advice during my study. Cooperation with you gave me a lot of learning points to me. Learnings are not always easy, but I am sure that the study will be priceless assets for me. I want to close by mentioning my roommate, Shinhyung Hwang for his somewhere between Korean 'Jeong' and American's 'Friendliness'. And it is somehow illegal not to mention my family. My family is also a good supporter of my Master's study abroad and the solid ground where all my experiences has been able to foot on.

Erklärung:

Ich versichere, dass ich diese Arbeit selbstständig verfasst habe und keine anderen als die angegebenen Quellen und Hilfsmittel benutzt habe.

Heidelberg, den 30.04.2023 ..... 이준희